Final Technical Report: Multi-Timescale Integrated Dynamics and Scheduling for Solar (MIDAS-Solar)

Jin Tan,[1] Andy Hoke,[1] Haoyu Yuan,[1] Bin Wang,[1] Rick Wallace Kenyon,[1] Xin Fang,[1] Przemyslaw Koralewicz,[1] Emanuel Mendiola,[1] Yingchen Zhang,[1] Yilu Liu,[2] Shutang You,[2] Mirka Mandich,[2] Annie Zhao,[2] Jianhui Wang,[3] Shengfei Yin,[3] Yanling Lin,[3] Erik Ela,[4] Vikas Singhvi,[4] Parag Mitra,[4] and Robert Entrike[4]

1 National Renewable Energy Laboratory
2 University of Tennessee, Knoxville
3 Southern Methodist University
4 Electric Power Research Institute

NREL is a national laboratory of the U.S. Department of Energy
Office of Energy Efficiency & Renewable Energy
Operated by the Alliance for Sustainable Energy, LLC

This report is available at no cost from the National Renewable Energy Laboratory (NREL) at www.nrel.gov/publications.

Contract No. DE-AC36-08GO28308

Technical Report
NREL/TP-5D00-85679
April 2023

Final Technical Report: Multi-Timescale Integrated Dynamics and Scheduling for Solar (MIDAS-Solar)

Jin Tan,[1] Andy Hoke,[1] Haoyu Yuan,[1] Bin Wang,[1] Rick Wallace Kenyon,[1] Xin Fang,[1] Przemyslaw Koralewicz,[1] Emanuel Mendiola,[1] Yingchen Zhang,[1] Yilu Liu,[2] Shutang You,[2] Mirka Mandich,[2] Annie Zhao,[2] Jianhui Wang,[3] Shengfei Yin,[3] Yanling Lin,[3] Erik Ela,[4] Vikas Singhvi,[4] Parag Mitra,[4] and Robert Entrike[4]

1 National Renewable Energy Laboratory
2 University of Tennessee, Knoxville
3 Southern Methodist University
4 Electric Power Research Institute

Suggested Citation
Tan, Jin, Andy Hoke, Haoyu Yuan, Bin Wang, Rick Wallace Kenyon, Xin Fang, Przemyslaw Koralewicz, Emanuel Mendiola, Yingchen Zhang, Yilu Liu, Shutang You, Mirka Mandich, Annie Zhao, Jianhui Wang, Shengfei Yin, Yanling Lin, Erik Ela, Vikas Singhvi, Parag Mitra, and Robert Entrike. 2023. *Final Technical Report: Multi-Timescale Integrated Dynamics and Scheduling for Solar (MIDAS-Solar)*. Golden, CO: National Renewable Energy Laboratory. NREL/TP-5D00-85679. https://www.nrel.gov/docs/fy23osti/85679.pdf.

NREL is a national laboratory of the U.S. Department of Energy
Office of Energy Efficiency & Renewable Energy
Operated by the Alliance for Sustainable Energy, LLC

This report is available at no cost from the National Renewable Energy Laboratory (NREL) at www.nrel.gov/publications.

Contract No. DE-AC36-08GO28308

Technical Report
NREL/TP-5D00-85679
April 2023

National Renewable Energy Laboratory
15013 Denver West Parkway
Golden, CO 80401
303-275-3000 • www.nrel.gov

NOTICE

This work was authored in part by the National Renewable Energy Laboratory, operated by Alliance for Sustainable Energy, LLC, for the U.S. Department of Energy (DOE) under Contract No. DE-AC36-08GO28308. Funding provided by the U.S. Department of Energy Office of Energy Efficiency and Renewable Energy Solar Energy Technologies Office. The views expressed herein do not necessarily represent the views of the DOE or the U.S. Government.

Cover Photos by Dennis Schroeder: (clockwise, left to right) NREL 51934, NREL 45897, NREL 42160, NREL 45891, NREL 48097, NREL 46526.

Acknowledgement:
This material is based upon work supported by the U.S. Department of Energy's Office of Energy Efficiency and Renewable Energy (EERE) Solar Energy Technologies Office (SETO) under the SETO Lab Call Award Number 34224. Support for the work was also provided by Hawaiian Electric Companies (HECO) under cooperative research and development agreement no. CRD-20-16630.
The authors thank the project teams from the partner organizations, including the University of Tennessee, Knoxville (Yilu Liu, Shutang You, Mirka Mandich, and Annie Zhao); Southern Methodist University (Jianhui Wang, Shengfei Yin, and Yanling Lin); the Electric Power Research Institute (Erik Ela, Vikas Singhvi, Parag Mitra, and Robert Entriken); and the multiple NREL researchers who conducted extensive research and analysis (Haoyu Yuan, Xin Fang, Bin Wang, Richard Wallace Kenyon, Przemyslaw Koralewicz, and Emanuel Mendiola). Many of these contributors are coauthors in the corresponding papers and reports. Also, we offer a special thanks to those who contributed behind the scenes to set up experiments, manage finances and reporting (Shannon Calkum), and otherwise support these efforts. Thanks also to Barry Mather and Bryan Palmintier for reviewing our publications.

Special thanks as well to our SETO technical managers, Kemal Celik, Jeremiah Miller, Yi Yang, and Guohui Yuan, who supported this project and provided feedback.

The project team thanks the members of the technical review committee for their insightful comments and assistance. Participation in the committee does not imply agreement with the project findings. The committee included Marc Asano (HECO), Li Yu (HECO), Gemini Yau (HECO), Julia Matevosyan (Energy Systems Integration Group), Mark O'Malley (University College Dublin), Clyde Loutan (California Independent System Operator), Xiaochuan Luo (Independent System Operator New England), and Kai Sun (University of Tennessee, Knoxville).

Executive Summary

Solar photovoltaic (PV) installations have experienced unprecedented growth in the United States. PV will become not only an energy producer but also a necessary provider of ancillary services at multiple timescales. Conventional methods to simulate power systems operations—such as long-term production simulation (which typically considers schedules from hours to minutes by using an optimization framework) and short-term transient studies (which simulate dynamics from seconds to sub-seconds using state variables and differential equations)—are not sufficient for studying the multiple-timescale variation of solar generation and its impact on system reliability. Long-term system economics and short-term system dynamics are highly coupled, particularly when the penetration level of renewable generation is extremely high, because the uncertainty and variability of solar generation will impact both power system steady-state and dynamic performance.

This project helps meet and exceed the U.S. Department of Energy Office of Energy Efficiency and Renewable Energy Solar Energy Technologies Office goal of systems integration by directly addressing this stability and reliability challenge for power grid planning and operation. We have developed a temporally comprehensive, closed-loop simulation model, named Multi-timescale Integrated Dynamics and Scheduling (MIDAS), that seamlessly simulates power system operations from economic scheduling (day-ahead to hours) to dynamic response analysis (seconds to sub-seconds). For schedules with very high levels of inverter-based resources (IBRs), up to and including 100%, the stability of grid controls has been evaluated through electromagnetic transient (EMT) simulations and power-hardware-in-the-loop (PHIL) simulations of key transient events at key schedule points. Specifically, MIDAS provides:

- A closed-loop simulation framework for simulating timescales from economic scheduling to dynamic stability analysis
- Machine learning-based stability assessment
- EMT modeling and analysis for large-scale power systems
- MIDAS PHIL test bed.

We worked with Hawaii Electric Companies to apply the MIDAS study framework to a Maui grid study. The entire island's transmission system was modeled in detail—from a yearly scheduling model, to a second-level frequency dynamic model, down to a sub-second-scale EMT model to address critical stability issues.

The project demonstrated how MIDAS can help system planners and operators assess system reliability and stability while the power grid is marching toward a high-renewable, high-IBR future. In this Maui grid study, we found that 100% instantaneous IBR operation is achievable in EMT simulation and PHIL testing, and grid planners and operators might need new analysis/simulation tools to assess grid reliability and stability in the scheduling stage. MIDAS will bring Maui and other systems closer to 100% clean and stable energy futures. (In this study, we examined transient stability. Other topics necessary for 100% IBR operation, such as protection and resource adequacy, were not examined.)

Table of Contents

1 Background 5
1.1 Background and Motivation 5
1.2 Literature Review 5
2 Project Objectives 7
2.1 Objectives 7
2.2 Summary of Tasks 7
3 Project Results and Discussion 9
3.1 Introduction 9
3.2 MIDAS Framework 10
3.3 Integrated Dynamic and Scheduling Model 12
3.3.1 Extended-Term Dynamic Model of PV and Grid 12
3.3.2 Multi-Timescale Scheduling Model Development 16
3.3.3 Interface Between Dynamic and Scheduling Models 17
3.3.4 Full-Dynamic Simulation of Integrated Dynamic and Scheduling Model 19
3.3.5 Quasi-Dynamic Simulation of Integrated Dynamic and Scheduling Model 20
3.4 Use Cases for MIDAS 21
3.4.1 18-Bus Test System 21
3.4.2 Maui Use Case 24
3.5 Large-Scale EMT Model for Maui Grid 31
3.5.1 EMT Modeling of Maui Grid 31
3.5.2 Validation of Maui PSCAD Model 32
3.5.3 Simulation of Low-inertia Scenarios 34
3.5.4 Transmission and Distribution Simulation of Maui Grid 40
3.6 PHIL Testing for MIDAS 40
3.6.1 MIDAS PHIL Test Bed 40
3.6.2 PHIL Testing for GFM Inverter in Low-inertia Grid 41
3.7 240-bus WECC Test System Development 47
3.8 Machine-learning Based Security Assessment 48
3.9 Tools Developed Under MIDAS Project 52
3.9.1 MIDAS Tool 52
3.9.2 DC2AC Tool 54

3.9.3 PSS/E Network Reduction Tool 55
3.10 Technical Summary 55
4 Significant Accomplishments and Conclusions 57
4.1 Featured Accomplishment 57
4.2 High-level Conclusions 58
4.2.1 Learnings from a Multi-timescale Simulation Approach 58
4.2.2 100% IBR Operation is Achievable in EMT Simulation and PHIL Testing . 58
5 Path Forward 60
5.1 System Planning and Operation 60
5.2 Advanced Coordination Between Solar and Storage 61
5.3 Plans for Tools Developed Under the Project 61
5.4 Development of the 240-bus WECC Test System 62
5.5 Community Engagement 63
6 Inventions, Patents, Publications, and Other Results 64
References 69
Appendix 73
6.1 Appendix A – 18-bus 4-areaTest System 73
6.2 Appendix B – Machine-learning based dynamic stability assessment. 73

1 Background

1.1 Background and Motivation

Increasing penetration levels of variable generation (VG) on the power grid will significantly increase the difficulty of balancing power systems operations at multiple timescales due to the reduced inertia and limited frequency reserve. This leads to poor grid frequency performance. For example, the Australian Energy Market Operator (AEMO) reported that the power system frequency remained outside the normal operating range more than 1% of the time during January 2019 [1]. The United Kingdom blackout on August 9, 2019, was exacerbated by low system inertia in power grids with high penetrations of inverter-based resources (IBRs) [2]. To address this, the United Kingdom recently launched a new inertia market design [3] to maintain the system inertia level, but it brings more conventional generation online. Therefore, without considering the fast frequency response capability of IBRs in scheduling, renewable energy will eventually hit a penetration ceiling due to the limited inertia and frequency response from generators.

Solar and wind power plants have been proven to be technically capable of providing frequency control ancillary services (FCAS) through active power control [4-6], including fast frequency control, primary frequency control (PFC), and automatic generation control (AGC).[1] If designed correctly, active power control from VG can have superior frequency regulation performance compared to conventional generators in terms of speed and accuracy because most existing photovoltaic (PV) and wind power plants interface with the power grid through power electronic devices with fast responses [7-9]; however, these advanced controls of PV and other IBRs are rarely considered in practice. Grid operators are not confident in VG being as reliable as traditional FCAS resources—partly due to the lack of a simulation tool to assess the performance of VG providing FCAS, to predict the inherent risk of using VG for FCAS considering VG variability and uncertainty, and to validate the functioning of newly proposed market incentives for VG-based FCAS.

As more renewables are integrated into electric grids, there is an increased interest in market designs to incentivize VG to be scheduled to provide fast FCAS [6, 10] (minute- to hour-level time resolution). There is also a need to evaluate the deployment of FCAS provided by VG and its performance in frequency dynamics (second-level time resolution). Therefore, in this project, we introduce a novel multi-timescale framework to study the performance of VG providing FCAS, named Multi-timescale Integrated Dynamics and Scheduling (MIDAS). Using this framework, two key issues are addressed: (1) the cost and reliability benefit of using PV to provide FCAS and (2) the risk of using PV to provide multiple FCAS.

1.2 Literature Review

Current commercial software for power system analysis is typically designed for specific

[1] *AGC* is a preferred term in North America for secondary frequency control. Within the Union for the Co-ordination of Transmission of Electricity (UCTE), secondary frequency control is called *load-frequency control*. The term *AGC*, however, designates the combination of dispatching and secondary frequency control within UCTE.

applications. For example, PLEXOS is widely used for production cost modeling, and PSS/E and PSLF are well-known for transient dynamic analysis. These tools and their approaches work well to tackle problems in traditional power systems. But the new problems and challenges brought on by high penetrations of renewable generation have fundamentally changed the interactions among operations at various timescales.

In recent years, some efforts have been made to combine multiple specific-timescale simulation modules into one platform. Reference [11] suggested that PSS/E can perform a new function, called extended-term dynamic simulation, to extend dynamic simulations to a virtually unlimited time frame, and the authors implemented slow-moving controls. This new feature has been used to test compliance with standards (e.g., CPS1 and CPS2) and evaluate the impact of renewable generation on system frequency performance [11]; however, the steady-state set points of the system cannot be realistically evaluated without knowledge of the economic scheduling. KEMA Inc. published the Renewable Energy Modeling and Integration Tool (KERMIT) to simulate power system frequency behavior for 24 hours, but it does not include economic scheduling. In the current industry practice, market operation is totally independent of dynamic simulation, but with the increasing FCAS from VG proposed for the future power grid, it becomes necessary to simulate the interactions between the reserve scheduling and the reserve deployment through dynamic controls. NREL's Flexible Energy Scheduling Tool for Integrating Variable Generation (FESTIV) can simulate the behavior of the grid from unit commitment to AGC; however, it adopts a simplified area control error (ACE) calculation and provides only steady-state frequency [12]. Additionally, some studies investigate the adequacy of wind generators providing all-timescale frequency response services by simulations from either the dynamic or market perspective [13, 14]; however, thus far, they cannot bridge economic scheduling and system dynamic performance.

Although the technical capability of providing FCAS with IBRs has been tested and proved, the related FCAS market models for IBRs in the current independent system operator (ISO) market in the United State are still under discussion. A new primary frequency response (PFR) market has been proposed and developed to host the reserve for short-term primary frequency support [15, 16].

2 Project Objectives

2.1 Objectives

The MIDAS-Solar project developed both a multi-timescale grid model and an integrated PV model to seamlessly simulate solar PV variability and its impact on power systems operations from economic scheduling timescales (day-ahead to hours) to dynamic response analysis (seconds to sub-seconds).

For schedules with very high levels of IBRs, up to and including 100%, the stability of grid controls were evaluated through targeted electromagnetic transient (EMT) simulations and power-hardware-in-the-loop (PHIL) simulations of key transient events at key schedule points.

2.2 Summary of Tasks

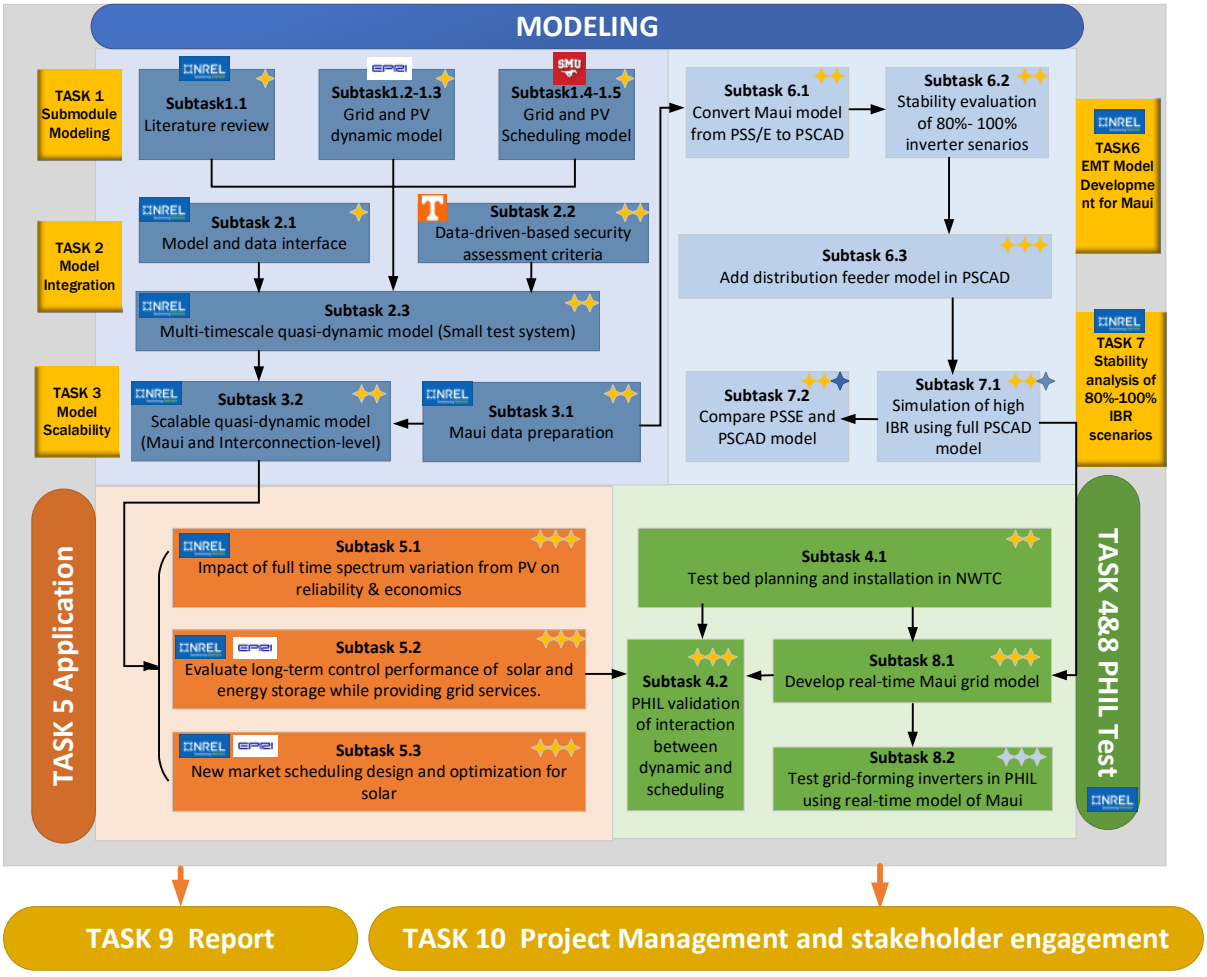

Figure 1. Subtasks and flowchart of the MIDAS project

To achieve the project objectives, we divided the technical work into three parts: **modeling**, **validation,** and **application**, as summarized in Figure 1. First, the proper

submodules of the grid and PV models were separately developed to ensure the **fidelity** of each device model at different timescales—from the day-ahead scheduling timescale, to the seconds-level EMT dynamics, to the millisecond-level EMT dynamics of the power grid and PV inverters (Task 1 and Task 6).

To study the interactions among the economics, reliability, and stability of a high-PV grid, the submodules from Task 1 were efficiently integrated to realize the novel multi-timescale, quasi-dynamic test model and simulation scheme (Task 2). To test and refine the **scalability** of the proposed model, multi-timescale models were implemented in more realistic grids, including the Maui grid and the Western Electricity Coordinating Council (WECC) 240-bus test system (Task 3). Task 5 demonstrated the applicability of the multi-timescale approach to three relevant applications drawn from impact analysis, control, and market design domains.

To study the stability of an IBR-dominated grid, the full EMT model of the Maui grid was developed. In addition, distribution feeders were modeled to study the interactions between the transmission and distribution systems (Task 6).

Both the proposed multi-timescale model and EMT model of the Maui grid were validated and tested through PHIL (Task 4 and Task 8).

3 Project Results and Discussion

3.1 Introduction

Increasing penetration levels of renewable generation on the power grid will significantly increase the uncertainty of balancing power systems operations at multiple timescales. From market-based economic scheduling to frequency dynamics, all operation statuses will be impacted by the response of renewable generation to various dispatch and control signals, as shown in Figure 2. To ensure the security and reliability of the grid operation, various renewable sources—such as solar, wind, and batteries—will be required to provide various ancillary services, and additional market incentives will be needed to encourage renewables to provide these services.

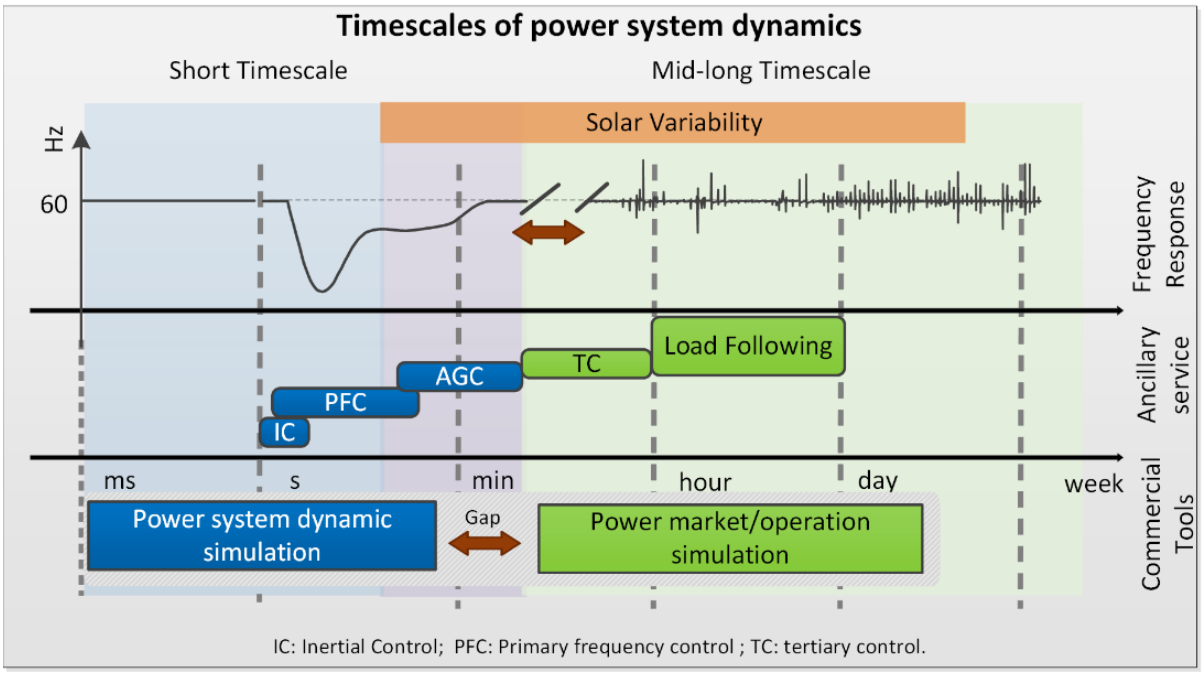

Figure 2. Timescales of power system dynamics and commercial software

The current commercial software for power system analysis are designed for one-timescale, isolated applications. For example, PLEXOS is for wholesale market simulations, and PSS/E and PSLF are for transmission electro-mechanic dynamic simulations. These tools and their approaches work well to tackle problems in traditional synchronous generator-dominated power systems. But considering the new problems and challenges brought by high penetrations of renewable generation, the interactions between various-timescale operations has fundamentally changed. For example, in the future, ISOs might encourage renewable generation to provide primary or secondary frequency ancillary service to improve the system reliability by developing new market rules. In this case, accurately capturing both the market operation and the frequency dynamic features in one platform will become an urgent requirement.

Different commercial software anin-house tools are summarized in Table 1 based on their target timescales.

Table 1. Comparison of Different Tools for Multi-Timescale Simulations

	Vendor	Transient	AGC	Extended-Term	Economic Dispatch	Day-Ahead Unit Commitment	Planning
PSS/E [1]	SIEMENS						
PLEXOS	Energy Exemplar						
KERMIT [2], [3]	KEMA						
IGMS[4]	NREL						
FESTIV[5]	NREL						
MAFRIT [6], [7]	NREL						
MIDAS	NREL						

Capable Capable but not well developed

Based on Table 1, the current commercial software is limited to one time resolution and research tools are not capable of covering the studied full-time-spectrum of solar variation, therefore they cannot analyze the variability and uncertainty impacts across different operational timescales. In this project, we propose an integrated model MIDAS that can perform efficient time-domain simulations over a broad range of phenomena—from fast control systems with a time constant, to transient dynamics (10 milliseconds), to load-following and scheduling timescales of up to 24 hours as shown in Table 1 . To simulate multiple time resolution, MIDAS integrate all the sub-scheduling programs and dynamic simulation in practice into one simulation framework with flexibility to test different scheduling strategies impact on economics, reliability and stability of grid operation simultaneously.

3.2 MIDAS Framework

The MIDAS framework is shown in Figure 3. It represents the evolution of active power balance and frequency control at different timescales: (1) mid- to long-term economic dispatch based on the load and renewables forecasting models; (2) multi-area AGC for renewable power plants, including a dynamic AGC dispatch model at the level of seconds (e.g., consider a PV power plant); and (3) a grid frequency response dynamic model that includes a primary and secondary frequency controller. The framework has been divided into three parts: the extended-term dynamic simulation model, the scheduling model, and the data-driven-based stability assessment model.

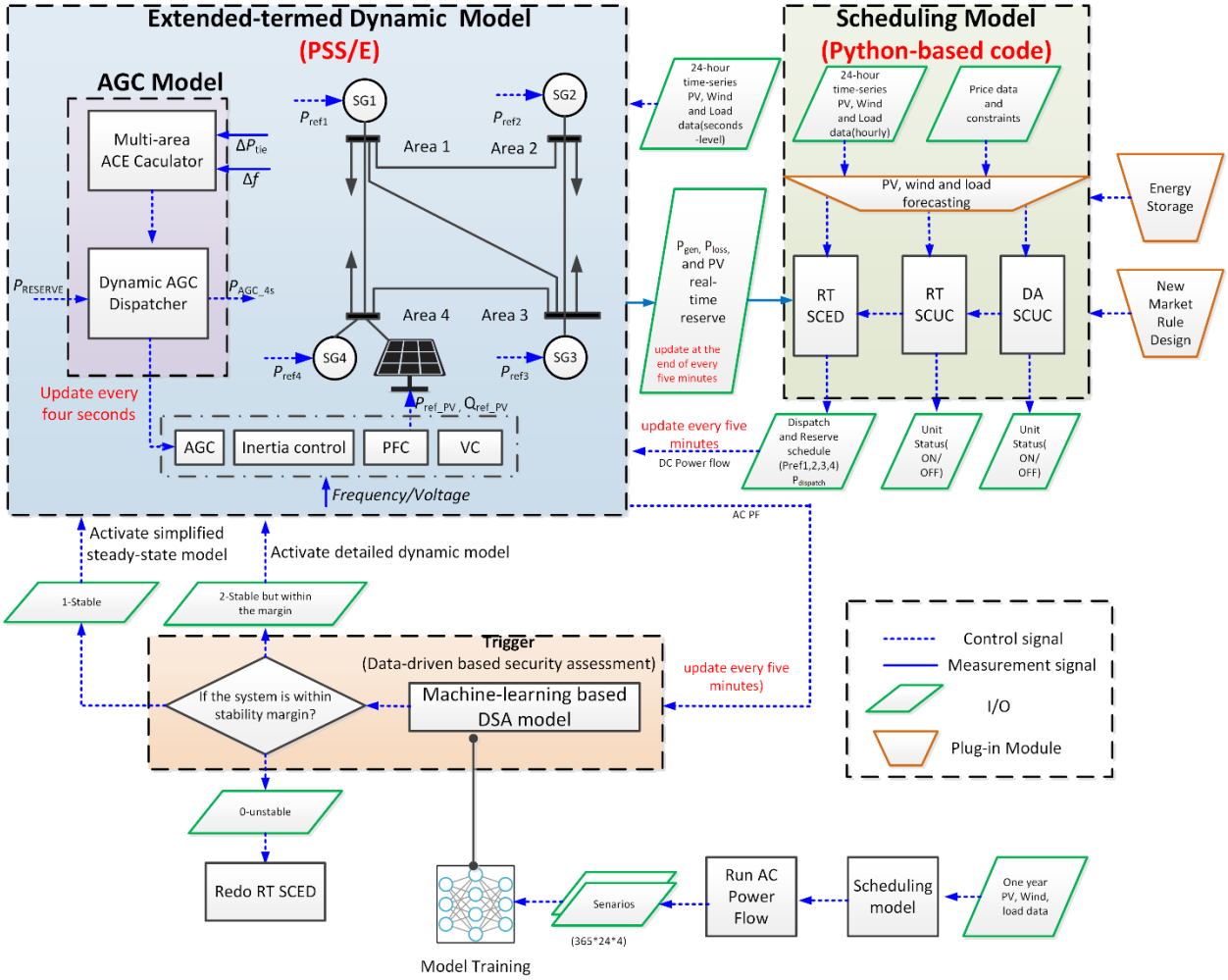

Figure 3. Refined MIDAS framework

The extended-term dynamic simulation model was implemented using the PSS/E platform; however, an AGC block and extended-term dynamic model for PV that can capture the variation in solar irradiance and advanced control functions are not included in PSS/E. Thus, it is required to separately develop a user-defined model for AGC and advanced control functions for PV. The dynamic model will be continually running for 5 minutes, and at the last time step, we will send the real-time power flow, system loss, and reserve of PV back to the scheduling model. In this way, the scheduling model will get an accurate awareness of the system's current operation point.

The scheduling model integrates multiple scheduling submodules—including day-ahead security-constrained unit commitment (DASCUC), real-time security-constrained unit commitment (RTSCUC), and real-time security-constrained economic dispatch (RTSCED)—with the flexibility to study different scheduling strategies. PV and energy storage are considered in this model. New market rules will be designed and flexibly plugged into the base model. The input and output are described in Table 2.

The Dynamic Stability Assessment (DSA) model was divided into two parts: an offline training data set and an online application for integrated model. One-year hourly PV, wind, and load data are needed for the test system. Steady-state power flow is calculated by the scheduling model, and the convergence is tested by the AC power flow. Then it created the training scenarios for the machine learning algorithm. Once the machine learning-based model is done and tested, it is directly used in our integrated model. The input and output are described in Table 2.

Table 2. Input and Output of Sub-Models

		Input	Output
Scheduling Model		1) At least 24-hour hourly PV, wind, and load data 2) Price data and constraints 3) System data 4) Real-time power flow, system loss, and reserve of PV every 5 minutes	1) 5-minute economic dispatch and reserve 2) ON/OFF status of units
Extended-Term Dynamic Model		1) At least 24-hour, PV, wind, and load data in second time resolution. 2) 5-minute economic dispatch and reserve	1) Real-time power flow, system loss, and reserve of PV every 5 minutes
DSA Model	Online	1) Power flow data from scheduling model or dynamic model	1) Trigger decision
	Offline	1) One-year hourly PV, wind, and load data 2) System power flow and dynamic data	1) 365*12*4 training scenarios 2) Machine learning-based model

The innovations of this simulation framework include: (1) the coordinated, closed-loop, multi-timescale simulation of the scheduling model and the extended-term dynamic model; (2) an improved dispatch submodule that can dynamically optimize the generators' power outputs while receiving the real-time output of the generators based on both the reserve deployments in the dynamic model and the real-time AC-based line loss; and (3) an extend-term dynamic model that can accurately capture the full spectrum of the grid frequency dynamics by updating the generator set points and the reserve dispatch from the scheduling model and integrating the multi-area AGC model, time-series load data, and solar data. More details are discussed in following section.

3.3 Integrated Dynamic and Scheduling Model

3.3.1 Extended-Term Dynamic Model of PV and Grid

3.3.1.1 Photovoltaic Variability Modeling

The variability of VG occurs at multiple timescales—from seconds, to minutes, to hours—and it requires the movement of other resources to ensure the balance of generation and load. It is important to capture the multi-timescale variability from PV. In this section, we

developed an approach to model the power output variability of utility-scale solar PV power plants and to incorporate the variable power output in the dynamic simulations.

Integration of Solar Plant Output Profile in PSS/E Dynamic Simulations: In this project, we uses WECC's second-generation, utility-scale solar PV models—namely, regca1, reecb1, and repca1—to model the dynamic behavior of a solar PV plant. The repca1 model, which represents the solar power plant controller, includes a variable called Plant_Pref that is normally initialized at the beginning of a dynamic simulation and remains unchanged during the simulation. It can, however, be changed using the Python application programming interface of PSS/E. We used this capability of PSS/E to change the Plant_Pref according to the power plant real power output profile.

3.3.1.2 Automatic Generation Control Modeling

In this section, an automatic generation controller and the plant controller models are developed. In addition to the existing plant controller, a new model was developed for PSS/E that allows the second-generation renewable energy plant control (REPC) model to receive the area megawatt command generated by the AGC module. The new model was included in the 18-bus, 4-area system with a PV generation plant, and the action of AGC for a load disturbance was tested.

The primary objectives of AGC are to regulate frequency to the specified nominal value and to maintain the interchange of power between the control areas at the scheduled value. The block diagram of a simple AGC controller is shown in Figure 4.

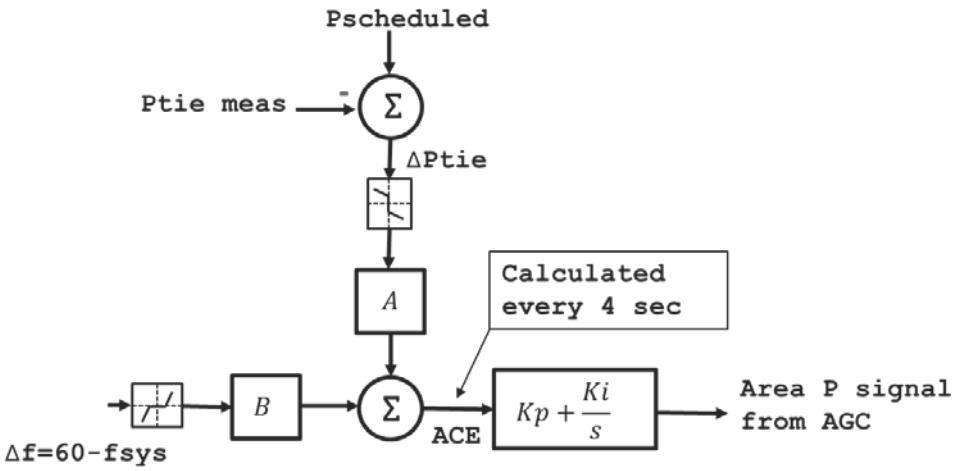

Figure 4. Block diagram of AGC controller

The AGC controller uses the frequency and tie-line flow deviation (from the prescheduled value) to generate the ACE signal. The ACE signal is given by:

$$ACE = (NI_s - NI_A) - 10B(F_A - F_s) - I_{ME}, \quad (1)$$

where:

- NI_S and NI_A are, respectively, the scheduled and the actual net area interchanges.
- F_S and F_A are, respectively, the scheduled and the actual system frequency.
- B is the balancing authority bias (a negative number in MW/ 0.1Hz).
- I_{ME} is the interchange metering error.

The inverter-based generation units in PSS/E are modeled by using the second-generation renewable models, also known as the RE models. Because the plant-level controller already exists for the inverter-based generation module, we developed a separate module that enables the REPCA1 model to communicate with the AGC model in the area. Figure 5 shows the plant controller auxiliary module for the renewable generation unit. Similar to the conventional plant controller described in the preceding subsection, this auxiliary module gets the area megawatt command from the AGC module in the area and determines the plant output based on the parameter Frac. The plant controller model shown in Figure 5 was developed as a user-defined model in PSS/E, and it is available as a dynamic linked library.

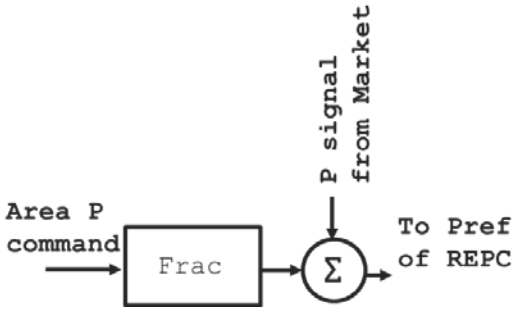

Figure 5. Block diagram of the plant controller auxiliary module for inverter-based units

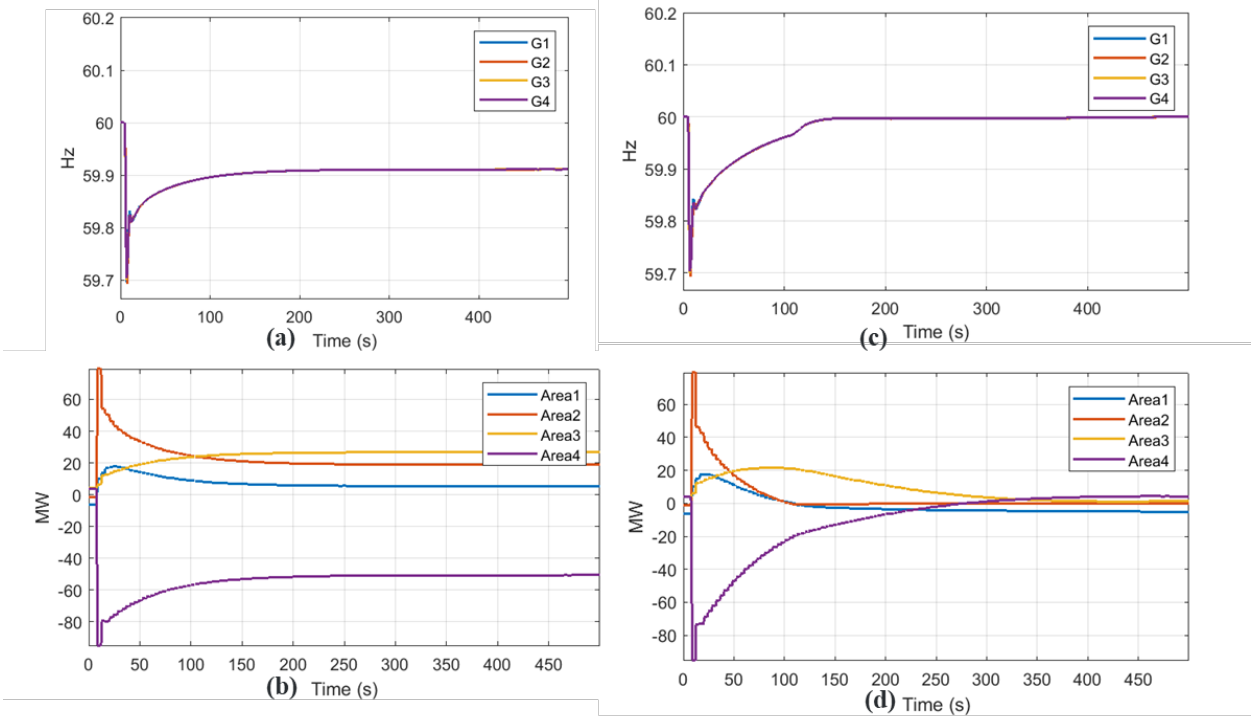

Figure 6. (a) Frequency (generator speed) recovery without AGC, (b) tie-line flows without AGC, (c) frequency recovery (generator speed) with AGC, and (d) tie-line flows with AGC

To validate the performance of the developed models, a frequency event was simulated in the 18-bus system. To create a sudden frequency drop, the load in Area 4 was increased by 100 MW in a step. The simulations were repeated with and without the AGC control to illustrate the difference between the frequency recovery and power sharing.

Figure 6 (a) and (b) show the frequency (generator speeds) and the tie-line flows, respectively, when the generators provide only PFR and no AGC action is modeled. Figure 6 (c) and (d) show the frequency (generator speeds) and the tie-line flows, respectively, when the generators provide both PFR and secondary frequency response via AGC action. As expected, with the AGC control enabled, the system frequency is restored to 60 Hz, and the tie-line flows are restored to the prescheduled values.

3.3.1.3 Load Tap Changer and Switched Shunt Modeling

Load tap chargers (LTCs) and switched shunts (SWs) are important devices in extended-term simulations. For example, during peak hours, when the system needs additional reactive support, LTCs need to change the tap positions to increase the load-side voltage, and the switched shunts need to be switched in to provide reactive support. On the other hand, during valley hours, overvoltage might be an issue. LTCs need to change the tap positions to reduce the load-side voltage, and the switched shunts need to be switched out. The normal transient dynamic test systems not come with any LTC or switched shunt

models. As a result, some dispatch results from the scheduling model do not lead to a feasible AC power flow solution. In addition, the dynamic model “SWSHNT” and “OLTC1T” are used for the switched shunts and LTC, respectively.

A simple load increase scenario was simulated in the 18-bus test system [28] to verify the effectiveness of the added voltage control devices. In the simulation, we increased the load at Bus 13 at a fixed rate of 1 MW/second for 200 seconds, as illustrated in Figure 7(a). The voltages of the Area West buses are shown in Figure 7(b), where Bus 13 had the lowest voltage, just above 0.98 p.u., which is the control lower bound of the LTC. As the load increased, the voltage dropped below 0.98, where it remained for approximately 50 seconds. The LTC started to change the ratio to increase the voltage of Bus 13. Seven taps were adjusted consecutively from 50 seconds to 110 seconds; however, the voltage was still below 0.98 p.u. In the meantime, the voltage of Bus 14 (red curve), the high voltage side of the LTC, kept dropping as the tap changed and dropped below 0.98 p.u. at approximately 110 seconds. This triggered the switched shunts to switch in one step, i.e., 100 MVar, which eventually increased the voltage of both Bus 13 and Bus 14.

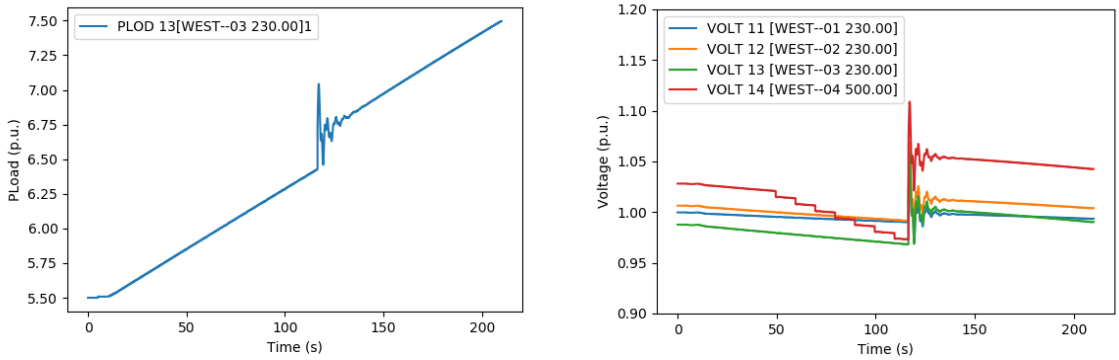

(a) Load increase (b) Voltage profile

Figure 7. Load increase simulation

3.3.2 Multi-Timescale Scheduling Model Development

The MIDAS generation scheduling tool includes day-ahead unit commitment (DAUC), day-ahead economic dispatch (DAED), real-time unit commitment (RTUC), and real-time economic dispatch (RTED). The framework of the MIDAS generation scheduling tool is shown in Figure 8. DAUC and DAED will be run every 24 hours with an hourly resolution. RTUC will be run every hour with a 3-hour time span and an hourly resolution. RTED will be run every 5 minutes with a 2-hour time span and a 5-minute interval. In the advanced version of the MIDAS generation scheduling tool, the time resolution—the time span of RTUC and RTED—can be changed by the operators. Note that if the time resolution of RTUC and RTED is changed to other values instead of the default ones, the input data of RTUC and RTED should be changed accordingly.

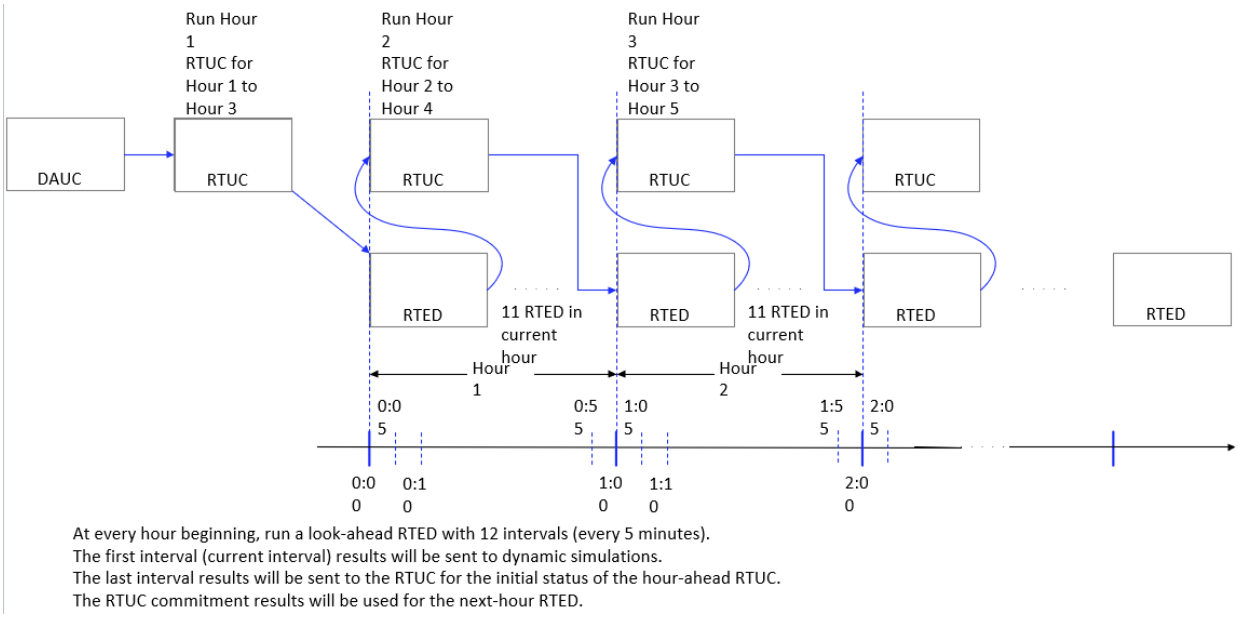

Figure 8. Framework of the MIDAS generation scheduling tool

Figure 8 also shows that each module of DAUC, DAED, RTUC, and RTED is coupled with the other. So, the scheduling of one module can impact the scheduling of the following modules. This framework can help capture the impacts of the inter-interval and intra-interval renewable energy variations on the generation scheduling. The detailed mathematic formulation of each module can be found in [1], [2].

3.3.3 Interface Between Dynamic and Scheduling Models

The interface design is shown in Figure 9. The components for the integrated simulation are represented using blue. The rest of the flowcharts represent the data flow of the extended time dynamic (ETD) simulations (left) and scheduling model (right). The figure shows that the ETD and scheduling model are running in parallel and act as two agents. The two models/agents are exchanging data through a shared folder for each RTED interval, i.e., 5 minutes. Two flags, i.e., ETD flag and SCED flag, are used to coordinate the two models when advancing in time. The proposed design coordinates the two models through two flags and interchanges the data through a shared folder.

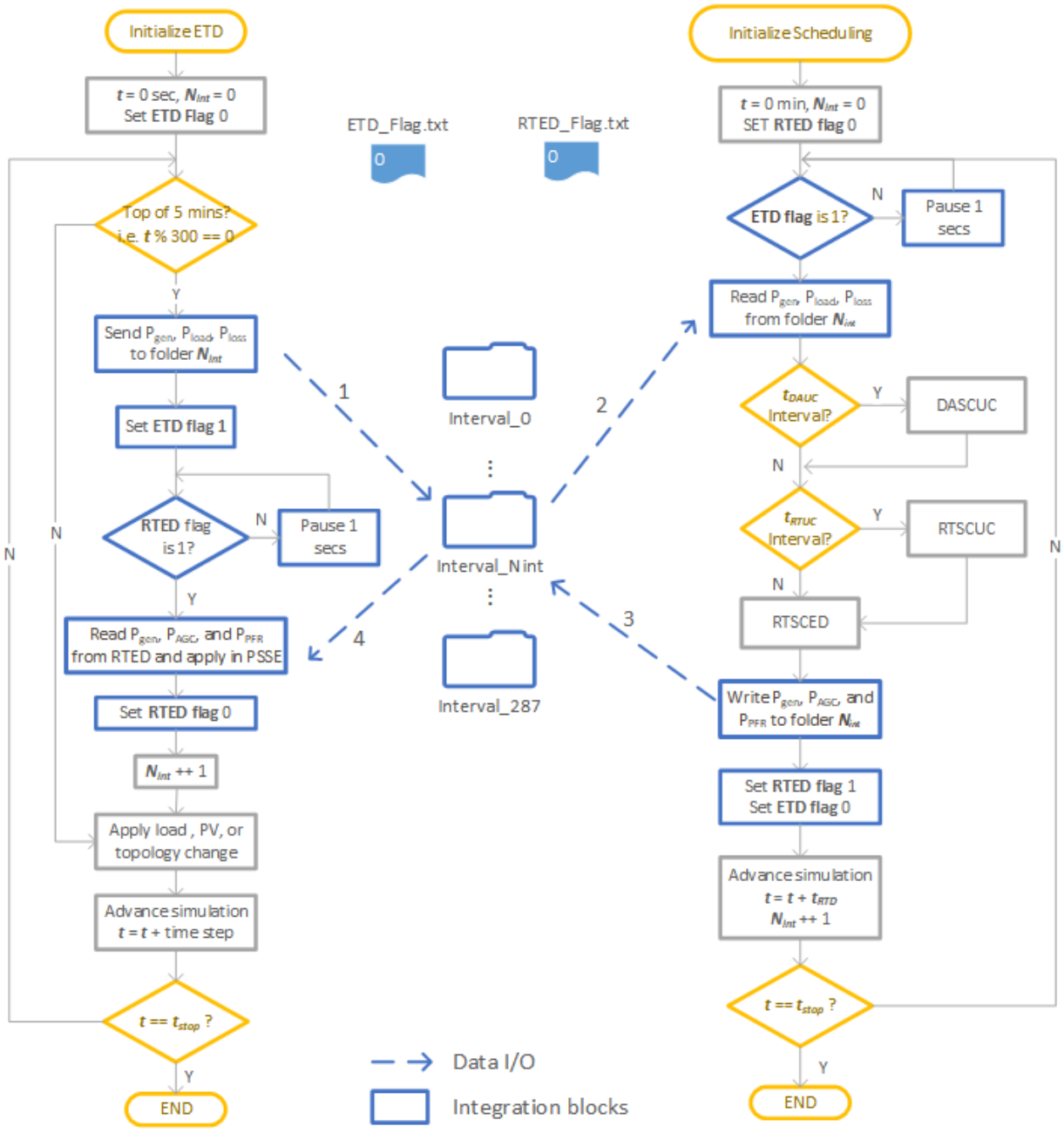

Figure 9. Interface design for integrated dynamic and scheduling model

The advantage of such a design is that the ETD model and the scheduling model do not need to be developed in the same environments and can be debugged and compiled independently. This grants both the ETD team and the scheduling team a high level of flexibility in developing their module. Moreover, when migrating to a utility partner's system, such a design is flexible in adapting to an ETD model or a scheduling model in a completely different platform.

3.3.4 Full-Dynamic Simulation of Integrated Dynamic and Scheduling Model

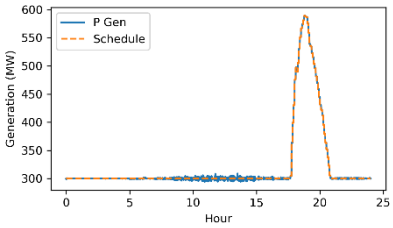

Figure 10. Gen 101 output

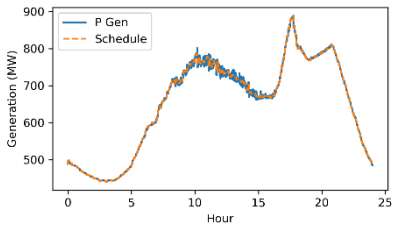

Figure 11. Gen 111 output

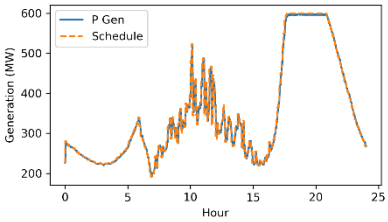

Figure 12. Gen 231 output

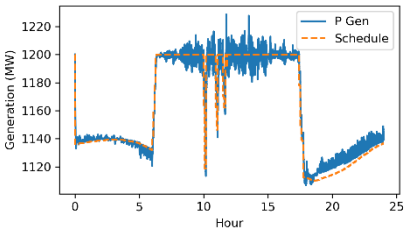

Figure 13. Gen 311 output

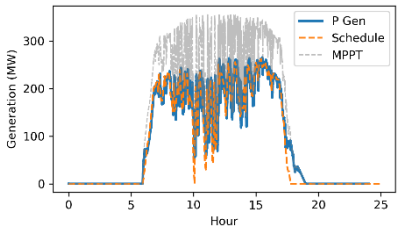

Figure 14. PV generation output

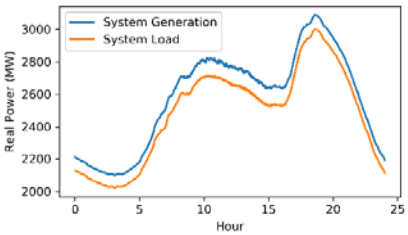

Figure 15. System generation vs. load

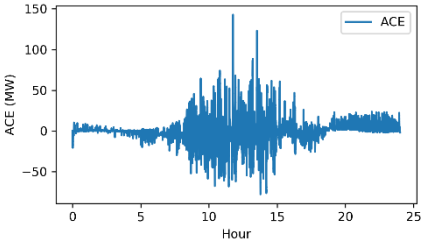

Figure 16. System ACE

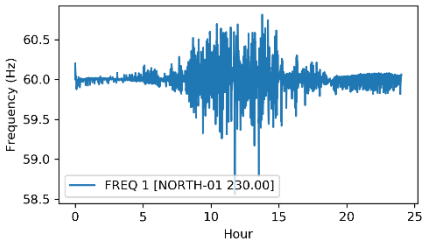

Figure 17. System frequency

After the integrated simulation design is implemented, a test run on the 18-bus system is performed. The description of the test system is presented in Appendix A. In this run, the generator at Bus 311 and the PV generator at Bus 312 can provide the regulation-up and regulation-down service, and the PV is using the cloudy day high-variation profile. The 24-hour plots are shown in Figure 10 to Figure 17. It is shown that the generators (blue lines) are closely following the scheduling results (dashed red lines), which means that the integrated simulation is performed as expected and can simulate up to 24 hours. The purpose of this test is to validate the accuracy of the integrated dynamic and scheduling

model.

3.3.5 Quasi-Dynamic Simulation of Integrated Dynamic and Scheduling Model

In this section, we integrated the DSA results from Section 3.8 with the dynamic simulation by using the DSA results to inform the choice of different integration sizes. As will be demonstrated, the variable-time step size simulation speeds up the simulation while maintaining high accuracy.

Three simulation runs are performed on the same sequence of events using different integration step sizes: named **Size 1**, **Size 2**, and **Variable**.

Size 1 step size: We use a quarter cycle, i.e., 0.00416667 second, as the integration step in this simulation run. We consider the results from this run the ground truth of this sequence of events.

Size 2 step size: We use four cycles, i.e., 0.025 second, as the integration step in this simulation run. This is the largest step size that the simulation can run.

Variable step size: We use a quarter-cycle step size for the intervals DSA flag as having an insufficient stability margin (orange dots) as well as intervals with events (green and red dots). For the other intervals (blue dots), we switch to a four-cycle step size.

The three runs are summarized in **Table 3**. For computational speed, Size 1 takes 1,390 seconds (~23 minutes), and Size 2 takes 734 seconds (~12 minutes), which is a 1.89-times speedup; however, using the large step size will introduce significant errors (we define the differences from the Size 1 run as errors) in the frequency-related metrics, such as the CPS1 score. The CPS1 score estimated by the Size 2 run is 10% higher, which is overly optimistic. On the other hand, the Variable step size achieves a 1.66-times speedup but maintains high accuracy compared with the Size 1 run—only a 1% difference in CPS score.

The errors of the minute-level frequency-related compliance factor are presented as a box plot in Figure 18. Compliance factors are the fundamental elements used in calculating CPS1 and can be thought of as the frequency control errors of each minute. The box here depicts the 5th and 95th percentiles of the error distribution, and the whiskers (the solid lines extending beyond the box) represent the 1st and 99th percentiles. All dots are the remaining 2% percentile. Even though the medium value of both Size 2 and Variable size are both close to zero. It is clear that Size 2 tends to bring large errors when underestimate the compliance factor, i.e., the frequency errors, according to the asymmetric distribution. On the other hand, variable step size gives a nicely symmetric distribution and [5, 95] percentiles of the errors (shown by the box) are confined to a very small region.

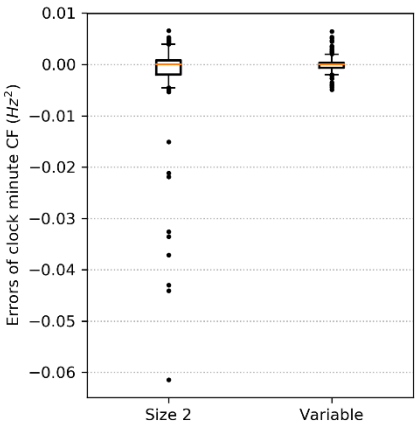

Figure 18. Statistics of compliance factor errors

Table 3. CPS1 Scores and Generation Costs

Step Size	Size 1	Size 2	Variable
Time (s)	1390.90	734.26	833.38
Speedup	N.A.	1.89	1.66
CPS1	88.15%	98.02%	89.19%
BAAL	28	28	28

Another observation is that even though Size 2 has a large error distribution, its [5, 95] percentiles are still relatively small. This, in turn, illustrates the importance of having the DSA to choose the proper small percentage of intervals to use small integration steps.

In summary, (1) the DSA results are integrated to inform the dynamic simulation to choose the proper integration step size; (2) the variable step size can speed up the simulation while maintaining good accuracy in assessing the system frequency response; and (3) a 1.6-times speedup is achieved in the 18-bus system. Even though the absolute reduction in terms of simulation time is on the scale of 10 minutes, the potential savings on a big system could be much more significant.

3.4 Use Cases for MIDAS

3.4.1 18-Bus Test System

To study the impact of PV and the performance of PV providing FCAS, we use the multi-timescale integrated model with the methodologies and metrics as described Section 3.3. Further, the use cases are developed to reveal the unique findings to understand the possible risks, challenges, and interactions between economics and reliability.

3.4.1.1 18-Bus Test System Introduction

We apply the proposed model to a modified four-area test system, as shown in Figure 19. It consists of 18 buses, 24 branches, and 6 transformers, with 7 loads, totaling 3,218 MW. The system includes four generators (one in each area), two hydropower plants, one coal power plant, and one gas power plant. Four equivalent generators are modeled as AGC-enabled generators. The load and wind profiles are obtained from a real power system on a typical day. More information about the 18-bus test system can be found in Appendix A. The MIDAS integrated model is implemented in a joint PSS/E and Python environment.

The parameters of the scheduling modules are summarized in **Table 4**.

Table 4. Typical Parameters of Scheduling Modules

Submodule	*Dispatch Time Step*	*Look-Ahead (h)*	*Refresh (Time per Day)*	*Load and Solar Forecast*
DASCUC	1 hour	24	1	Daily
RTSCUC	1 hour	3	24	Hourly
RTSCED	5 min	2	288	5-min

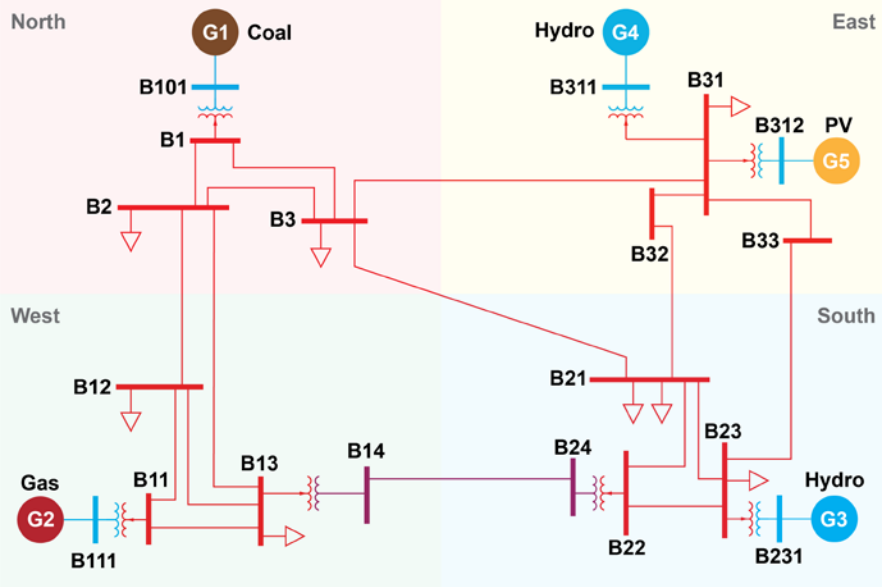

Figure 19. One-line diagram of the 18-bus system

3.4.1.2 Impact Analysis of Full-Time Spectrum Variation from Solar

To study the impact of the variability of renewable generation on system frequency, cases on a sunny day and a cloudy day are compared by assuming that all forecasts are perfect over the length of the scheduling interval. For the cloudy data, we adopt the 1-second real solar power variation data from the Maui grid and scale it up to match our system. 3% regulation reserve has been used in the scheduling model. Figure 20 (a) and (b) show the solar output power for 1 day. The closed-loop simulation of the integrated model gives the 24-hour continual dynamic simulation of the grid frequency, as shown Figure 20 (c) and (d), which clearly show that the grid frequency is much worse on a cloudy day than a sunny day.

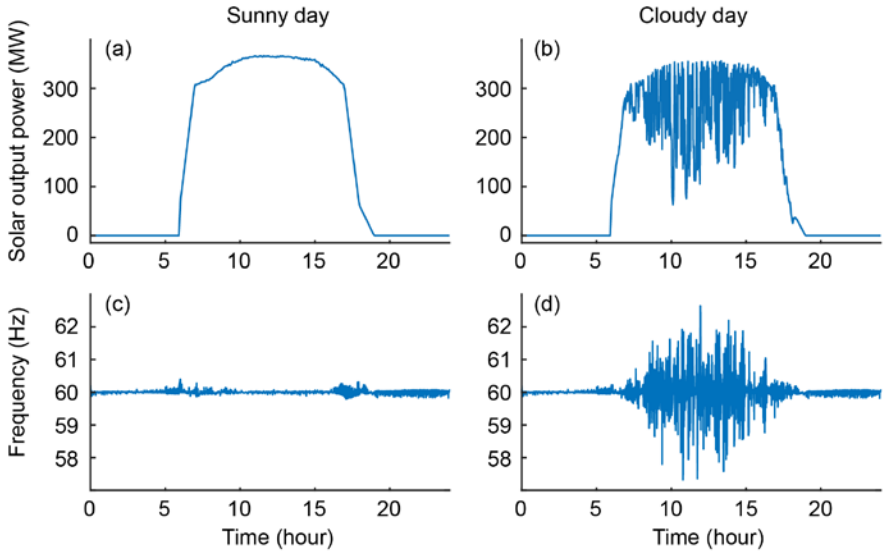

Figure 20. Comparison of output power and grid frequency

CPS and BAAL (Balance Authority ACE Limit) violation scores are used to quantify the reliability, as shown in **Table 5**. On the sunny day, the CPS score is 198% and no violations occur. However, on the cloudy day, the CPS score is 92.3%, and the BAAL has as many as 48 violations. This means that when we use the 3% regulation reserve requirement for grid operation, it might be more than enough on a sunny day but not enough on a cloudy day. This implies that there might be a need for an adaptive regulation requirement based on the weather and system operational conditions.

Table 5. Comparison of Metrics: Sunny Day vs. Cloudy Day

	Sunny Day	***Cloudy Day***
CPS1	198%	92.3%
BAAL Viol.	0	48

In addition, on the cloudy day, the solar variation can cause a significant frequency deviation that is larger than the deadband of the PFC. If this occurs regularly, it can lead to inadequacy of the PFR and increase the risk of underfrequency load shedding if a contingency occurs.

3.4.1.3 Summary

More related use cases in the 18-bus test system can be found in a journal paper under submission [29], including 1) effects of control modes of PV during a cloudy day; 2) Interaction between PFR and AGC; 3) Fast- vs. slow-response resources for regulation.

The main conclusions are as follows:

1) In an electric grid with high penetrations of PV, the traditional regulation requirement might be enough for sunny day, but it might not be enough for a cloudy

day. Thus, adaptively define the system reserve requirement based on system operational status and weather conditions will be recommended.

2) Advanced frequency controls of PV can improve the frequency reliability metrics by providing FCAS under a perfect forecasting scenario, while the reserve adequacy from PV needs to be considered and controlled from both the scheduling and control perspective. When PV is providing stacked PFR and AGC reserve, there is a risk of overtaking the other reserve during the ramp of sunset or sunrise and it might result in insufficient PFR and AGC when needed.

3) PV has a better tracking performance than gas and hydro in AGC regulation. The results show that fast response inverter-based resource is a good candidate for FCAS provider, while it needs detailed economic analysis for a specific system, by considering the trade-off between opportunity cost and revenue gained from FCAS.

3.4.2 Maui Use Case

3.4.2.1 Maui System Description

Maui is likely to become the first interconnected electric transmission system anywhere to operate with 100% wind and solar PV power on an instantaneous basis. Through 2024, Maui is scheduled to bring online more than 175 MW of new solar storage hybrid power plants. In addition to the almost 200 MW of wind and solar presently on the grid, this will be enough renewable power to supply Maui's roughly 70,000 customers (i.e., gross load of 140 MW–200 MW) without using conventional generation for many hours in the year; however, the operability of 100% inverter-based power systems has not been demonstrated in the field.

3.4.2.2 Strategy of PV and Battery Energy Storage Providing Ancillary Services

(1) Methods

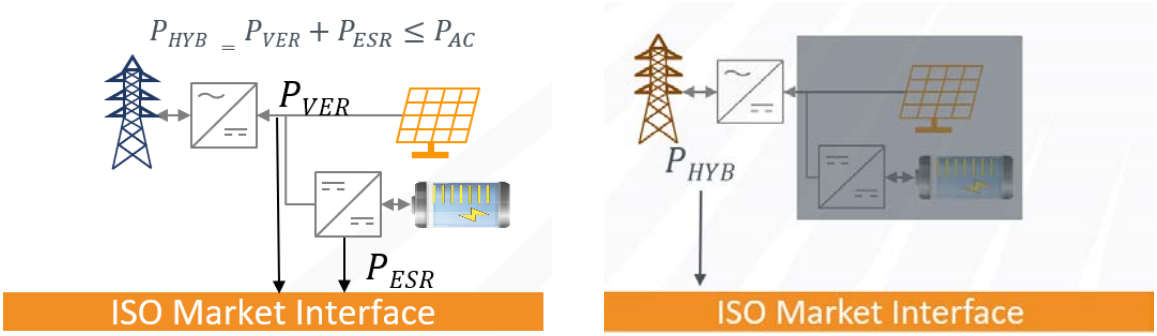

(a) Separate independent resources. (b) single hybrid resource, self-management.

Figure 21. Two operation modes of a hybrid PV power plant

The same hybrid resource could have different electricity market participation modes. From the system operator's view, different participation modes mean different situational awareness, modeling complexities, controllability, and telemetry requirements. In our

study, we explore two participation modes for a hybrid PV power plant, as shown in Figure 21. One is to treat the PV and the battery as separate independent resources (Case 1), and the other is to treat them as a single hybrid resource as a black box for the system operators (Case 2). The coordination between the PV and the battery will be taken care of by the plant owner.

For the single hybrid resource, the hybrid PV and battery plant (HPP) can be treated as a single integrated resource. From the ISO/regional transmission operator perspective, they want to treat the HPP as a conventional generator. This mode is simple to implement and easy to avoid considering the state-of-charge (SOC) management of the battery and PV forecast; however, the challenges will be transferred to the plant owners because they need to manage the PV and battery at the plant level while providing capacity limits and bids for the whole entity.

In this study, two operation modes of an HPP are implemented in both the MIDAS scheduling tool and the dynamic simulation tool. The advanced controllers are implemented on the PV and battery to participate in different reliability ancillary services.

In Case 1, the PV and battery are scheduled independently. Two sets of set points are sent from the system operator (SO) to the PV and the battery energy storage system (BESS), as shown in Figure 22. The ISO will need the PV forecast and will actively manage the SOC of the BESS.

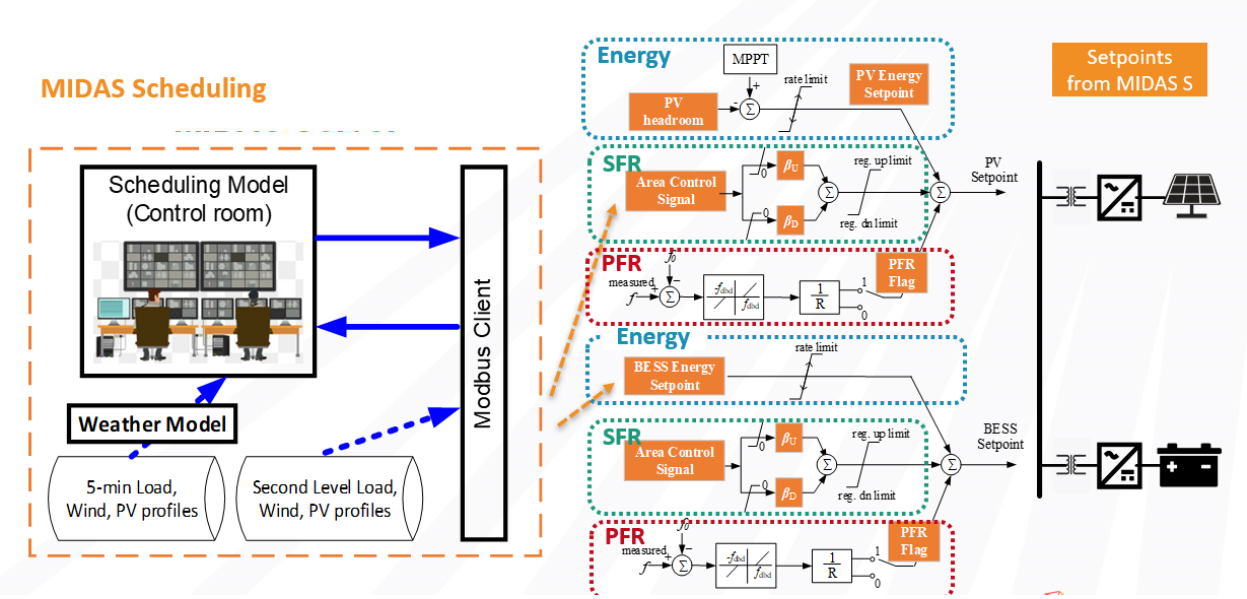

Figure 22. Controllers' implementation for the model of the separate independent resources

In Case 2, one set of set points is sent to the HPP. The plant level control distributes the HPP set points to the PV and BESS, respectively, to fulfill the energy, secondary frequency response (SFR), and PFR obligations. In our study, we implemented the coordination control strategy by running the PV at maximum power point tracking (MPPT) and using the BESS to fulfill the remaining energy obligation and the full amount of the

SFR and PFR obligations, as shown in Figure 23.

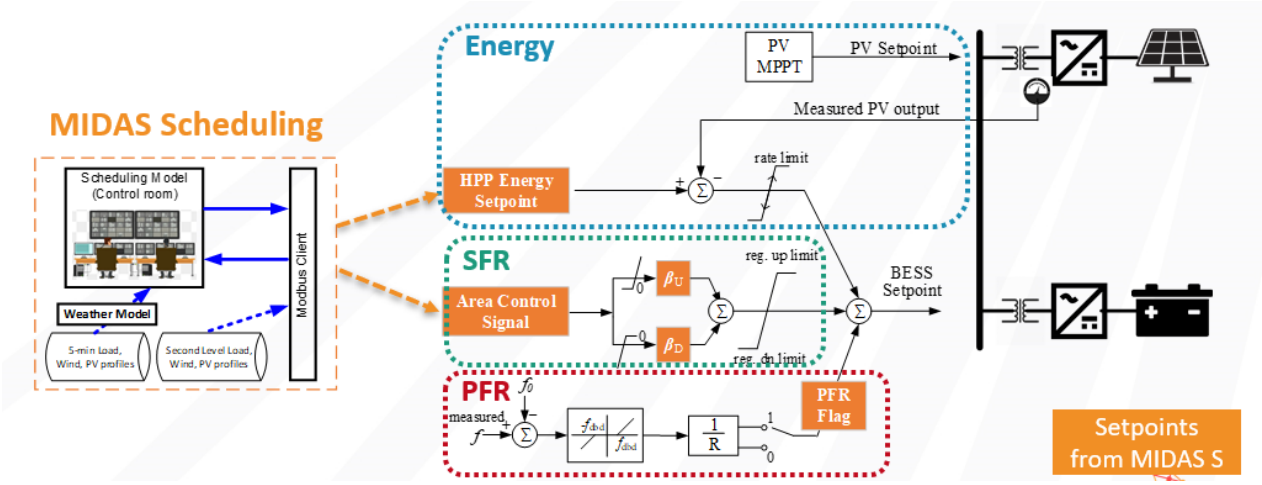

Figure 23. Controllers' implementation for the single hybrid resource mode

The Maui grid model was developed based on a high renewable penetration scenario, which represents a low-inertia condition. A high wind and high PV noon hour with high load (175 MW) is chosen to perform the simulation. In this case, the PV and wind penetration level reached 73%. The renewable profiles of the wind and PV are shown in Figure 24. These PV profiles represent the Maui grid condition on March 7, 2019. The PV variability is high during this hour, as can be observed.

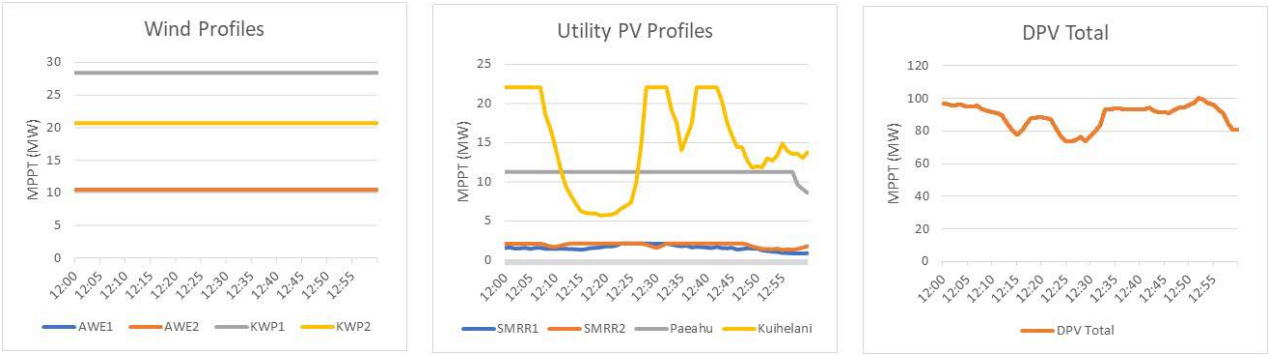

(a) Wind profiles (b) Utility PV profiles (c) Profile of total DPV output

Figure 24. PV and wind profiles of the simulated hour

(2) Simulation Results

In Case 1, the PV is treated as a dispatch resource and provides the frequency-related services. In Figure 25(a), the orange line shows the MPPT of the PV inverter in the field-testing, the blue line presents the set point sent to the PV inverter from MIDAS, and the green line shows the actual output of the PV inverter. AS shown, the PV can be dispatched below the maximum power point (MPP) to provide headroom in this case. Due

to the frequency variation caused by other solar variations, the tested PV inverter can provide both up- and down-regulation services. When the set point aligns with the MPPT, the PV inverter can only provide down-regulation.

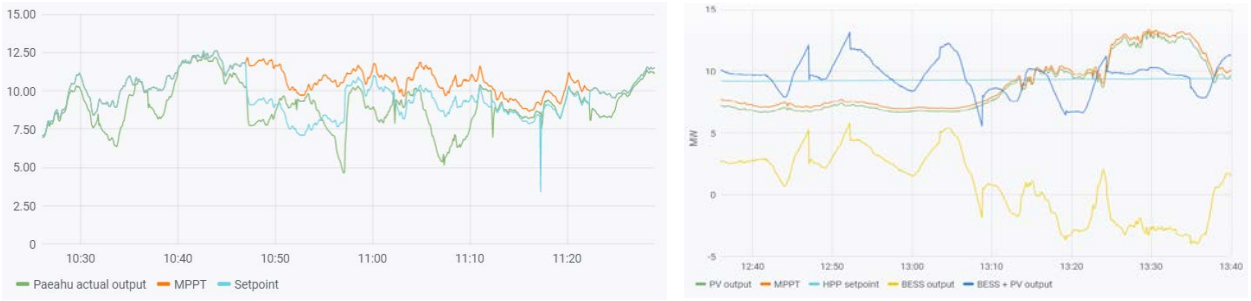

(a) Case1 **(b) Case 2**

Figure 25. PV output under two modes

In Case 2, the set point is sent to the whole HPP. Results show that the PV output can track the MPPT at any time. The dark blue curve is the output of the BESS plus PV. When the PV is in oversupply, the battery can charge itself, and when the PV output is lower than the set point, the BESS can generate power to compensate the PV by discharging. Meanwhile, the BESS also provides up- and down-regulation for ancillary services.

The grid frequency was compared under two cases. As shown in Figure 26, the frequency varied around 60 Hz due to the load and solar variations. To quantify the impact, we calculated the frequency standard deviations and summarize them in Table 6. This shows that the improvement of the grid frequency of the two cases is very close, whether we

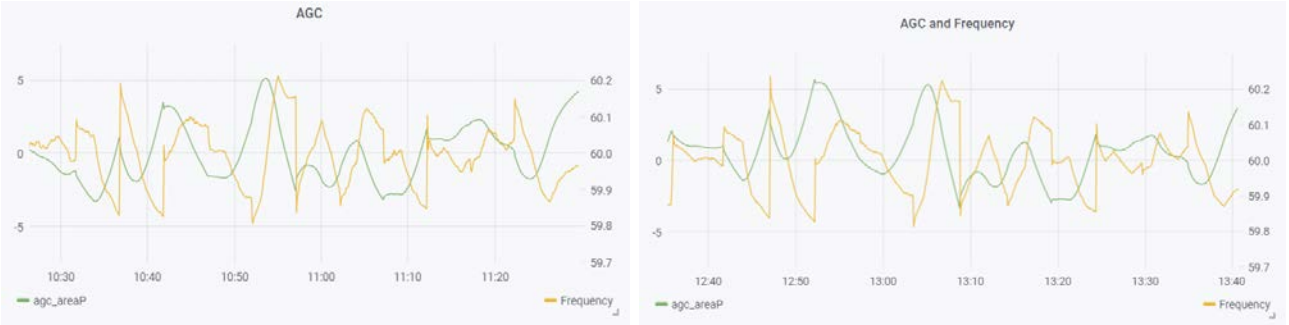

adopt the separate mode or the hybrid mode.

(a) Case 1 **(b) Case 2**

Figure 26. AGC signal and system frequency

Meanwhile, we also compare two cases with a base case that leverages only the PV and battery to provide energy. The renewable curtailment and generation cost are also summarized in Table 6. Compared with the energy-only case, both cases 1 and 2 can reduce the renewable curtailment and generation cost and can improve the reliability metrics (frequency standard deviation). This means that using the HPP (PV+BESS) to provide ancillary services for the Maui grid—renewable-dominated grid—can improve

both system economics and reliability. This is because the Maui grid has an oversupply from solar at noon. Using the curtailed PV to provide ancillary services could avoid the reserve cost that is associated with synchronous generators.

Comparing Case 1 to Case 2, the differences in curtailment and generation cost are mainly caused by the discharge/charge schedule of the BESS. Case 1 can optimize the operation of the PV and BESS from the system level. This means that the operator has full controllability to schedule the BESS in the DAUC and to optimally predefine its charging and discharging. In this study, during the noon hour, the BESS is charging at 5 MW throughout because the DAUC sees abundant renewable generation. In Case 2, however, the BESS is not explicitly modeled because it is now a part of the HPP. Scheduling will not optimize its charge or discharge in a longer horizon because it loses the visibility of the BESS. The BESS is discharging at the beginning and switches to charging in the middle of the simulation. This effectively reduces the net load during this hour, which, in turn, reduces the generation cost but increases the renewable curtailment.

Table 6. Comparison of Three Cases

	Energy Only	Separate (Case1)	Hybrid (Case 2)
Renewable energy curtailment (MWh)	29.81	**22.41**	26.44**
Generation cost ($)	9210.51	8015.82	**7960.77***
Frequency Std	0.092538	0.084765	**0.084601**

(3) Summary

Two HPP operation modes, separate individual resources (Separate) and single hybrid resources (Hybrid), are explored in the PHIL test.

a) The Separate mode requires the system operators to fully model and telemeter both the PV and the BESS devices. This brings additional complexity to the system-level schedule; however, the system operator will have full control of both devices and can potentially achieve a global optimal schedule (e.g., reduced renewable dispatch in our case study).
b) The Hybrid mode needs only the system operators to model and telemeter the hybrid plant as one plant that is comparable to a traditional plant (without the need for forecasting the PV output and real-time monitoring of the PV headroom). The plant owner/operator takes responsibility to coordinate the PV and BESS.
c) Both modes can effectively provide ancillary services (SFR and PFR), as demonstrated in our study.

3.4.2.3 Inertia Requirement Study

To maintain the frequency nadir above 59.3 Hz and the rate of change of frequency (ROCOF) below 3 Hz/s for the Maui grid, we explored nadir constraints and ROCOF

constraints in the scheduling model and studied their impacts. Take the nadir constraints as an example in the following.

To fully capture the relationship among the frequency nadir, the system inertia, the maximum generation outage, and the PFR headroom, a linear regression-based nadir constraint will be constructed and added to the MIDAS generation scheduling model. To build the relationship between the frequency nadir and other system parameters—such as the system inertia, the maximum generation outage, and the PFR headroom—we use 1-year generation scheduling and dynamic simulation data to train this linear regression model. The unit commitment is performed for 1 year (365 days with 8,760 hours). Then, the dynamic simulation of the largest generation outage at that hour is performed for each hour to obtain the system frequency nadir under each hour's largest generation outage.

With these data, the following linear model is constructed:

$$f_{nadir} = a * Inertia + b * PFR_{headroom} + c * Pgmax + d \quad (2)$$

The parameters from the linear regression model are listed in Table 7.

Table 7. Coefficient Results of the Linear Regression Model

	Coefficients
Inertia (a)	0.000847
HR Total (b)	0.006293
Largest Pgen (c)	-0.04737
Intercept (d)	59.86421

The frequency nadir linear regression results are shown in Figure 27.

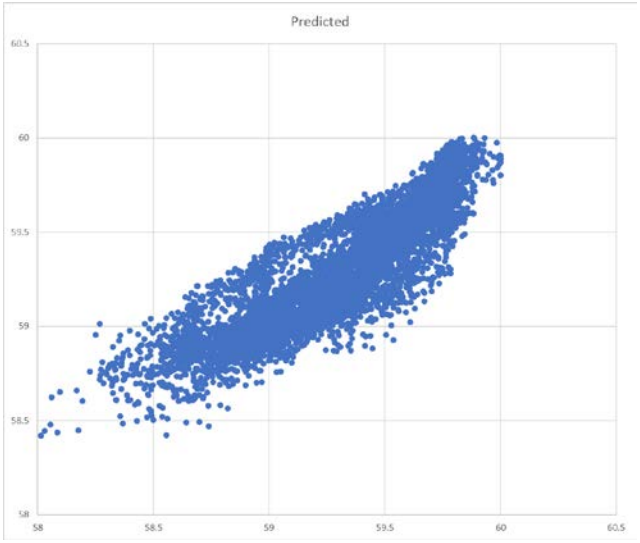

Figure 27. System frequency nadir from the linear regression forecast and dynamic simulation

The forecasting errors of the nadir using the linear regression model are depicted in Figure 28. The R2 error is 0.79, and the standard deviation is 0.1692 Hz. Ninety percent of the cases have a prediction error between [-0.29, 0.29] Hz.

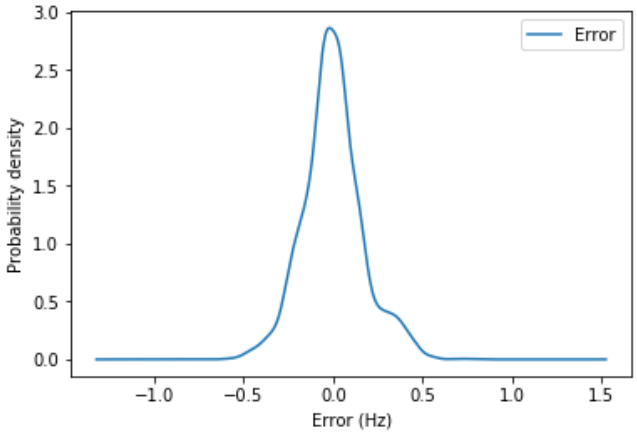

Figure 28. System frequency nadir forecasting error distribution

Three cases are simulated, including the case without nadir constraints, the case with nadir constraints, and the case with only inertia constraints.

Case 1: without inertia constraints

Case 2: with inertia constraints based on the linear regression model with (2) added

Case 3: with a predetermined inertia constraint (Inertia > 350 MVA*s).

The generation scheduling results of these three cases are listed in Table 8.

Table 8. Scheduling Results with Nadir Constraints

	Generation Cost ($)	*Min Nadir (Linear Regression)*
No constraint	244481.3	58.70977
Linear regression constraint (Eq. (2))	259055.2	59.29053
Inertia >350 MVA*s	311722.5	58.89598

As shown in Table 8, the system generation cost increases when the nadir and inertia constraints are added. With the inflexible inertia constraints, the generation cost significantly increases. With the adaptive linear regression-based nadir constraints, the generation cost mildly increases.

The system frequency nadirs in the three cases are simulated and shown in Figure 29.

As shown in Figure 29 with the linear regression constraint, the frequency nadir, will be

larger than 59.3 Hz for most hours. Only 2 hours nadir is slightly lower than 59.3 Hz. Because the linear regression model has some forecasting errors, at these hours, the nadir is slightly lower than the predetermined 59.3 Hz. With only the inertia constraints, the frequency nadir cannot be maintained.

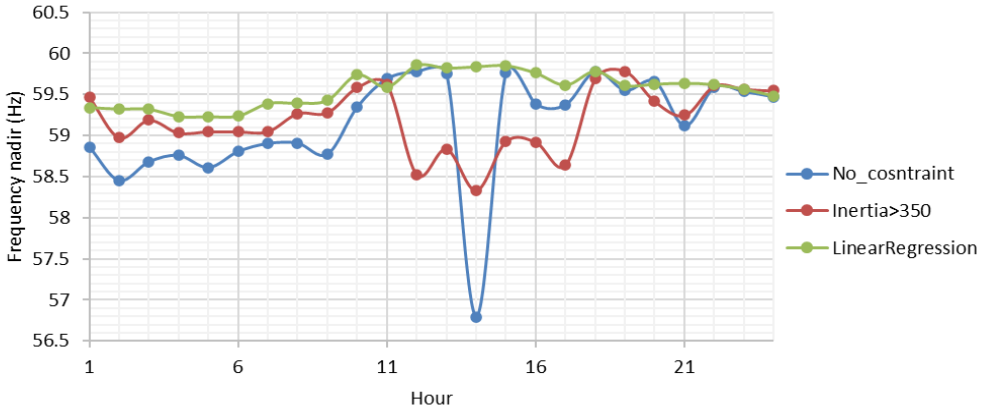

Figure 29. System frequency nadir from dynamic simulations

In this project, both the impacts of the inertia and the ROCOF-related constraints are studied in the scheduling model. A linear regression model is used to construct the constraint of the inertia, the PFR headroom, the largest generation contingency, and the frequency nadir. The simulation results show that the generation cost increases after adding this constraint. The system frequency nadir for most hours can be improved with this nadir constraint. Compared to a case with predetermined inertia constraints, the cost of the linear regression-based nadir constrained case is lower. In addition, the nadir results of the inertia-constrained case demonstrate that the system cannot maintain the nadir by considering only the inertia.

3.5 Large-Scale EMT Model for Maui Grid

3.5.1 EMT Modeling of Maui Grid

The Maui transmission system has been constructed in the Power Systems Computer Aided Design (PSCAD) software platform using parallel computational elements from both PSCAD and the E-RTAN Plus from Electranix Corporation to operate on 30 cores, which reduces the computational cost by more than an order of magnitude. A 20-second simulation takes approximately 4 hours of computation time in this 30-core configuration. Figure 30 shows the layout of the model, with substantial bus reduction for descriptive purposes and to protect proprietary information. The model, as dispatched in the 2023 case, includes 171 distributed solar PV units, 90 loads, 2 Type 3 and Type 4 wind power plants, 2 utility-scale solar plants, 3 hybrid power plants, 3 synchronous generators, and 6 synchronous condensers.

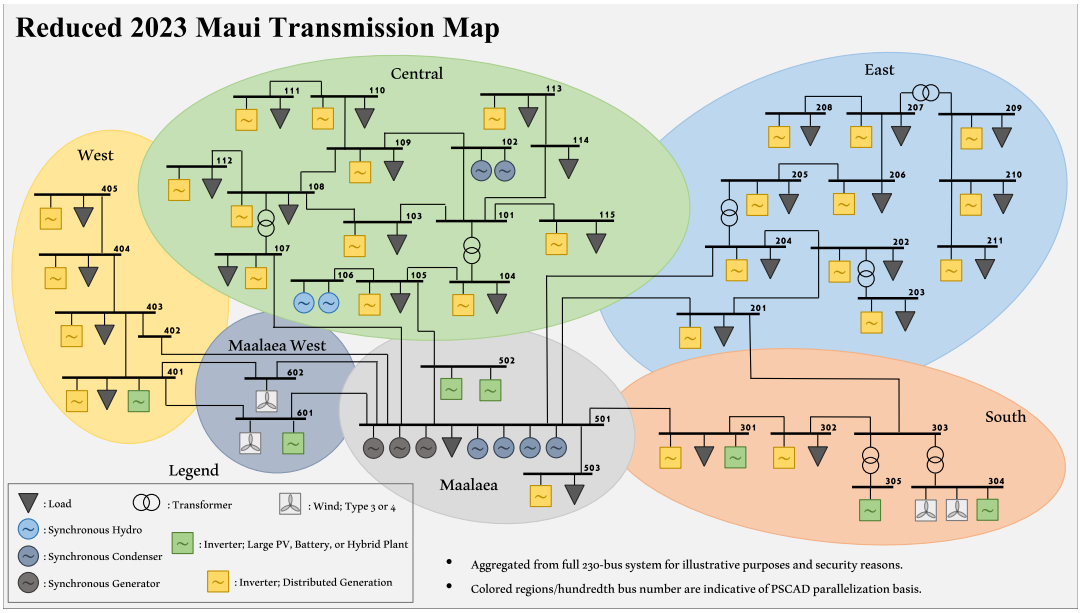

Figure 30. PSCAD Maui transmission map

3.5.2 Validation of Maui PSCAD Model

The alignment of the PSCAD model with the Hawaiian Electric Companies-supplied PSS/E model required the comparison of steady-state voltage magnitude and bus phase quantities. The distribution of errors between the two models is shown in Figure 31, which are minimal and deemed acceptable.

The distributed PV (DPV), utility-scale solar, and HPP plants are all implemented in PSCAD using high-order grid-following (GFL) models (Figure 32 (a)) developed by the NREL team. In tandem, grid-forming (GFM) models (Figure 32 (b)) were also developed. These models, established in the DQ rotating reference frame, include 6th-order output filters, inner current controllers, and respective power (GFL) or voltage (GFM) controllers. The publication [34] documents these models.

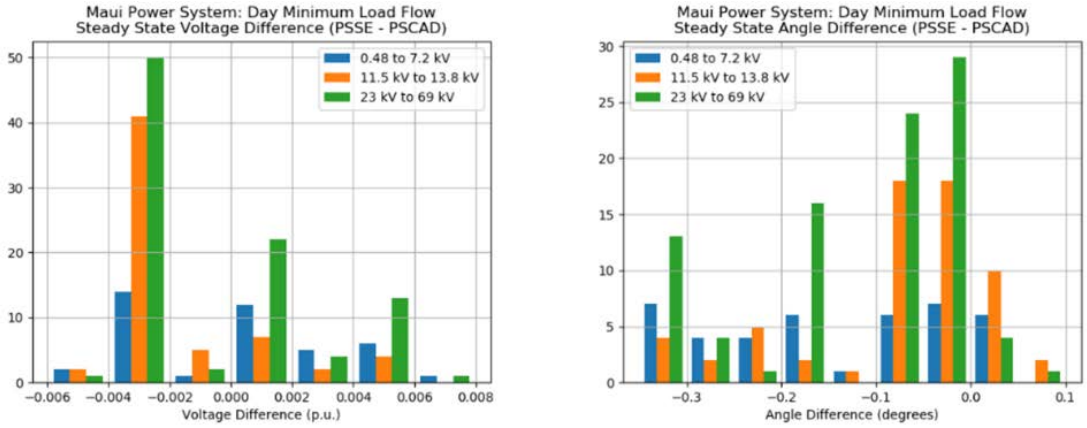

Figure 31. Count (histogram) of buses with various levels of error in (a) steady-state voltage and (b) phase angle between the PSS/E and PSCAD models

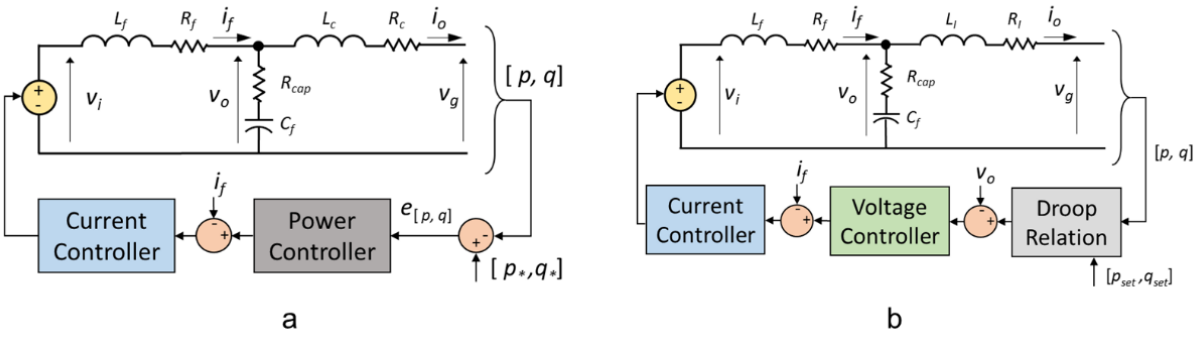

Figure 32. (a) GFL and (b) GFM control diagrams for PSCAD implementation

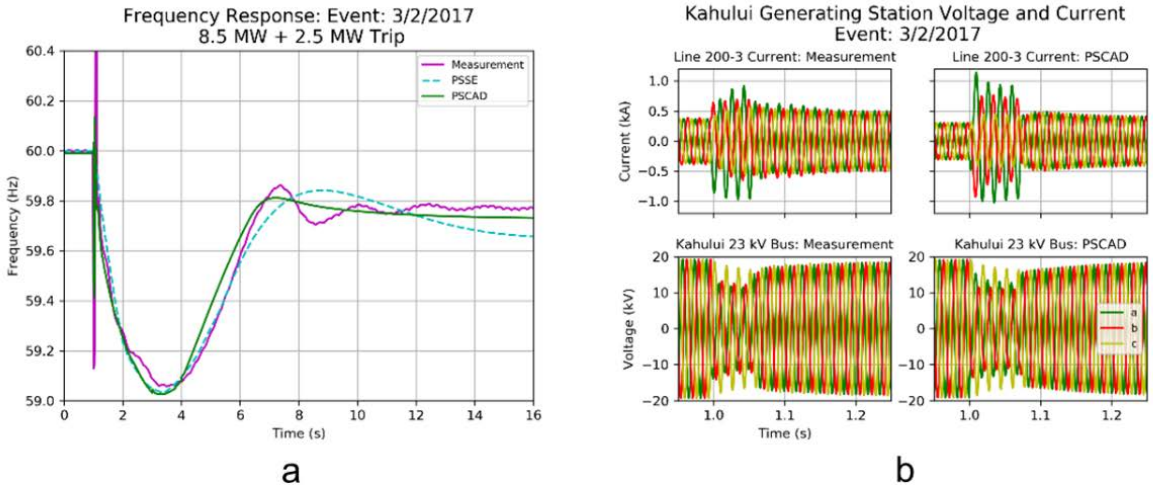

Figure 33. (a) Frequency and (b) current and voltage waveforms of the measured and PSCAD reproduced response for the March 2, 2017 event

An event on March 2, 2017, which consisted of a fault on a synchronous generator's transformer and subsequent trip of that generator, was selected for the dynamical validation of the PSCAD model. The measured frequency response, the PSS/E generated response, and the PSCAD generated response are shown in Figure 33(a). The measured and PSCAD generated current and voltage waveforms of the selected buses are shown in Figure 33(b). The field data show a damped oscillation around 0.4 Hz that does not appear in either the PSS/E or PSCAD model. After investigation, it was found that not enough data existed to determine the cause of the 0.4-Hz oscillation. In addition, the oscillation was not present in more recent field events and was not of major concern to the utility partner, so the team decided to move on. The effort to validate the Maui PSCAD model is documented in [35].

3.5.3 Simulation of Low-inertia Scenarios

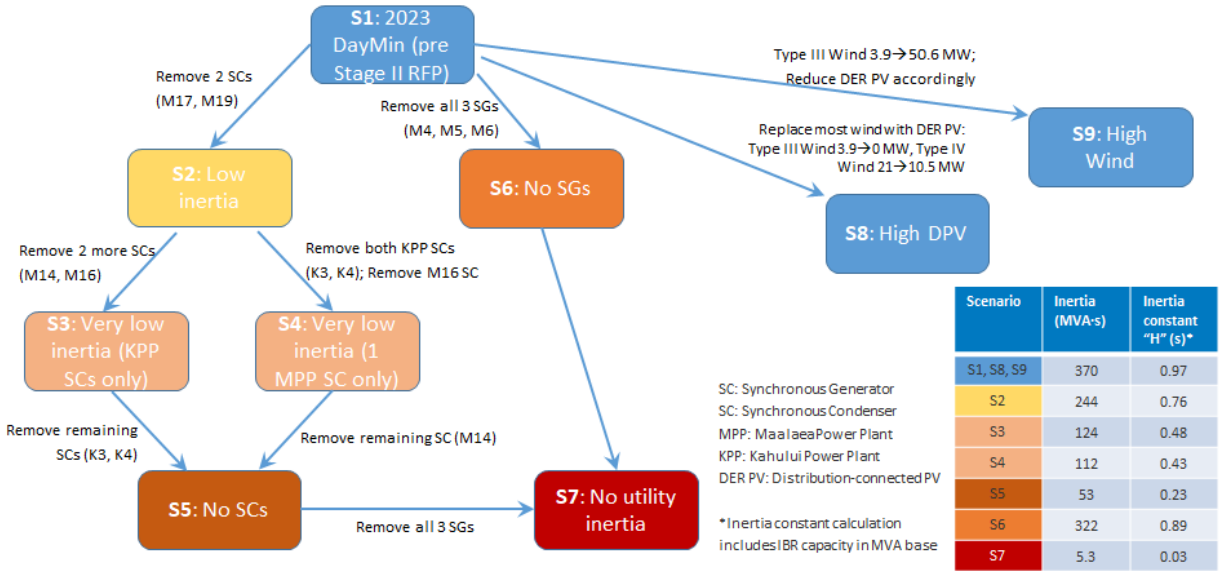

Scenario	Inertia (MVA·s)	Inertia constant "H" (s)*
S1, S8, S9	370	0.97
S2	244	0.76
S3	124	0.48
S4	112	0.43
S5	53	0.23
S6	322	0.89
S7	5.3	0.03

Figure 34. Maui PSCAD simulation scenarios

With the validated PSCAD model of the Maui system in the 2023 day minimum load dispatch, denoted as scenario S1, eight more scenarios were dispatched, as shown in Figure 34. Scenarios S2–S5 represent a consecutive decrease in system inertia. Scenario S6 has only synchronous condensers online. Scenario S7 has zero utility-side inertia. Scenarios 8 and S9 are high wind and high DPV, respectively. Note that the utility's planning cases have since changed from those analyzed here; in addition, scenarios S2–S7 were extrapolations from a planning case to lower inertia scenarios and do not necessarily represent planned operating scenarios.

Eleven events were simulated in PSCAD for each scenario, as shown in **Table 9**. The events E1–E7 represent faults on critical buses (low short-circuit or low critical clearing time), E8 is the loss of 21 MW of wind power, E9 is the trip of a critical transmission path,

E10 is the loss of four behind-the-meter hydro units, and E11 is the loss of a synchronous condenser.

For these simulations, discontinuous control behaviors, such as distributed energy resource (DER) tripping and underfrequency load-shedding action, were disabled to better observe the system oscillatory stability.

Table 9. Maui PSCAD Events Simulated

Event	Contingency	Notes
E1	A three-phase fault on bus 97 (KWP) and cleared in 5 cycles.	Fault at a low short-circuit ratio (SCR) bus
E2	A three-phase fault on bus 1203 (AWP) and cleared in 5 cycles.	Fault at a low SCR bus
E3	A three-phase fault on bus 35 (Kihei) and cleared in 5 cycles.	Fault at a low critical-clearing-time (CCT) bus
E4	A three-phase fault on bus 39 (Maalaea) and cleared in 5 cycles.	Fault at a low CCT bus
E5	A three-phase fault on bus 401 (Puunene) and cleared in 5 cycles.	Fault at a low CCT bus
E6	A three-phase fault on bus 823 (Puuk B) and cleared in 5 cycles.	Fault at a low CCT bus
E7	A three-phase fault on bus 850 (Mahina A) and cleared in 5 cycles.	Fault at a low CCT bus
E8	Loss of the largest generator (21 MW wind plant)	
E9	Loss of line 39-35 (Maalaea-Kihei)	A critical contingency for Maui system which may lead to voltage instability
E10	Loss of 4 BTM hydro units	Reduces inertia (to zero in S7)
E11	Loss of synchronous condenser (SC)	K4 is lost upon fault in S3; M14 is lost for all other scenarios except for S5 and S7 where there is no SC

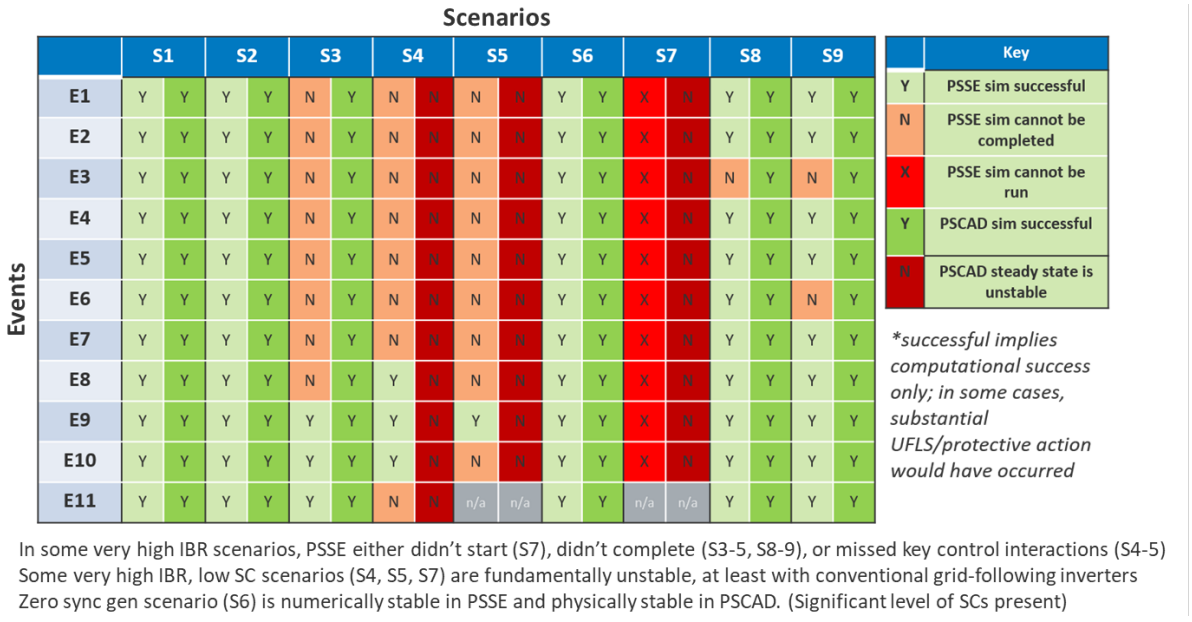

Figure 35. Simulation results for PSS/E and PSCAD for varied dispatch scenarios and events

Each of the 11 events were simulated in PSCAD for each of the 9 scenarios. Figure 35 shows the summary of the results of each simulation with GFL inverters. These results show that the Maui model with no GFM assets (S7) is not stable, as expected.

Interestingly, the model with only synchronous condensers as GFM (S6), and all frequency response from HPPs, is stable, as detailed in [36]. The scenarios become less stable as the inertia decreases, as illustrated in subsequent figures, with scenarios S3 and S4 being borderline unstable and scenarios S5 and S7 being unstable. Scenarios S1, S8, and S9 gave similar results, indicating that the exact mix of GFL assets did not strongly influence the stability for these scenarios. A journal paper highlighting these results is under construction [40]. Selected simulation cases are discussed in the following.

Event 1: Fault at Low Short-Circuit Ratio Bus (97, KWP I)

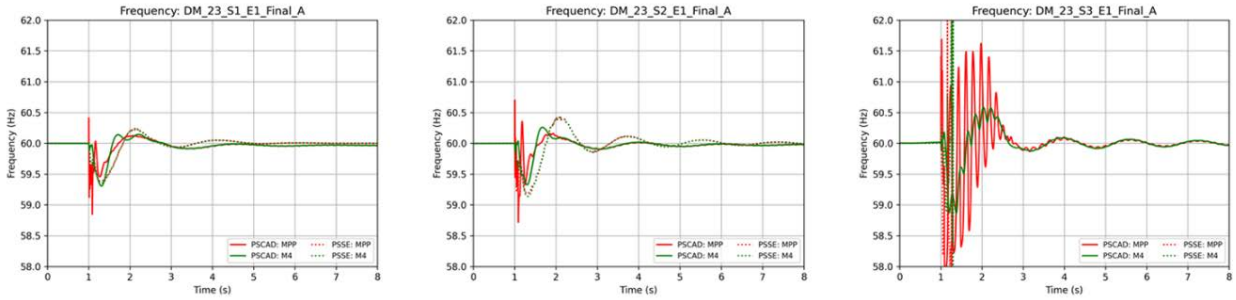

Figure 36. PSS/E and PSCAD frequency (shaft speed and phase-locked loop derived) for event E1 applied to scenarios (a) S1, (b) S2, and (c) S3, which have successively decreasing inertia levels. (MPP indicates the frequency at the Maalaea Power Plant, and M4 indicates the frequency derived from the rotor speed of generator M4.)

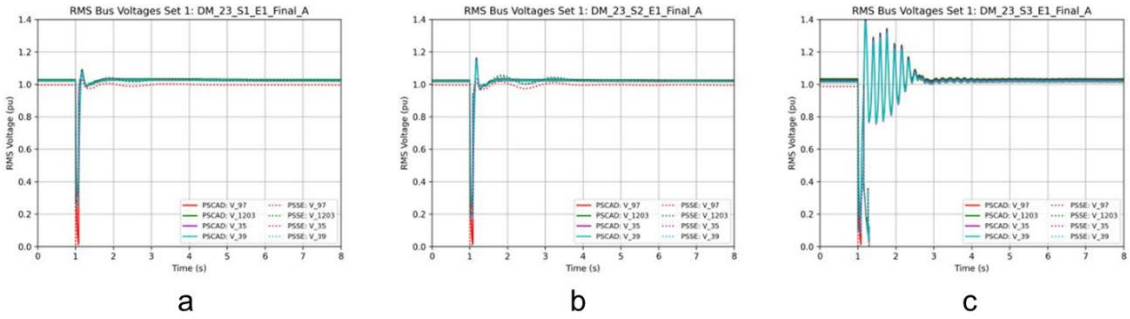

Figure 37. Root-mean-square PSS/E and PSCAD voltages for selected buses. Event E1 is applied to scenarios (a) S1, (b) S2, and (c) S3.

Time domain profiles are provided for frequency (Figure 36), root-mean-square voltage (Figure 37), and aggregate distributed generation output (Figure 39). In Scenario S3, which represents a 66.7% reduction in inertia (or GFM assets on the system) from S1, the system has a poorly damped, high-frequency mode that appears only on PSCAD. The PSS/E model fails (is numerically unstable) in this simulation.

	S1	S2	S3	S4	S5
Low freq mode	0.44 Hz	0.50 Hz	0.64 Hz	0.65 Hz	1.77 Hz
Damping ratio	25.4%	16.0%	5.03%	-0.46%	-1.55%
Inertia (MVA·s)	365	239	119	108	48

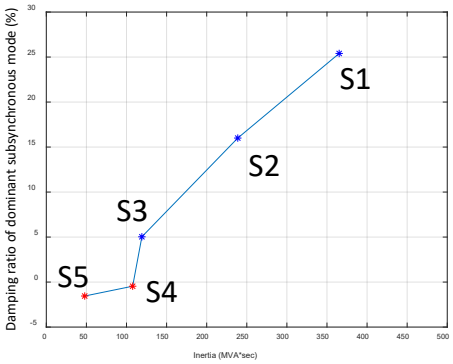

Figure 38. Effect of reducing system inertia on oscillatory stability for event E1

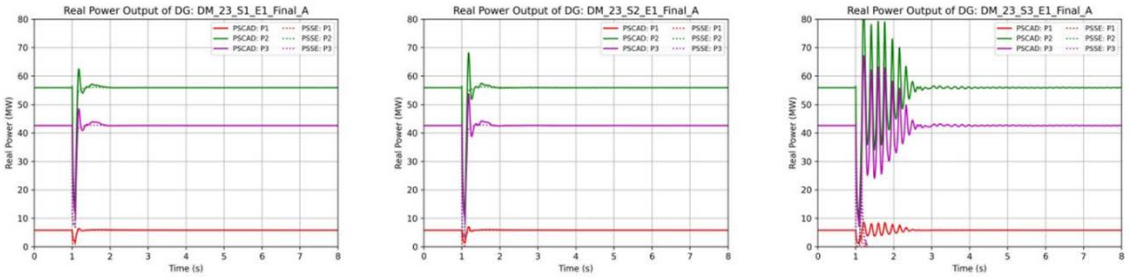

Figure 39. Aggregated distributed generation output for PSS/E and PSCAD. Event E1 is applied to scenarios (a) S1, (b) S2, and (c) S3

The effect of reduced inertia on system stability (as quantified by the damping ratio) is illustrated in Figure 38. Also note that the location of the inertia on the system can play a role: Scenarios S3 and S4 have similar inertia but different damping ratios.

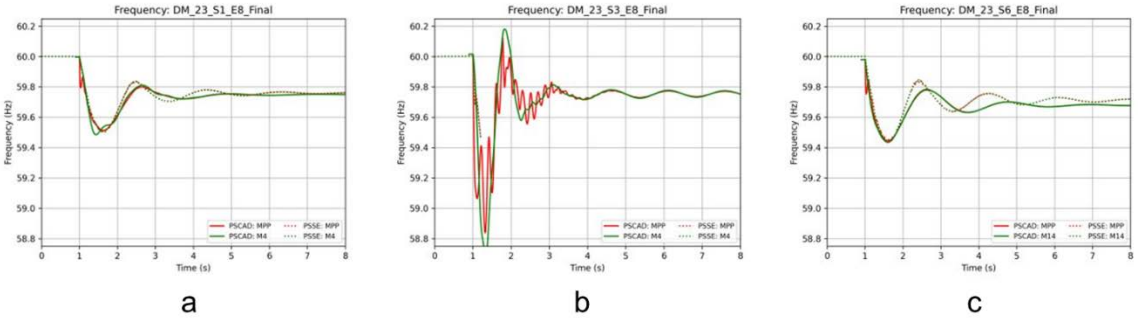

Figure 40. Frequency response for scenarios (a) S1, (b) S3, and (c) S6, perturbed with event E8

Figure 40 illustrates that the dynamic response of scenario S6 is very similar to S1 despite having zero synchronous generation (but significant quantities of synchronous condensers) online; however, note that these simulations do not include DER trip and momentary cessation dynamics. If DER momentary cessation dynamics are included, the

synchronous condensers might not be sufficient to stabilize the system under severe fault events due to the need to replace lost DER active power.

Event 8: Loss of Largest Generator (21 MW from Wind Plant)

The time domain frequency results of Event 8 as applied to S1, S3, and S6 are shown in Figure 40 (a), (b), and (c), respectively.

GFM Inverter Impacts

As a display of the potential benefits to GFM controls, a single HPP unit is replaced with a droop-controlled GFM inverter and compared to the scenario S3 response to event E8. The frequency response in Figure 41 shows a substantial improvement in response, with a much higher nadir and improved damping with the GFM (b). The active power output of the GFM device, called G2 in Figure 42(b), shows a near-instantaneous delivery of power following the perturbation.

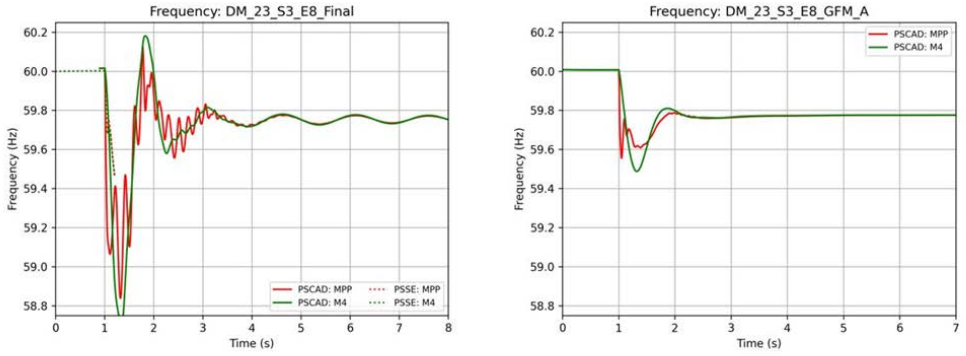

Figure 41. Frequency response to event E8 applied to scenario S3 with (a) all GFL and (b) a single HPP as GFM

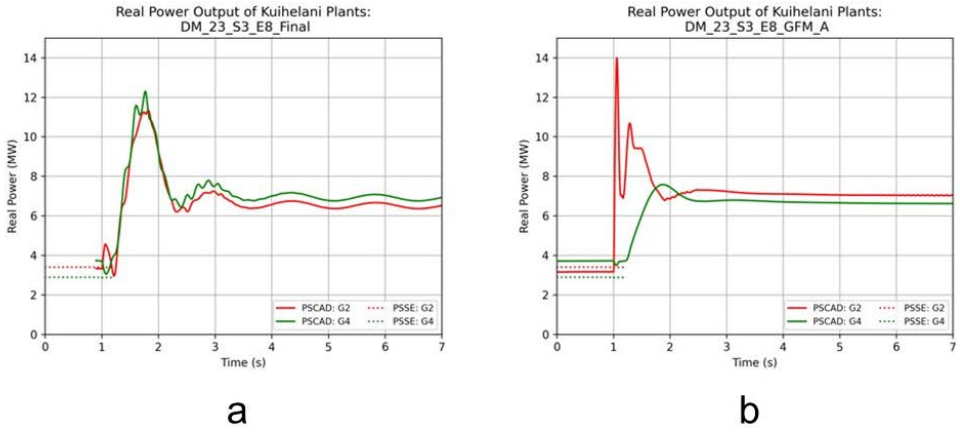

Figure 42. HPP real power response to event E8 applied to scenario S3 (a) without GFM and (b) with a single plant as GFM. G2 is a 30-MVA PV-BESS plant that is in GFL mode in (a) and GFM mode in (b). G4 is another 30-MVA PV-BESS plant that is in GFL mode in both simulations.

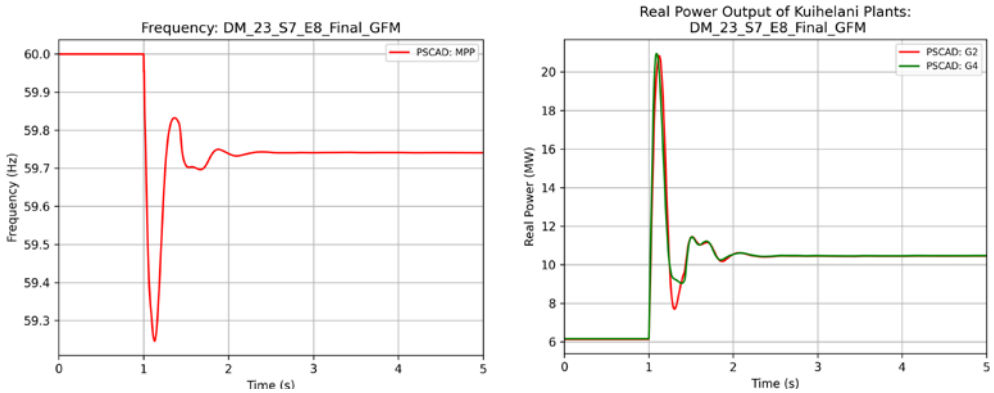

Figure 43. (a) Frequency and (b) real power response of GFM resources to Event E8 applied to scenario S7, which contains only IBRs (no synchronous machines)

The EMT simulations also indicated that it is possible to stabilize the zero-inertia scenario, S7, of this 145-MW power system with 60 MVA of GFM capacity. Figure 43 shows the response to event E8 (loss of the largest generator): The system is stable and recovers quickly. In contrast, without GFM capacity, this event is unstable, even before perturbation. These results will be further detailed in an upcoming publication.

An investigation into the impacts of controller complexity yields that the modeling of the inverters' inner current loops is critical to uncover the high-frequency oscillatory modes, as indicated by Figure 44. This work was presented at the Power Systems Computation Conference in June 2022 [37]. Based on this result, the team now includes in all EMT simulations the phase-locked loop, current controller, and power controller dynamics of IBRs. (Prior to this, and to some extent still in industry and academia, it is common for dynamic simulations to include only power control loops.)

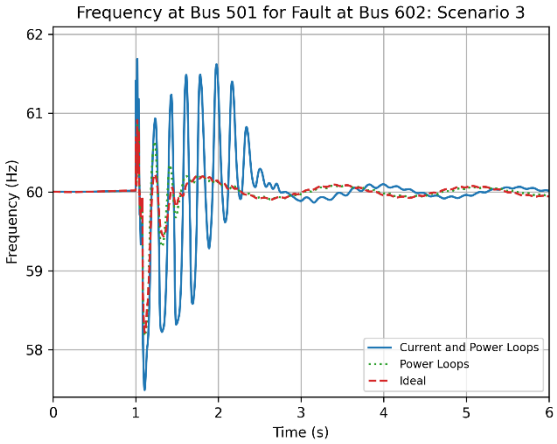

Figure 44. Frequency results for varied GFL inverter controller complexity

3.5.4 Transmission and Distribution Simulation of Maui Grid

A single-phase GFL inverter has been developed in the PSCAD environment and applied to an aggregate feeder model that replaced a constant power load and three distributed generation units. The feeder model is shown in Figure 45, in which short circuit ratios of the feeder buses are also included. The time-domain responses do not differ substantially from the non-feeder models and thus not repeated here. However, for certain simulations such as unbalanced faults (not simulated here), including single-phase DER representations would be very important (though it is rarely done in practice).

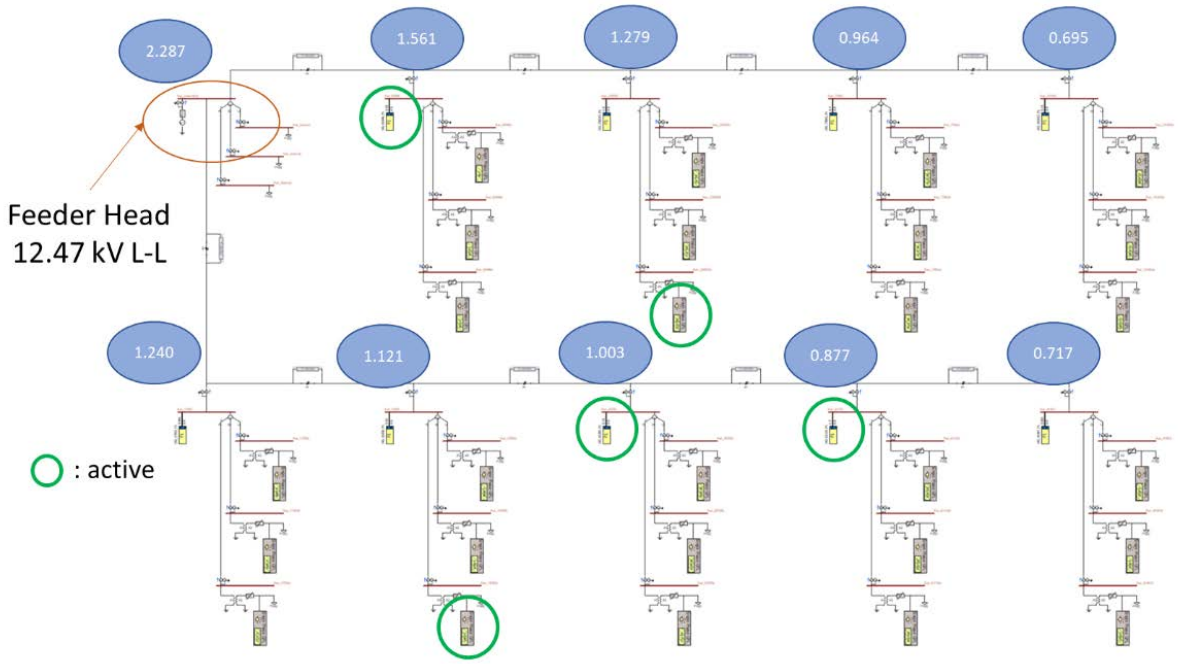

Figure 45. Feeder model showing the location of single phase, and three phase inverter models

3.6 PHIL Testing for MIDAS

3.6.1 MIDAS PHIL Test Bed

3.6.1.1 Framework

MIDAS PHIL test bed has been set up using software/hardware facilities at NREL's Flatirons campus, including MIDAS server, RTDS machine, and Controllable Grid Interface. Maui grid is simulated on RTDS, which takes the real-time power set points from MIDAS server and simultaneously interacts with power hardware.

3.6.1.2 RSCAD Model (version 1) Development for Maui Grid

Maui RSCAD model version 1 was developed from the Day Minimum case provided by Hawaiian Electric by first conducting a network reduction using our proposed reduction techniques [43] to enable the simulation with 4 NovaCor cores on RTDS, and then adding

hybrid power plant (HPP) models whose controls are to be evaluated.

- Reduced model in PSS/E has been validated over a loss-of-generation event, where frequency deviation curves overlap with each other between the models before and after the network reduction. Steady state of the Maui RSCAD model has also been validated by comparing the bus voltage, MW, and MVar of generation and load to those in reduced PSS/E model. Dynamics have been validated over the loss of one generation unit.
- AGC has been implemented in this RSCAD model. All generations, loads, and their frequency droop characteristics have been properly configured. Through these efforts, we can get reasonable frequency responses.
- Communication between MIDAS server-RTDS (121 channels) and that between RTDS-hardware (5 channels) have been implemented by Modbus and UDP, respectively.

3.6.1.3 Use Cases

Three different PV/HPP control strategies are simulated for the Paeahu HPP.

Case 1. PV and BESS only provide energy: PV only provides energy and can be curtailed through delta control. BESS strictly follows a constant charging/discharging profile determined day ahead.

Case 2. PV provides both energy and ancillary services: PV provides energy and ancillary service (PFR and AGC) through delta control. BESS strictly follows a constant charging/discharging profile determined day ahead. This case verifies that PV inverters can be used to provide both regulation and PFR services.

Case 3. HPP (PV+BESS) provides both energy and ancillary services: PV and BESS are treated together as a single plant and receives a single set point. HPP provides both PFR and AGC. This case verifies that by forming an HPP, PV and BESS can provide both regulation and PFR services. The detailed discussion and analysis haven been included in Section 3.4.2.2.

Table 10. Reliability and Economic Comparison of Three Cases

	Case 1	Case 2	Case 3
RE Curtailment (MWh)	29.81	**22.41**	26.44
Generation Cost($)	9211	8016	**7961**
Frequency std	0.0925	0.0848	**0.0846**

3.6.2 PHIL Testing for GFM Inverter in Low-inertia Grid

EMT simulations described in Section 3.5 demonstrate the ability of grid forming inverters to stabilize Maui system dispatches that are otherwise unstable, include cases with 100% inverter-based generation, both with and without synchronous condensers. These PSCAD simulations have used NREL's generic PSCAD models of GFM inverters. To gain more confidence in these findings using a real hardware inverter, we developed a real

time, EMT-domain model of the Maui power system in RSCAD and used PHIL to test the ability of a real megawatt-scale inverter at NREL's Flatirons Campus to stabilize the Maui system. The 2.2-MW SMA inverter can operate in GFM and GFL modes, allowing an apples-to-apples comparison of Maui system stability with the inverter in GFL and GFM modes.

3.6.2.1 Maui RSCAD model (version 2) for EMT-domain PHIL

In Section 3.6.1, we have developed the Maui RSCAD model (version 1) which focuses on frequency dynamics and their interactions with scheduling. Following that work, we added faster dynamic models for several key components in the system including the DPV units and 3 HPP units. This version 2 is designed for capturing fast EMT-domain dynamics of the Maui system in cases at nearly 100% IBRs. Major changes from version 1 to version 2 are summarized in **Table 11**.

3.6.2.2 PHIL Testbed Set up

The PHIL test setup as implemented at NREL's Flatirons Campus is shown in Figure 46. We leverage an RTDS real-time computer to run the model and simulate the dynamics of Maui power system. The simulated 3-phase voltage waveforms at the point of interconnection of the 30 MVA PV-BESS plant (called K1 below) are transmitted in real-time to a 7 MVA controllable grid interface (CGI, a controllable AC supply). The AC terminals of the 2.2-MVA hardware inverter are connected to the CGI so that the inverter sees the voltage waveforms produced by the Maui model. The inverter responds to those voltages as it would to voltages in the real power systems, and its resulting 3-phase output current waveforms are sampled using medium voltage CT's every 25 μs, digitally filtered for noise and anti-aliasing, transmitted to the RTDS via 2 Gb/s optical cables, and injected in real time back into the Maui model, completing the PHIL loop. More details of PHIL setup can be found in publication [41].

Table 11. Major Changes from Maui RSCAD Model Version 1 (V1) to Version 2 (V2)

	Element	Modeling in V1	Modeling in V2
Purpose		• Capture slower dynamics and their interactions with scheduling	• Capture fast EMT-domain dynamics of the Maui system in cases at and near 100% IBRs
Dispatch	Generation and load	• 2022 DayMin No HPP case • Single scenario, no disturbance • Total load = 145.2 MW, total generation = 146.4 MW.	• 2023 DayMin 3 HPP case • 6 scenarios, 2 contingencies, 4 configurations (for 2 HPP units) • Total load = 162 MW, total generation = 164 MW.
Dynamic elements	Machine	• 6 synchronous generators (SGs) w/ exciters and governors, no synchronous condensers (SCs)	• 3 SGs w/ exciters and governors and 6 SCs (the 6 SGs in V1 were either removed or converted into SCs, 3 small SGs and a couple of SCs were added)
	Load	• 13 loads, w/ load-frequency characteristics added	• 11 loads (2 small ones merged into nearby loads)
	DPV & UPV	• 12 DPVs and 2 UPVs (utility-scale PV plants). • Each of DPVs and UPVs is modeled as dynamic PQ source.	• 10 PVs (2 UPVs and 2 small DPVs merged into nearby DPVs) • Detailed average DPV model was implemented (translated from Kenyon's PSCAD DPV model: https://github.com/NREL/PyPSCAD)
	BESS	• Two BESSs, i.e., BESS1 and BESS2 • BESS1 modeled as dynamic PQ source w/ fixed set point (no droop) • BESS2 modeled as dynamic PQ source w/ frequency droop.	• The control in BESS1 PSS/E model documentation has been implemented in RSCAD, which, upon a frequency drop <59.7Hz, injects extra MW for 5 sec and then linearly ramps back to the pre-disturbance output level in the following 30 sec. • BESS2 is still modeled as dynamic PQ source w/ droop (updated gain).
	Wind	• 2 type-3 and 2 type-4 wind farms • Modeled as dynamic PQ source w/ fixed set point (no droop)	• Detailed average WTG models provided by RTDS are ready to be swapped in. However, this requires 1-2 more RTDS cores than the available. Still, wind farms are modeled as dynamic PQ source.
	HPP	• 3 HPPs • W/ frequency droop	• Modeled as detailed IBR model, BESS RSCAD model, or represented via PHIL by BESS inverter hardware, based on different control configurations
Comms	MIDAS-RTDS	• Modbus	• Modbus disabled, no comms with MIDAS server. Switching scenarios manually within RTDS.
	Hardware-RTDS	• UDP	• UDP
AGC		• AGC units include all 6 SGs, 3 HPPs and 2 BESSs w/ controllable participations. AGC signals updated every 4 seconds.	• AGC disabled.

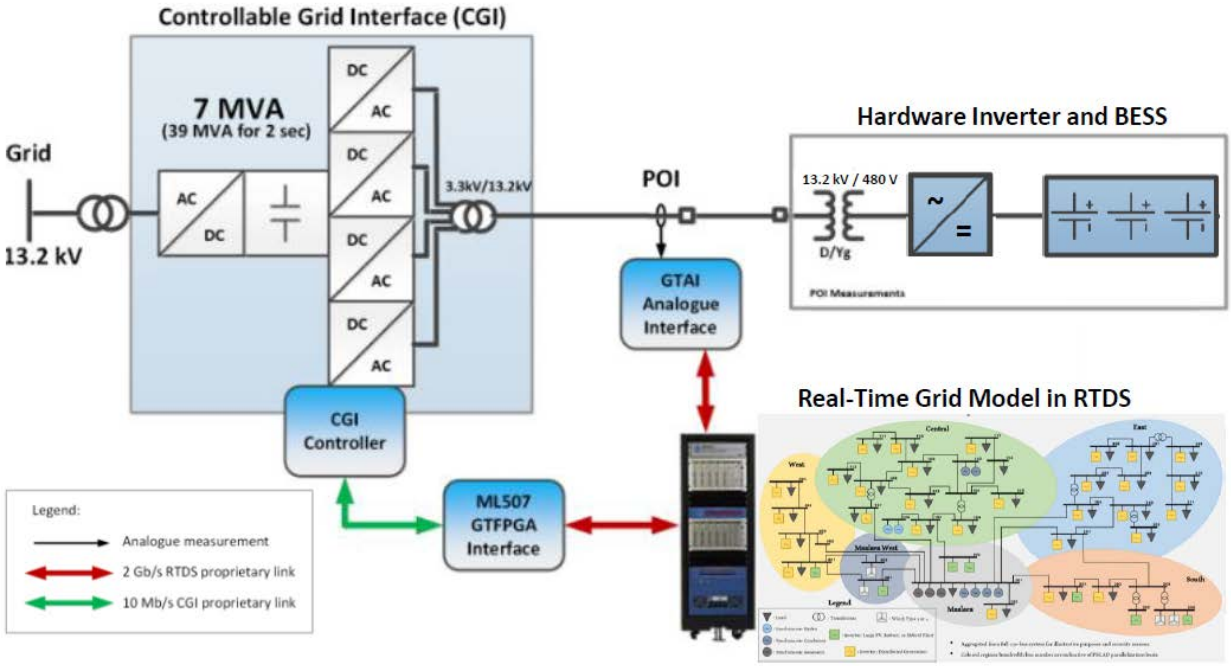

Figure 46. Multi-MW high-fidelity PHIL test setup

3.6.2.3 Simulation Scenarios Power HIL Test Results

Table 12. PHIL Test Scenarios, in Order of Decreasing Inertia

Scenario	# SGs	# SCs	Inertia (MVA·s)	Inertia constant H (s)	Generation from IBRs (%)
S1	3	6	365	0.97	96%
S6	0	6	317	0.89	100%
S2	3	4	239	0.76	96%
S3	3	2	119	0.47	96%
S3a	3	1	92	0.39	96%
S5	3	0	48	0.21	96%
S7	0	0	0	0.0	100%

Seven Maui resource dispatch scenarios were implemented in the RSCAD model. The scenarios are summarized in **Table 12**, where the abbreviations SG and SC stand for synchronous generator and synchronous condenser, respectively.

Simulation assumptions include

- For each scenario, two events were simulated: A 3-phase, 5-cycle fault at a low SCR bus (bus 97) and the loss of largest generator (two adjacent wind plants operating at 21 MW in total).
- For all simulations, underfrequency load-shedding and inverter trip and momentary cessation settings were disabled within the RSCAD model to better observe the system dynamics.

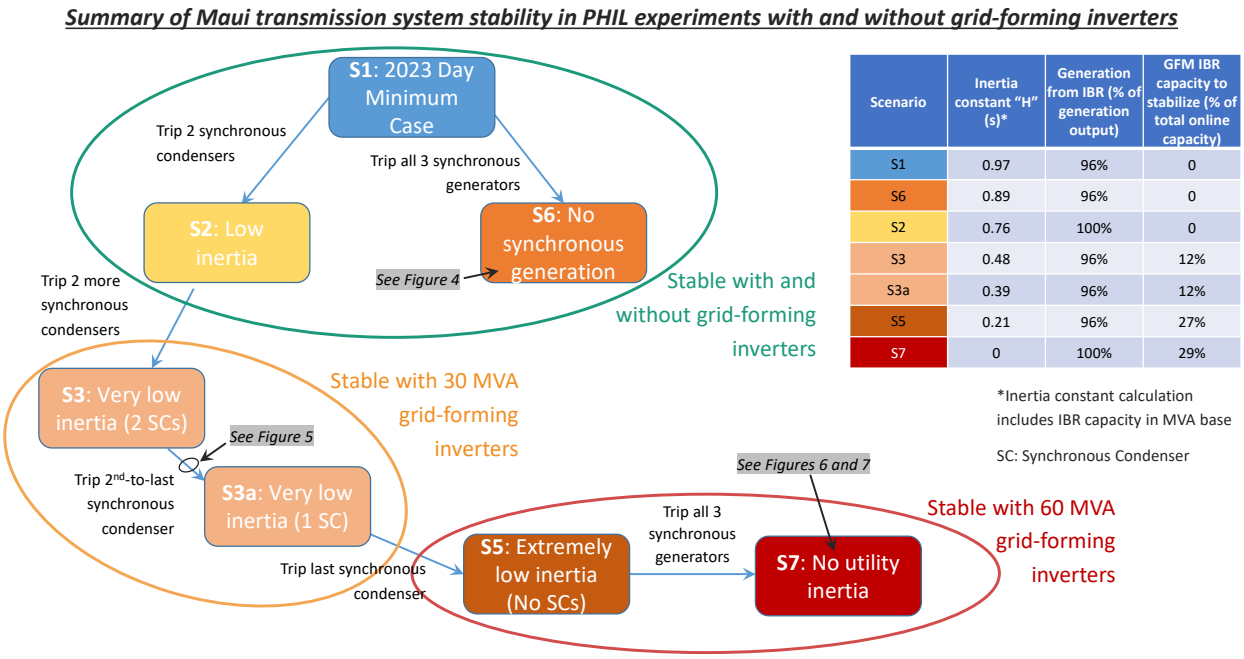

Figure 47. Summary of PHIL test results. To be considered stable, a scenario has to survive both the fault and the N-1 generation trip tests without frequency exceeding underfrequency load-shedding thresholds and without voltage or frequency exceeding ranges that would cause excessive tripping of generation.

The results of the PHIL tests are summarized in Figure 47, and selected test results are presented in detail below. The scenarios with inertia constants above 0.6 seconds were stable in all cases, with and without GFM inverters. Scenarios 3 and 3a, which had inertia constants between 0.3 and 0.5 seconds, needed 30 MVA of GFM capacity (12% of total online generation capacity) to remain stable. The very low inertia scenarios are stabilized with 60 MVA of GFM inverter capacity (27% to 29% of total generation online capacity). Notably, the percentage of generation from IBRs is not predictive of stability or of the need for GFM capacity to provide stability. In contrast, low inertia is clearly associated with higher need for GFM capacity. These results align with PSCAD tests in this report.

One example with fault event of a zero-inertia operating case is shown in Figure 48, other case studies can be found in publication [41]. It shows that for the 60 MVA GFM case (purple), the system recovers quickly from the fault without oscillations. For the case with 30 MVA of GFM in hardware (blue), the simulation shows low-amplitude oscillations even before the event, and the inverter trips shortly after the fault, causing the system voltage

to collapse and the PHIL system to trip. With 30 MVA of GFM in simulation (red), the system voltage and frequency oscillate after the fault and eventually stabilize; however, the large voltage and frequency deviations would likely have resulted in extensive tripping of DPV and possibly a system collapse.

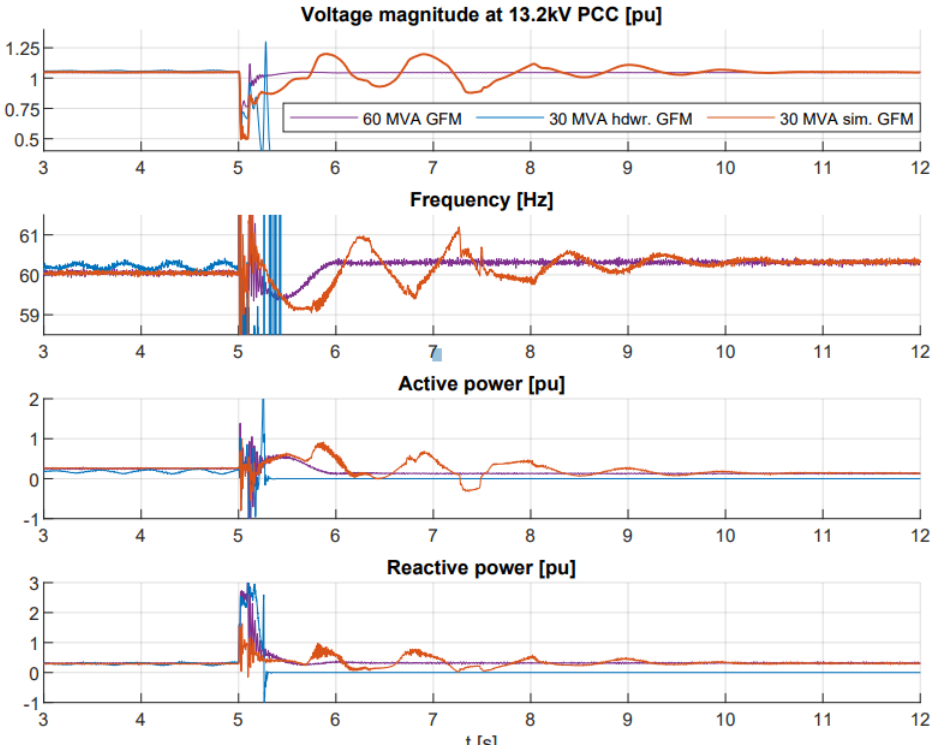

Figure 48. Scenario 7 (zero synchronous machines) fault event with 30 MVA and 60 MVA of inverters in GFM mode. The 30 MVA case is run with the GFM plant implemented in hardware (blue) and in simulation (red). Note that all traces are measured at the hardware inverter's 13.2 kV PCC, and the two cases with 30 MVA of GFM appear very different.

3.6.2.4 Summary

The PHIL test results experimentally verify several key conclusions of the Maui PSCAD study conducted earlier, including:

- In higher system strength scenarios (S1 and S2), the system was stable both with and without GFM controls.
- In low system strength scenarios (S3-S5), a single HPP in GFM mode (either of the two 30 MVA capacity Kuihelani plants) was sufficient to stabilize the system, whereas with no GFM IBR, the system is unstable or marginally stable in those scenarios. This is true whether the GFM HPP is included in hardware or inside the real-time simulation.
- In the zero-inertia (or extremely low system strength) scenario, S7, both Kuihelani plants (60 MVA capacity) are needed to be operated in GFM mode to stabilize the 144 MW system.

- The stabilizing effect of HPPs in GFM mode is robust to both the loss of the largest generator and to a severe 5-cycle fault at a low short circuit ratio bus.
- In the scenario with zero synchronous generation but significant synchronous condensers, S6, GFM controls were not necessary to stabilize the system – it was stable with all IBRs using GFL controls.

As far as we are aware, this is **the first time a real hardware GFM inverter has been shown to stabilize an otherwise unstable bulk power system** (i.e., a power system with many geographically separated generators interconnected by a transmission system). In addition, we believe it is **the first time a MW-scale GFM inverter has been shown to stabilize a bulk power system with zero inertia** (i.e., no synchronous generators or condensers). While both of these results align with our expectations from theory and EMT simulation, the demonstration at MW-scale in hardware is a significant step towards future operation of 100% IBR bulk power systems.

It is important to note that this does not mean bulk power systems can be immediately operated in scenarios such as those studied. Remaining concerns include but are not limited to:

- Will protection systems operate safely in scenarios with very low fault current (and with fault current having significantly different sequential components and other characteristics from synchronous machine fault current)?
- This PHIL study used one commercially available GFM inverter. Inverters from at least two other manufacturers are currently planned to be deployed in Maui HPPs, and control implementations between manufacturers may vary widely. Will other GFM control implementations provide similar results?
- This study has focused on control stability and has intentionally removed nonlinearities such as underfrequency load-shedding controls and DER trip and momentary cessation behaviors. What impact will these have on system stability during contingency events?
  What other challenges will arise in the field that did not show up in PHIL or EMT simulations?

3.7 240-bus WECC Test System Development

A reduced 240-bus WECC test system in Figure 49 has been developed to validate the MIDAS framework, which has also been improved and can be used by others for verifying their research ideas on analyses and controls. The original model in [22] contains scheduling data that have been benchmarked against the operation data. But that model misses dynamic data. We extended that model by (i) developing a power flow base case reflecting the realistic generation resource mix of the actual WECC system in the year of 2018 [23], (ii) adding positive-sequence dynamic models for synchronous generators, exciters, governors, and IBRs [23], and (iii) adding power system stabilizers [24]. To the best of our understanding, this reduced 240-bus WECC test system is the only open, interconnection-level test system, in the public, with IBR dynamic models included in its

dynamic data.

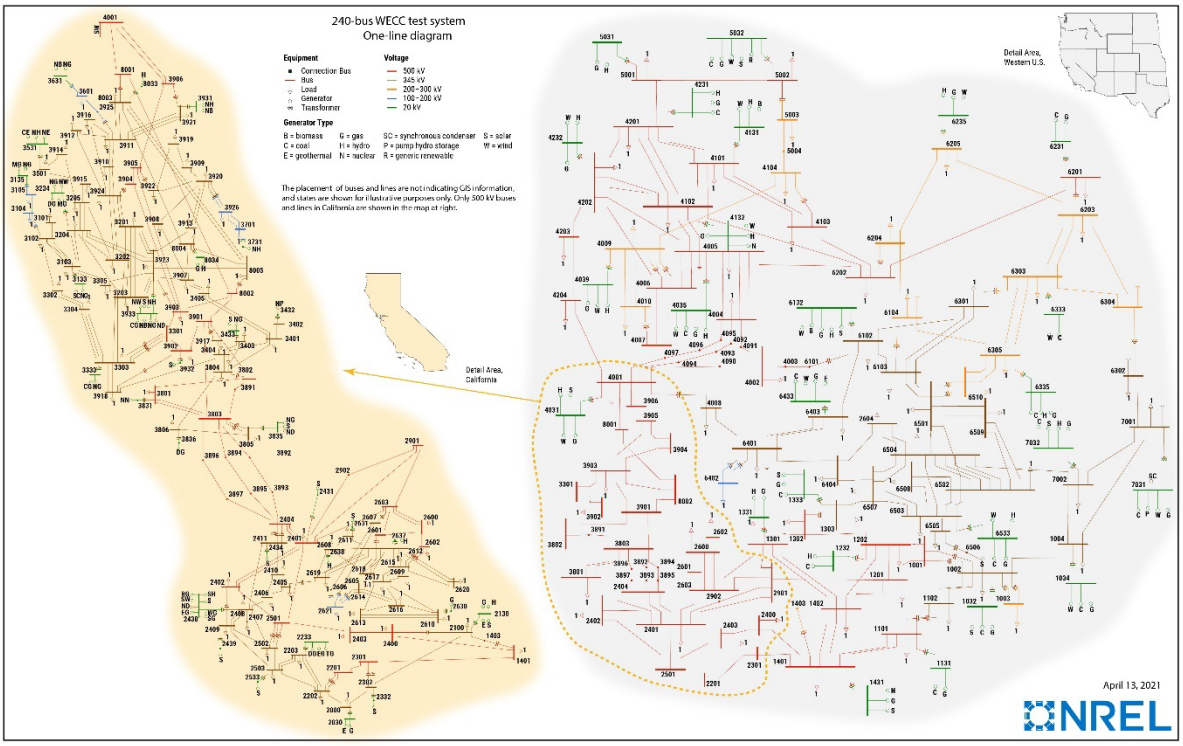

Figure 49. One-Line diagram of the reduced 240-bus WECC test system

This newly developed model has been made available to the public from NREL [25]. More details on the development can be found in [26]. So far, this 240-bus WECC Test system has been used for 2021 IEEE NASPI Oscillation Source Location Contest and more than 8 other projects. It has been providing the training data set for machine-learning-based dynamic stability assessment [27], validating an automated tool for obtaining AC power flow solution [30], and providing various oscillation scenarios for testing oscillation detection algorithms [31] and providing one-year dispatchable power flows for robust PSS design, etc.

3.8 Machine-learning Based Security Assessment

Milestone 1.2.1: Develop data-driven security assessment (DSA) criteria that will be suitable for triggering the dynamic simulation.

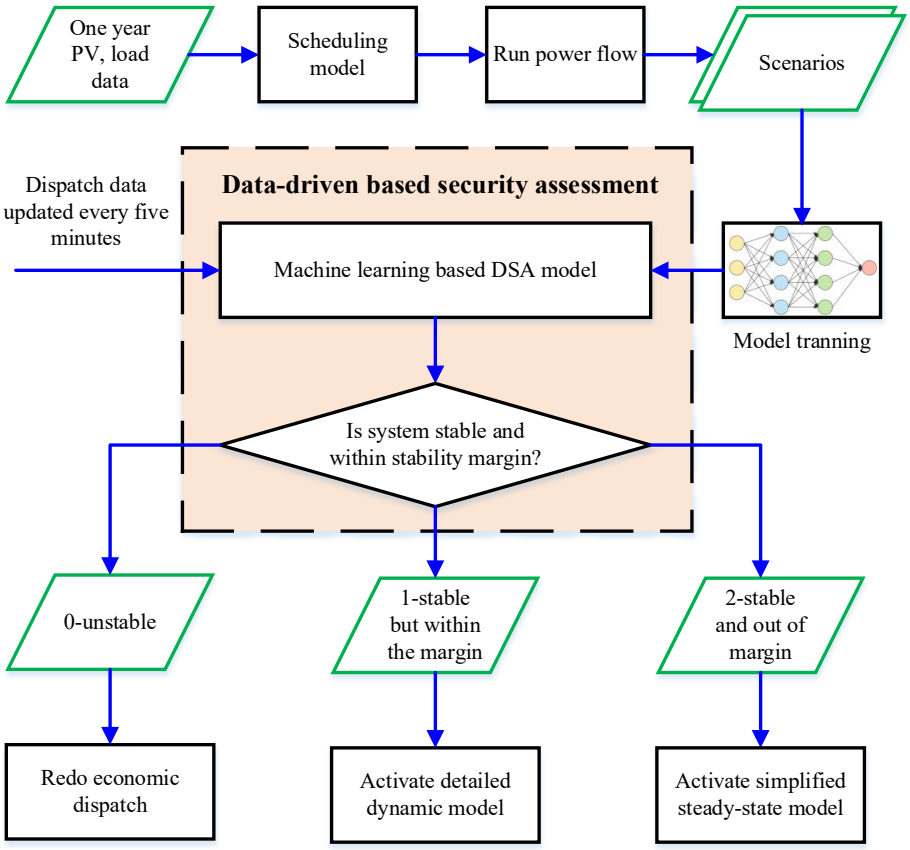

Figure 50. Framework of machine learning-based DSA

Machine learning (ML) or artificial intelligence (AI) based data-driven stability assessment (DSA) can help determine when it is necessary to trigger a dynamic simulation. It can bridge the gap between a short-term full dynamic simulation and long-term scheduling simulation. The framework of this method is illustrated in Figure 50. This work develops the methods for machine-learning-based DSA technology. The margin results obtained by this DSA tool help select simulation approaches with different levels of simulation details and complexity.

Figure 51 shows the detailed DSA flowchart. Generation dispatch data and load data from the scheduling model are used to develop AC power flow. Chronological AC power flow scenarios for an extended period (for example, one year) are obtained, and stability margins are then assessed based on detailed simulation and analysis. The power flow data and the stability margins are used for the machine learning model training. After training, the machine learning model can be used to predict the stability margin for a specific power flow scenario. If the estimated stability margin indicates an unstable system, a command is sent to the scheduling model to generate new dispatch data. If the system is stable and the stability margin is large enough, the simplified steady-state model will be activated for simulation. If the system is stable but within a small stability margin, a detailed dynamic model is used for full dynamic simulation to quantify the stability more accurately.

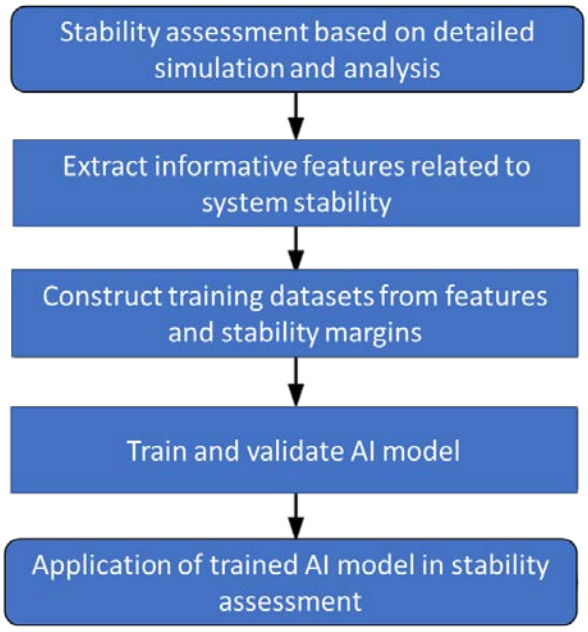

Figure 51. Flowchart of machine learning-based DSA

The 18-bus test system and the reduced WECC test system are used to develop and validate the developed DSA tool. The following four stability assessment use cases are developed in this study.

- AI-based transient stability assessment.
- AI-based frequency stability prediction.
- AI-based small signal stability assessment
- AI-based WECC-1 Remedial action scheme (RAS) Improvement

An example of AI-based transient stability assessment is provided here. More details and other use cases can be found in a separate task report in the Appendix B.

Transient stability is the power system ability to maintain synchronism when subjected to a severe disturbance, such as a short circuit on a transmission line. The maximum allowable fault-clearing time for the system to remain stable is known as critical clearing time (CCT). A larger CCT value generally indicates higher angle stability. The distribution of CCT values of one bus (Bus 1002) in the 240-bus system is shown in Figure 52. (Bus 1002 was selected because of lower CCT values compared with other buses.) It can be seen that the CCT values in summer peak hours are obviously lower, partially due to the higher loading levels of generators during summer peak hours.

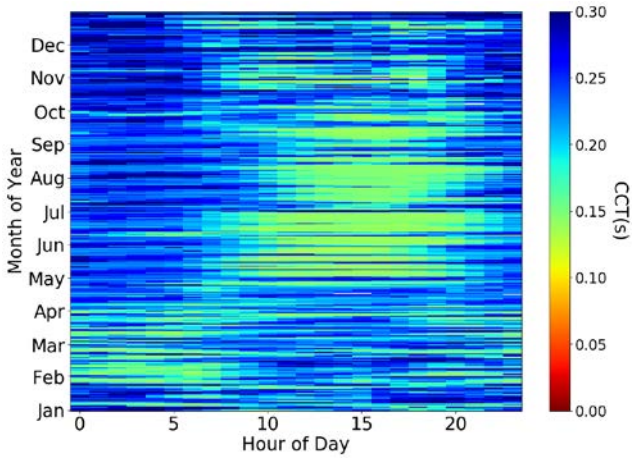

Figure 52. Distribution of the CCT values in one year (Bus 1002)

Neural network is applied to predict CCT values of the 240-bus reduced WECC system. The input and output data information are given in **Table 13**. The data set is divided into two subsets: 80% data are used for training (68%) and validation (12%), and the remaining 20% data are used for testing.

Table 13. Data Entries for CCT Prediction

Input/Output	Data	Number of Data Entries
Input	Total generation	1
	Total load real power	1
	Total system inertia	1
	Generator power output	146 (number of generators)
	Load power	139 (number of loads)
	Generator's inertia contribution	146 (number of generators)
Output	CCT	1

The CCT prediction performance and error distribution are shown in Figure 53. The Mean Absolute Error (MAE) of all prediction points is 0.00607s, which is around 4% of the average CCT value. The distribution of the error is almost symmetric to the Y axis. This indicates a desired feature that errors have a close-to-zero expectation. In addition, it can be noticed that the CCT prediction error is smaller when the CCT value is smaller, which is also a preferable feature since scenarios with low CCT values are more important for operators.

Figure 54 shows the CCT prediction performance of two days. It is noted that although the CCT values change dramatically with the power flow within one day, the machine learning tool can assist real-time fast stability assessment by predicting the angle stability margin accurately. It can also verify the observation that the prediction errors are smaller

for smaller CCT values.

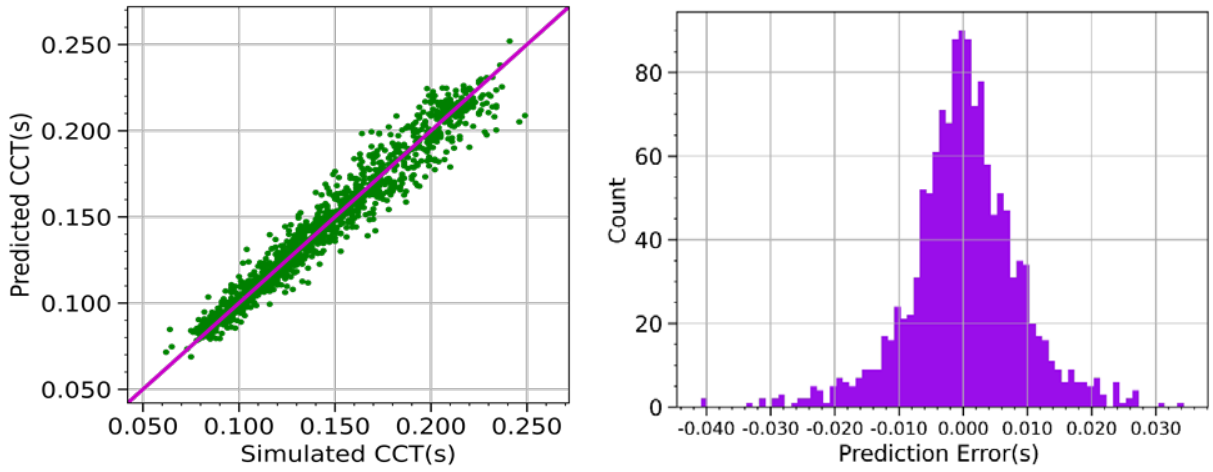

(a) (b)

Figure 53. CCT prediction performance and error distribution. (a) CCT prediction results for multiple days. (b) CCT prediction error

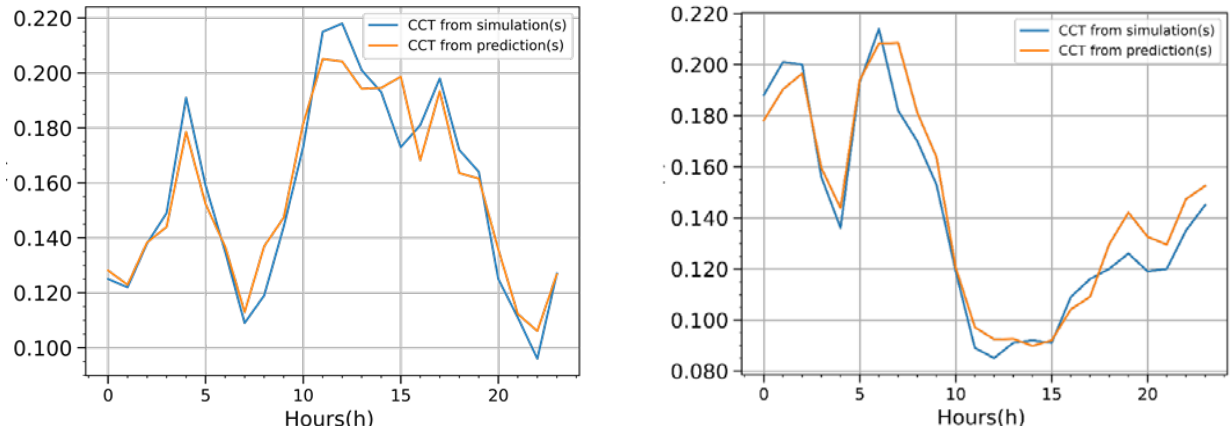

(a) Jan. 20 (b) Aug. 5

Figure 54. CCT prediction results of two days

3.9 Tools Developed Under MIDAS Project

3.9.1 MIDAS Tool

The Multi-timescale Integrated Dynamics and Scheduling for Solar (MIDAS-Solar) is a multi-timescale power system operation simulation tool which integrates the power system economy scheduling from day ahead to real time and the AGC dynamic responses analysis across different timescales with modern PV power plants. Detailed development and introduction of the tool can be found in a separate document called “MIDAS TOOL MANUAL_V2.0” [38].

We also provide a user-friendly graphic user interface of MIDAS tool as shown in Figure 55. The user guide is in a separate document called “MIDAS_GUI_Manual_V1.0” [39].

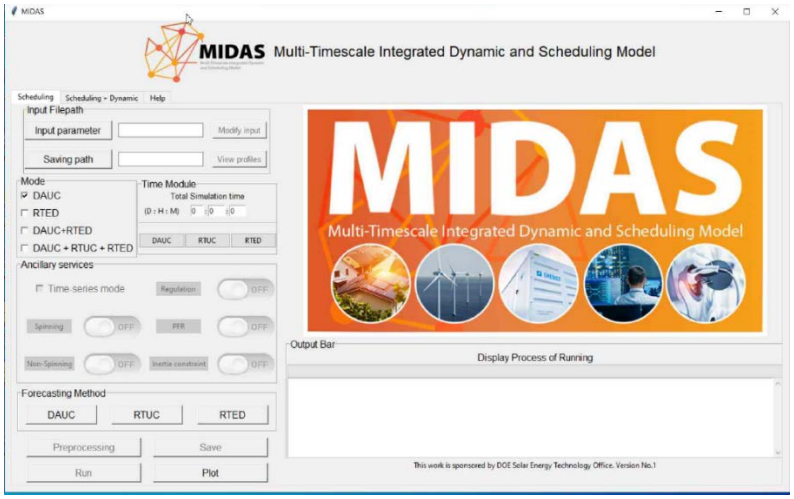

Figure 55. GUI of MIDAS tool

3.9.2 DC2AC Tool

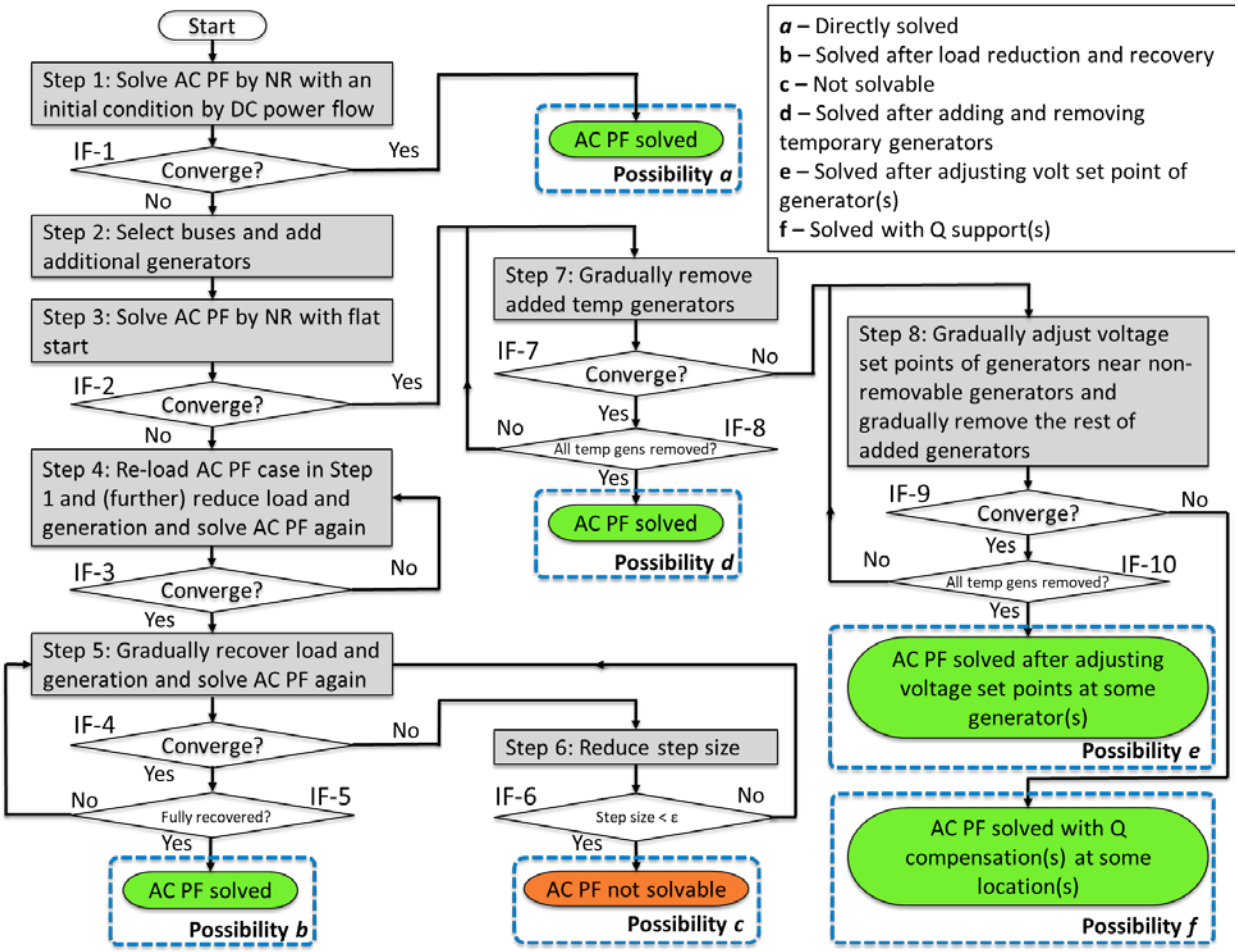

Figure 56. Flowchart of the DC2AC tool

DC2AC Tool is an automated tool for achieving a converged AC power flow solution from any dispatch determined using a DC model-based optimal power flow. This tool assists MIDAS could do the continuous closed-loop simulation between the scheduling and dynamics. The entire process is free of human intervention. This tool first achieves a solvable AC power flow case by modifying the power flow condition and then to try to track the AC power flow solution while gradually removing the adopted changes. If all adopted changes can be completely removed, then the original AC power flow solution is obtained. Otherwise, insights into actionable controls are derived to help in operation and planning. Currently, this tool has been implemented in Python using Siemens PTI PSS/E as the power flow solver. Detailed development and validation process of the tool can be found in [30]. This tool has been made free and open source on GitHub [32].

3.9.3 PSS/E Network Reduction Tool

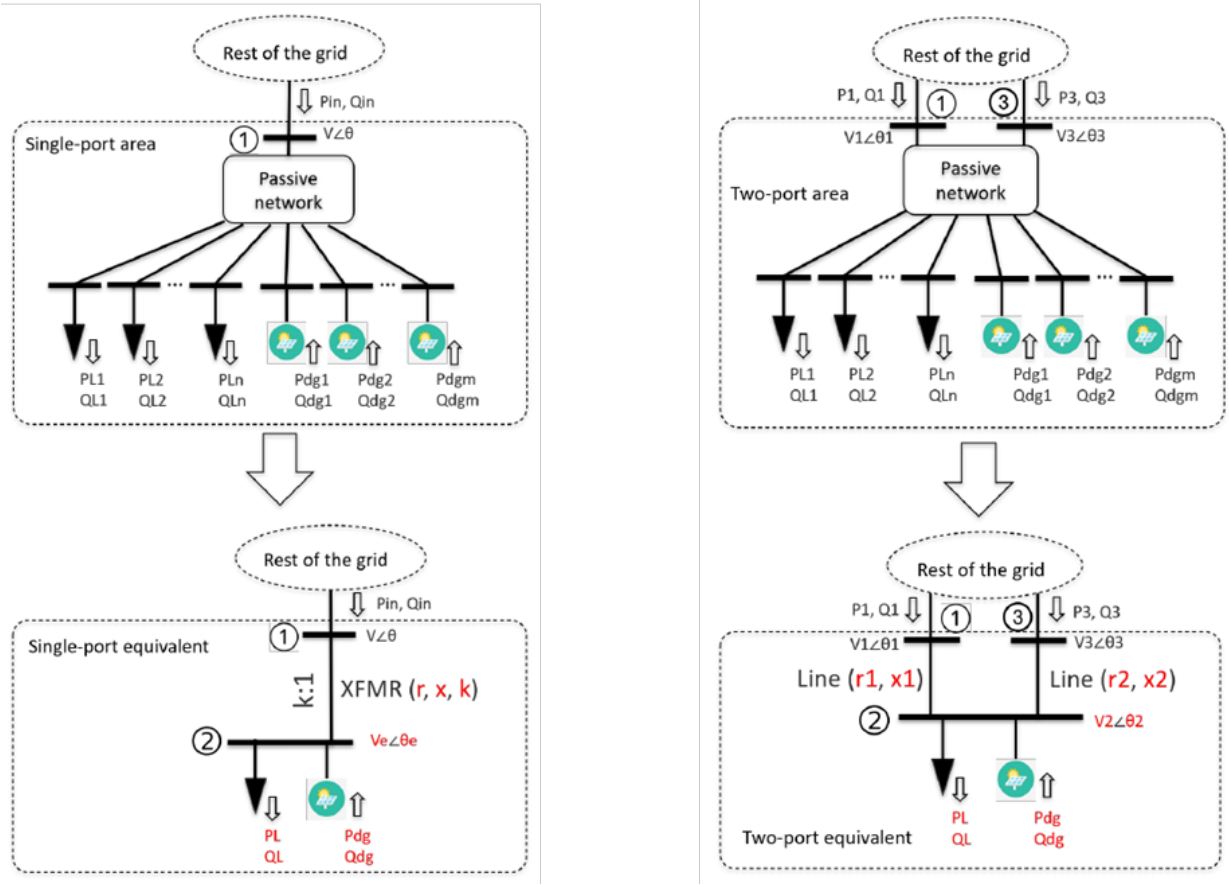

Figure 57. Single-port (left) and two-port (right) reduction techniques

This network reduction tool is named PsseReducer, which is based on Python and PSS/E. PsseReducer adopts the single-port and two-port reduction techniques proposed in [21] to reduce power system network models. The adopted reduction techniques can preserve the voltage and power at the port(s) of the reduced subnetwork and keep the power flow pattern in the rest of the system unchanged. This tool has been made free and open source on GitHub with examples [33]. In this project, PsseReducer has been used to create reduced Maui Grid for the PHIL testing.

3.10 Technical Summary

This project proposes an innovative multi-timescale simulation framework of integrated scheduling and dynamic model (MIDAS) to study performance of PVs providing frequency control ancillary services (FCAS). We discuss motivation for introducing MIDAS to quantify the performance of FCAS for high renewable penetrated grid. MIDAS models the power grid operations and control for FCAS by including PFR and AGC expression and constraints in scheduling model and a true physical representation of centralized AGC, detailed dynamics of other PFC units and second-level solar and load variations. It can simulate the power grid from day-ahead unit commitment to second-level frequency

dynamic seamlessly and continuously. Therefore, it can link FCAS in RTED with actual implementation through PFC and AGC at a high time resolution. MIDAS is applicable to study the impacts of high penetrations of renewables at a broad range of timescales, compare different advanced controls, operation strategies, and generation technologies for FCAS, and reveal the insight of interaction between PFR and AGC by providing quantified reliability and cost information simultaneously.

Our case studies demonstrate that 1) the traditional regulation requirement could be short for a high PV penetrated grid on a cloudy day based on simulated reliability metrics and the requirement needs to be improved by considering PV variations under different weather condition; 2) When PV is providing stacked PFR and AGC reserve, there is a risk to overtake the other reserve during the ramp of sunset or sunrise, and it might result in insufficient PFR and AGC when needed; 3) Fast response IBR is a good candidate for FCAS provider, while detailed economic analysis is needed for a specific system. Specifically, we should consider the trade-off between opportunity cost and revenue gained from FCAS.

From the EMT study of Maui Grid, we have found that phasor-domain simulation may encounter numerical instability and misses key system dynamics in some very weak grid scenarios. Modeling inverter control loops (power and current) of GFL devices is required to detect faster modes in the system response under very weak grid conditions. Study indicates that the presence of synchronous generators is not necessary for the system stability. The power system can be stable with GFL and synchronous condensers or GFM inverters plus GFL.

Presence of a single GFM (30 MVA) greatly increases damping, ROCOF, and nadir of primary frequency mode in weak grid scenarios (145 MW total load). Through MW-scale PHIL experiment, we confirm that introducing two GFM plants (60 MVA total) stabilizes zero-inertia system (145 MW total load).

We believe that when we are moving forward to 100% renewable grid, the integrated economics and reliability study and simulation like this should be helpful for system operators to fully understand the risk and benefit of implementing new products and controls for FCAS in their planning and operation stage and therefore secure future power grid.

4 Significant Accomplishments and Conclusions

This project has developed Multi-Timescale Integrated Dynamic and Scheduling (MIDAS) study framework to address the challenge of operating the grid with extremely high renewable penetrations by bridging the modeling and analysis gaps of different timescales between economics, reliability, and stability of grid operation.

MIDAS will be the first of its kind framework to model and analyze the impact of PV systems on system dynamics, reliability, and economics at all time spectrums. MIDAS will:

- Provide information about the impacts of PV on grid economics and reliability simultaneously.
- Enable PV to provide grid services for power systems with high penetration of solar by seamlessly studying technical feasibility and economic feasibility.
- Help stakeholders understand what types of advanced controls PV can support grid operation (control), when PV is needed to provide grid reliability services (impact analysis), the revenue stream for PV to become a grid-service provider, and how to incentivize PV (market).
- Identify the possible stability issues of an IBR-dominated system by using full EMT simulation and propose the mitigation methods.

4.1 Featured Accomplishment

Provide a panorama for grid with high PV penetrations: The power system model in MIDAS can provide multi-timescale comprehensive information on economics, reliability, and stability from resource adequacy (years to days) and energy balance (days to minutes) to frequency dynamics (minutes to seconds) and EMT (sub-second) timescales.

MIDAS touch for Maui grid operational planning: One-year (8760 hours) scenarios for 2022 Maui grid are investigated in MIDAS to help Maui planner evaluate the proposed existing fixed minimum inertia requirement.

Develop the first-of-a-kind, full-scale EMT model of the entire Maui transmission system: the EMT model shows that Maui system stability can be maintained while operating with 100% IBRs (PV, wind, and energy storage). Our simulations indicate that this unprecedented operation scenario can be achieved with synchronous condensers, GFM inverters, or a combination of the two technologies.

A megawatt-scale PHIL testing bed with real-time EMT model of Maui grid: In our PHIL simulations, we connect a real, MW-scale GFM inverter to a real-time EMT simulation model of Maui system.

Multi-timescale test systems: To tackle the challenges of high renewables integration,

NREL researchers develop a set of test systems by providing one-on-one models and data for scheduling, power flow, and dynamic study. The 240-bus WECC Test system has been used for 2021 IEEE NASPI Oscillation Source Location Contest and more than 8 other projects so far. All the test systems can be found in the Test Case Repository for High Renewable Study.

4.2 High-level Conclusions

In this project, we have successfully developed a MIDAS tool, which could enrich existing planning and operational tools for conducting reliability and stability analysis down to the fast time-scale dynamics. Unlike current commercial tools, MIDAS bridges the gaps between the economic analysis and dynamic reliability evaluations of grid operation. Thus, grid operators can see the trade-offs of dispatching renewable (and nonrenewable) assets for a variety of grid services.

So far, MIDAS has helped Maui to plan ahead for more renewables by modeling its operations under future high solar scenarios. The Maui model in MIDAS can identify potential reliability and stability issues before they happen, from resource adequacy (years to days) and energy balance (days to minutes) to frequency dynamics (minutes to seconds) and EMT (sub-second) timescales, providing a uniquely complete picture of Maui's high-renewable system.

4.2.1 Learnings from a Multi-timescale Simulation Approach

In the multi-timescale study of Maui Grid, the simulation shows that it becomes more challenging to ensure the grid stability from a scheduling perspective. Grid planners and operators need to carefully design and implement inertia/dynamic related constraints because these frequency-dynamic-related constraints have never been included in the existing scheduling model of the commercial software. Any newly proposed services/constraints need to be tested and validated beforehand through MIDAS or similar simulation/study framework.

The project has demonstrated the pros and cons of a fixed minimum inertia requirement for Maui Grid. Also, we propose a new adaptive operational constraint that aims to avoid underfrequency load shedding after severe contingencies anytime based on the grid operational conditions.

4.2.2 100% IBR Operation is Achievable in EMT Simulation and PHIL Testing

In the Maui 100 EMT study, the simulation indicates that there are three pathways for Maui grid to achieve a stable operation of a 100% renewable energy grid in terms of inverter technologies. One way is to use GFL and synchronous condensers, the second way is to use GFL and GFM, and the third one is to use a hybrid method which combine GFL, GFM, and synchronous condensers. In addition, GFM has been identified as an effective technology to increase damping, reduce ROCOF, and improve nadir of primary

frequency mode in weak grid scenarios.

The project has demonstrated that 1) Maui system can be stable with GFL and synchronous condensers; 2) We can use two GFM plants (60 MVA total) to stabilize zero-inertia Maui system (145 MW total load), and this is validated through EMT simulation and MW-scale PHIL experiment.

Note that the above conclusions are based on transient stability analysis, and we have not considered other topics necessary for 100% IBR operation, e.g., protection, reserves, and resource adequacy.

The MIDAS methods and high-level conclusions can be generalized to other island grids and interconnections. But some other specified questions need to be studied and addressed further based on the characteristics of the different grids.

5 Path Forward

The MIDAS-Solar project focused on key technical challenges from two main aspects when the grid is transitioning to 100% renewable energy. These two key aspects include 1) how could we ensure the grid reliability with high PV penetrations through advanced control and new ancillary services from PV; 2) how shall we maintain grid transient stability when the grid is operating with 100% renewables or even with IBRs. There are some follow-up research topics that can be considered when we move to next steps.

5.1 System Planning and Operation

To maintain high levels of reliability and stability of bulk power systems, changes will be needed for both transmission systems and IBRs. The existing practices at various timescales—planning, day-ahead scheduling, real-time dispatch and operation and transient stability, at all levels—transmission, generation, distribution, and storage systems will need to adapt.

The MIDAS-solar project has pointed out that some interactions among different timescales need to be considered in the design and analysis stage, and new control technologies need to be developed and deployed for the future IBR-dominated system. The future directions consist of many aspects such as design, analysis, control, operation, and planning. Here, we name a few of them:

1) Controls of IBRs could become more complicated from both device and system levels. So far, system operators haven't fully used the fast response capabilities from IBRs. Some engineers tend to try to make IBRs perform as synchronous machines so that the system-level design doesn't introduce dramatic changes. However, the future IBR-dominated grid has to consider the high flexibility and controllability of IBRs, because of new power system dynamic characteristics (e.g., low inertia, low short-circuit ratio, etc.). So, we might make future IBRs perform better than existing IBRs as well as better than traditional synchronous machines on some aspects. That transformation will lead to a set of new questions such as how we should consider the fast response/control capability in IBRs in the planning stage, how we re-elevate the resource adequacy with IBRs to ensure grid stability, and how we could properly design the new system-level ancillary services for IBRs to fully use/incentivize new controls of IBRs. Further, the IBR control algorithms may interact with other dynamic components in the bulk power systems, like other IBRs or high-voltage dc transmission. This could complicate the design, control, and analysis of IBR-dominated power systems.
2) We need to fully understand the stability mechanism of the future IBR-dominated system. If the grid structure or characteristics of the dominant dynamic components is dramatically changed, the modeling and analysis methods will need to be updated accordingly to ensure the system's reliability, security, and stability. For example, the existing scheduling model couldn't guarantee the system stability, therefore, some new tools such as MIDAS are needed for the future

planning study. Further, we need to revisit the stability mechanism in this new paradigm. We need to understand the limitations of existing simulation-based analysis tools and methods. The MIDAS-solar project has identified some new stability issues that need to be captured in EMT simulations. However, to fully understand the dynamic characteristics of an IBR-dominated grid such as the high-frequency oscillations introduced by wind, PV and even batteries in the field, more research efforts are required in this field.

5.2 Advanced Coordination Between Solar and Storage

Given the flexibility of energy storage, pairing a PV plant with a BESS in an HPP provides a promising solution for system operators to improve PV dispatchability and predictability while providing fast response capability to augment or substitute traditional power plants' inertial response. Facing the fast-increasing capacity of utility-scale HPPs, grid operators expect HPPs to take a more essential role than before, ensuring system-wide stability, reliability, and flexibility of grid operation. However, most HPPs are still treated as non-dispatchable and uncontrollable resources in scheduling, and advanced grid controls of HPPs are rarely considered in practice. Because there are more technical challenges that need to be addressed first. The future research topics include:

- How to develop advanced coordination/control strategies of PV and battery and maximize usage of the battery capacity for energy arbitrary and fast power response?
- How could system operators work with HPP vendors and coordinate the operations of HPPs and stand-alone batteries?
- Development of plant-level optimal coordination of PV and BESS to meet the system-level control command.
- Development of versatile HPP controls for multiple grid services.

5.3 Plans for Tools Developed Under the Project

Under the MIDAS project, we have obtained four software records as introduced in Section 3.9. These developed tools are summarized in **Table 14**.

Table 14. Future Plans for Four Tools Developed Under the MIDAS Solar Project

Tools	Software record	Plan	Further development
MIDAS Tool	NREL SWR-21-97	Commercialization	Yes
MIDAS-DC-AC Tool	NREL SWR-21-39	Commercialization Open source	Yes
Network Reducer Tool	NREL SWR-21-55	Open source	No Plan
PyPSCAD	NREL SWR-20-64	Open source	No Plan

For MIDAS tool, the collaboration with our utility partners to use MIDAS has initially demonstrated the market needs. The next steps include:

- Further develop the multiple-timescale models and components including battery energy storage, pump hydro storage, etc.
- Further enhance the functionality of DC-AC Tool by using AC-OPF method.
- Including the open-source power system simulation package in a fully open-source simulation package.
- Try to commercialize the tool with potential software vendors (e.g., GE) by including the use of commercial tools within the modular co-simulation framework. Meanwhile, we will keep working with utilities and demonstrating the use cases and capabilities of MIDAS tool.

5.4 Development of the 240-bus WECC Test System

For the 240-bus WECC Test System, our final goal is to develop a realistic (but not real) interconnection-level test system that enables both academia and industry users to address the challenges of integrating high penetrations of IBRs.

To address different problems associated with various timescales, this test system has been designed to span multiple timescales with a set of inputs and model parameters. The overall development pathway at different timescales is shown in Figure 58.

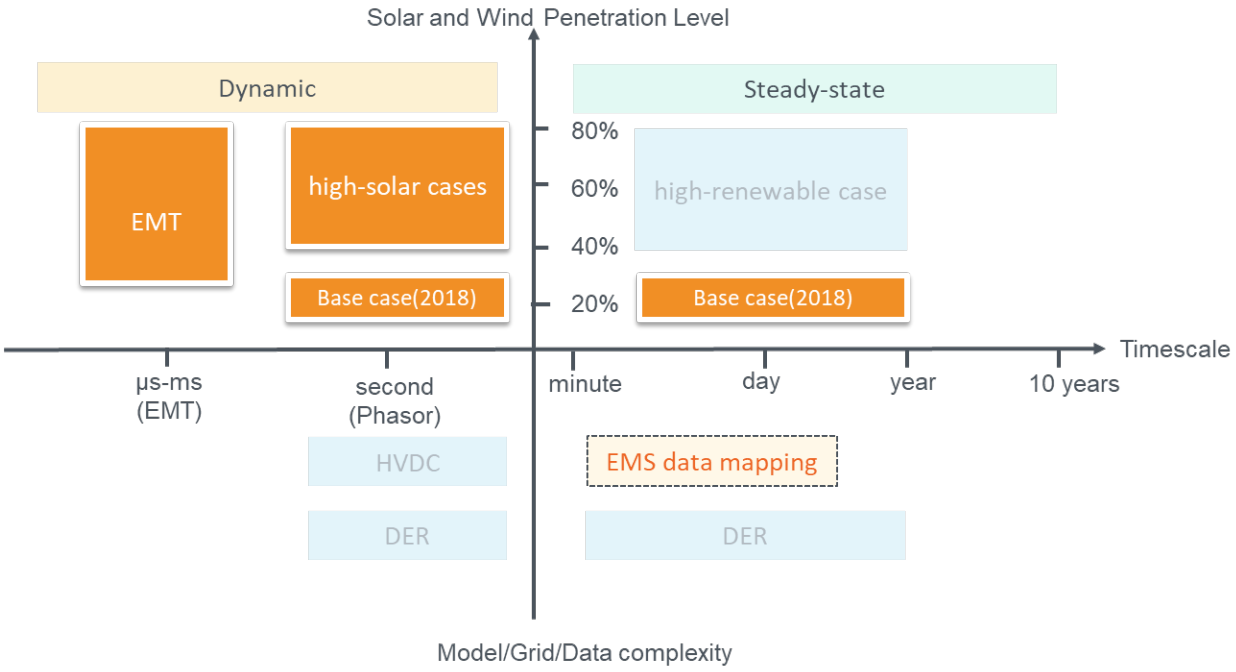

Figure 58. Development pathway of 240-bus WECC test system

Under MIDAS project, we have developed a one-on-one matched reduced 240-bus WECC test system for both scheduling and dynamic simulation. Also, high IBR penetration scenarios are developed considering the UPV/DPV technical potentials in

each of the 11 U.S. states in this reduced WECC test system.

As highlighted in Figure 58, compelling future works are summarized as follows:

- **Full EMT model development**: We will include detailed GFL and GFM models. (An on-going effort supported by a LDRD)
- **High renewable penetration scenarios development**: Future high renewable scenarios will require additional mapping from the WECC planning study, e.g., the future capacity expansion and time-series generation data of IBRs and load data.
- **IBR modeling**: 2nd generation renewable dynamic models, which are the latest renewable dynamic model, are used for this work. These models have limitations and may encounter numerical issues under low short-circuit-ratio conditions. Newer renewable dynamic models addressing those numerical issues are available in academia and have been integrated to commercial software, including PSS/E which is used for this work. In addition, HVDC lines have been modeled as positive load and negative load so far. To investigate the dynamic interactions between HVDC lines and IBRs, we will replace them with the detailed inverter control models.

5.5 Community Engagement

The MIDAS-Maui study has identified some potential technical routes for 100% renewable pathways. These transitions (e.g., GFM deployment, hybrid PV and battery energy storage, ancillary services requirements, etc.), are less likely to be successful if the proposed methods are not adopted by utilities, approved by regulators, and welcomed by a local community. In this regard, next steps include:

- For the short term, the results disseminations and discussion will be key to gain the public trust and get their support.
- For the long term, to build up a long-term trustful collaboration relationship with utility partners, we will focus on their needs, develop customer-focused projects, and continuously deliver the high-quality research outputs.

6 Inventions, Patents, Publications, and Other Results

Software Records

[1] Multi-timescale integrated dynamic and scheduling model (NREL SWR-21-97)

[2] Network Reduction Tool (NREL SWR-21-55). Available at https://github.com/NREL/PSSE_Network_Reduction

[3] MIDAS-DC-AC Tool: Fully Automating the Acquisition of AC Power Flow Solution (SWR-21-39)

[4] PyPSCAD: Library of Python code for interacting with parallelized PSCAD models, as well as detailed, scalable PSCAD grid-following and grid-forming inverter models," (NREL SWR-20-64). Available at https://github.com/NREL/PyPSCAD

Open-source Test Cases

[1] Test Case Repository for High Renewable Study. https://www.nrel.gov/grid/test-case-repository.html

Journal Papers (8 published/accepted, 2 in preparation)

[1] S. You, etc., Build Smart Grids on Big Data and Artificial Intelligence — a Real-world Example," Energies, AIPES 2020 special issue.

[2] S. Yin, J. Wang, Z. Li, and X. Fang, "State-of-the-art Electricity Market Operation with Solar Generation: A Review," Sustainable and Energy Renewable.

[3] A. Hoke, V. Gevorgian, S. Shah, P. Koralewicz, R. W. Kenyon, and B. Kroposki, "Island Power Systems with High Levels of Inverter-based Resources – Stability and Reliability Challenges," IEEE Electrification Magazine, March 2021.

[4] X. Fang, H. Yuan, and J. Tan, "Secondary Frequency Regulation from Variable Generation Through Uncertainty Decomposition: An Economic and Reliability Perspective," IEEE Transactions on Sustainable Energy.

[5] Y. Zhao, etc., "Deep Learning-based Adaptive Remedial Action Scheme with Security Margin for Renewable-Dominated Power Grids," Energies.

[6] L. Zhu, Y. Zhao, et al., "Adding Power of Artificial Intelligence to Situational Awareness of Large Interconnections Dominated by Inverter-Based Renewables," High Voltages.

[7] J. Cochran, C. Bak, P. Francos, etc., "Same Goal, Different Pathways for Energy Transition", IEEE Power Magazine. (to be published)

[8] J. Tan, H. Yuan, Y. Zhang, etc., "A Multi-Timescale Framework to Study the Performance of High-Penetration of Renewables Providing Frequency Ancillary Services," (submitted to IEEE Trans on Sustainable Energy)

[9] X. Liu, X. Fang, etc. “Machine Learning Based Frequency Stability Constrained Unit Commitment: An Island System Study” (plan to submit it to IEEE Trans on Sustainable Energy)

[10] A Hoke, P. Koralewicz, B. Wang, and R. W. Kenyon, Li Yu, Kelcie Kawamura, Jin Tan, “Stability of Inverter-based Transmission Systems: Power Hardware-in-the-Loop Experiments with a Megawatt-scale Grid-forming Inverter,” IEEE Electrification Magazine, September 2022.

Conference Papers (18 published/accepted; 1 submitted)

[1] R. Biswas, J. Tan, H. Jain, V. Gevorgian, and Y. Zhang, “Equivalent Test Bed in PSCAD and PSLF for Studying Advanced Power Systems Controller Performance,” IEEE 2019 ISGT North America Conference.

[2] H. Xiao, S. Fabus, S. You, etc., “A Unified Machine Learning Approach for Data-driven Security Assessment of Power Grids,” presented in CIGRE. (FY20Q1)

[3] H. Yuan, R. S. Biswas, J. Tan, and Y. Zhang, “Developing a Reduced 240-Bus WECC Dynamic Model for Frequency Response Study of High Renewable Integration,” T&D 2020.

[4] R. Kenyon, A. Hoke, J. Tan, and B. Hodge, “Grid-Following Inverters and Synchronous Condensers: A Grid-Forming Pair?” present on-line for 2020 IEEE Clemson University Power System Conference.

[5] H. Jain, M. Sengupta, A. Habte, and J. Tan, “Quantifying Solar PV Variability at Multiple Timescales for Power Systems Studies,” presented at PVSC 2020.

[6] S. You, etc., “Deploy Artificial Intelligence in Smart Grids — an FNET/GridEye Example,” submit to European Conference on Artificial Intelligence 2020.

[7] S. You, etc., “A Review on Artificial Intelligence for Grid Stability Assessment,” In 2020 IEEE International Conference on Communications, Control, and Computing Technologies for Smart Grids (SmartGridComm) (pp. 1-6). IEEE.

[8] R. Kenyon, B. Wang, A. Hoke, J. Tan, and B. Hodge, “Validation of Maui PSCAD Model: Motivation, Methodology, and Lessons Learned,” NAPS 2020.

[9] S. Yin, J. Wang, Y. Lin, X. Fang, H. Yuan, and J. Tan, “Practical Operations of Energy Storage Providing Ancillary Services: From Day-ahead to Real-time,” NAPS 2020.

[10] X. Fang, J. Tan, H. Yuan, S. Yin, and J. Wang, “Providing Ancillary Services with Photovoltaic Generation in Multi-Timescale Grid Operation,” NAPS 2020.

[11] B. Wang, A. Hoke, and J. Tan, “Power System Network Reduction for Power Hardware-in-the-Loop Simulation,” IEEE Kansas Power and Energy Conference, 2021.

[12] R. Kenyon, A. Sajadi, A. Hoke, and B. Hodge, “Introducing Generic PSCAD GFL and GFM Models: Demonstrated on the IEEE 9 Bus System,” IEEE Kansas Power and Energy Conference, 2021.

[13] A. Habte, M. Sengupta, H. Yuan, G. Buster and J. Tan, “Simulation of PV Variability as a Function of PV Generation and Plant Size,” 2021 IEEE 48th Photovoltaic Specialists Conference (PVSC), 2021, pp. 2136-2140, doi: 10.1109/PVSC43889.2021.9518528.

[14] Lizhi Ding, Xiaonan Lu, and Jin Tan,” Comparative Small-Signal Stability Analysis of Grid-Forming and Grid-Following Inverters in Low-Inertia Power Systems,” IECON2021.

[15] R. W. Kenyon, A. Sajadi, B. Hodge, and A. Hoke, “Criticality of Inverter Controller Order in Power System Dynamic Studies – Case Study: Maui Island,” accepted by Power Systems Computation Conference.

[16] L. Ding, X. Lu, and J. Tan,” Holistic Small-Signal Stability Analysis of Low-Inertia Power Grids with Inverter-Based Resources and Synchronous Condensers,” ISGT2022.

[17] Y. Zhao, S. You, …, and J. Tan, “Fast and Accurate Transient Stability Assessment Method Based on Deep Learning: WECC Case Study,” submitted to Hawaii International Conference on System Sciences.

[18] J. Ting, B. Wang, W. Kenyon, and A. Hoke, “Evaluating methods for measuring grid frequency in low inertia power systems”. (accepted by KPEC 2022)

[19] X. Liu, J. Xie, X. Fang, H. Yuan, B. Wang, H. Wu, J. Tan, “A Comparison of Machine Learning Methods for Frequency Nadir Estimation in Power Systems” (accepted by KPEC 2022)

Invited Talks and Presentations (15 presentations)

[1] J. Tan, “Multiple Timescale PV Model for Dynamics and Scheduling,” presented at ESIG Fall workshop 2019.

[2] J. Tan, “Frequency Control and Modeling of Inverter-based Renewables for Grid Study: An Industry Perspective,” presented at PESGM 2019 Panel Session.

[3] H. Yuan and J. Tan, “Multi-timescale Integrated Dynamics and Scheduling for Solar (MIDAS-Solar),” present at Panel Session/ISGT 2020, Washington DC.

[4] H. Yuan, “Machine Learning-based Security Assessment and Control for Bulk Electric System Operation,” present at Panel Session/ISGT 2020, Washington DC.

[5] J. Tan, “Multi-timescale Integrated Dynamics and Scheduling (MIDAS)-Maui Study Cases,” 2020 ESIG Fall technical workshop, November 2020.

[6] J. Tan, “A Machine-learning Approach for Dynamic Security Margin Assessment of Power Grids with High Penetration of Renewable Energy,” MATLAB Utilities & Energy Conference, Virtual, November 2020. (Panel session)

[7] A. Hoke, “Advanced EMT Simulation for Modern Power Grids with GFM and GFL Controls: An Industry Perspective,” IEEE Energy Conversion Conference and Exposition (ECCE) Special Session October 2020.

[8] A. Hoke,” Power HIL Evaluation of Inverter Controls for 100% Inverter-based Bulk Power Systems: A Power Electronics Grid Integration Case Study,” Power Electronic Grid Interface (PEGI) Platform Industry Workshop, NREL October 2020.

[9] W. Kenyon, B. Wang, J. Tan, G. Yau, M. Asano, L. Dangelmaier, and A. Hoke, “Inverter-based Operation of Maui: Electromagnetic Transient Simulations,” NERC Inverter-based Resource Performance Working Group, March 2021

[10] A. Hoke, “Grid Reliability and Inverter-based Resources,” Presented to Northeast Power Coordinating Council (NPCC) DER Forum, February 11, 2021.

[11] W. Kenyon, B. Wang, J Tan, and A. Hoke, “Inverter-based Operation of Power Systems: Electromagnetic Transient Simulations and Grid-forming Inverters,” presented to FERC staff.

[12] A. Hoke, “Operating Power Systems at Near 100% Instantaneous Inverter-based Generation,” EUCI Smart Inverter-based Resources Course.

[13] A. Hoke, “High Penetration PV and Wind in Island Power Systems,” Workshop delivered to U.S. Virgin Islands Water and Power Authority.

[14] A. Hoke, “Grid-Forming Technology: Current Applications and Future Considerations,” IEEE PES General Meeting Panel Session, July 26, 2021.

[15] J. Tan “A Machine Learning Framework for Bridging the Gap Between the Steady-State Scheduling and Dynamic Security Operation for Future Power Grid” IEEE PES General Meeting Panel Session, July 26, 2021.

Technical Report

[1] Wang, Bin, and Jin Tan. "DC-AC Tool: Fully Automating the Acquisition of AC Power Flow Solution". Golden, CO: National Renewable Energy Laboratory. NREL/TP-6A40-80100.2022.

[2] J. Tan, X. Fang, H. Yuan, J. Wang, S. Yin, Y. Lin "MIDAS TOOL MANUAL_V2.0". NREL Internal Report.

[3] X. Liu, X. Fang, J. Tan. "MIDAS GUI Manual" NREL Internal Report.

[4] J. Tan, B. Wang, H. Yuan, X. Fang, etc. "240-bus WECC Test System" NREL Report (in development).

[5] J. Tan, etc. "MIDAS Final Report" (in development).

Media Report

- "NREL Methods Assist Maui in Approaching 100% Renewable Operations -New Capabilities Demonstrate How Renewables Can Stabilize and Support the Power Grid" July 30, 2021
- "As Maui approaches 100% renewables, NREL models grid options" PV magazine, August 2, 2021
- "NREL supports Hawaii's island of Maui on path to 100% renewables", Renewable now, August 4, 2021

References

[1] AEMO. (2019). Regulation FCAS changes. Available: https://www.aemo.com.au/-/media/files/electricity/nem/security_and_reliability/ancillary_services/frequency-and-time-error-reports/regulation-fcas-factsheet.pdf?la=en

[2] N. G. E. Transmission, "Appendices to the Technical Report on the events of 9 August 2019," 2019, Available: https://www.ofgem.gov.uk/system/files/docs/2019/09/eso_technical_report_-_appendices_-_final.pdf.

[3] A. Groundy. (2019). National Grid ESO claims world first approach to inertia, awarding £328m in contracts. Available: https://www.current-news.co.uk/news/national-grid-eso-claims-world-first-approach-to-inertia-awarding-328m-in-contracts

[4] V. Gevorgian, Y. Zhang, and E. Ela, "Investigating the impacts of wind generation participation in interconnection frequency response," IEEE transactions on Sustainable Energy, vol. 6, no. 3, pp. 1004-1012, 2015.

[5] A. Hoke and D. Maksimović, "Active power control of photovoltaic power systems," in Technologies for Sustainability (SusTech), 2013 1st IEEE Conference on, 2013, pp. 70-77: IEEE.

[6] E. Ela et al., Active Power Controls from Wind Power: Bridging the Gap. National Renewable Energy Laboratory, 2014.

[7] J. Aho et al., "A tutorial of wind turbine control for supporting grid frequency through active power control," in 2012 American Control Conference (ACC), 2012, pp. 3120-3131: IEEE.

[8] J. Morren, S. W. De Haan, W. L. Kling, and J. Ferreira, "Wind turbines emulating inertia and supporting primary frequency control," IEEE Transactions on power systems, vol. 21, no. 1, pp. 433-434, 2006.

[9] W. Hu, C. Su, J. Fang, Z. Chen, and Y. Hu, "Ancillary frequency control of direct drive full-scale converter based wind power plants," in PowerTech (POWERTECH), 2013 IEEE Grenoble, 2013, pp. 1-6: IEEE.

[10] E. Ela, V. Gevorgian, A. Tuohy, B. Kirby, M. Milligan, and M. O'Malley, "Market designs for the primary frequency response ancillary service—Part I: Motivation and design," Power Systems, IEEE Transactions on, vol. 29, no. 1, pp. 421-431, 2014.

[11] L. Wang, D. Chen, S. PTI, and E. Siemens, "Automatic generation control (AGC) dynamic simulation in PSS/E," Siemens PTI eNewsletter, no. 107, 2011.

[12] E. Ela and M. O'Malley, "Studying the variability and uncertainty impacts of variable generation at multiple timescales," IEEE Transactions on Power Systems, vol. 27, no. 3, pp. 1324-1333, 2012.

[13] H. Chavez, R. Baldick, and J. Matevosyan, "The Joint Adequacy of AGC and Primary Frequency Response in Single Balancing Authority Systems," Sustainable Energy, IEEE Transactions on, vol. PP, no. 99, pp. 1-8, 2015.

[14] V. Trovato, A. Bialecki, and A. Dallagi, "Unit commitment with inertia-dependent and multispeed allocation of frequency response services," IEEE Transactions on Power Systems, vol. 34, no. 2, pp. 1537-1548, 2018.

[15] E. Ela, V. Gevorgian, A. Tuohy, B. Kirby, M. Milligan, and M. O'Malley, "Market designs for the primary frequency response ancillary service—Part I: Motivation and design," IEEE Transactions on Power Systems, vol. 29, no. 1, pp. 421-431, 2014.

[16] W. Li, P. Du, and N. Lu, "Design of a new primary frequency control market for hosting frequency response reserve offers from both generators and loads," IEEE Transactions on Smart Grid, vol. 9, no. 5, pp. 4883-4892, 2017.

[17] X. Fang, J. Tan, H. Yuan, S. Yin, and J. Wang, “Providing Ancillary Services with Photovoltaic Generation in Multi-Timescale Grid Operation,” *2020 52nd North Am. Power Symp. NAPS 2020*, Apr. 2021.

[18] S. Yin, J. Wang, Y. Lin, X. Fang, J. Tan, and H. Yuan, “Practical Operations of Energy Storage Providing Ancillary Services: From Day-Ahead to Real-Time,” *2020 52nd North Am. Power Symp. NAPS 2020*, Apr. 2021.

[19] California ISO, “Flexible Ramping Product,” 2016.

[20] Q. Wang, W. Hongyu, T. Jin, B. M. Hodge, W. Li, and C. Luo, “Analyzing the impacts of increased wind power on generation Revenue Sufficiency,” in *IEEE Power and Energy Society General Meeting*, 2016, vol. 2016-Novem, pp. 1–5.

[21] B. Wang, A. Hoke, J. Tan, "Power System Network Reduction for PHIL Simulation," Kansas Power and Energy Conference, 2021.

[22] J. E. Price and J. Goodin, "Reduced network modeling of WECC as a market design prototype," 2011 IEEE Power and Energy Society General Meeting, Detroit, MI, USA, 2011, pp. 1-6, doi: 10.1109/PES.2011.6039476.

[23] H. Yuan, R. S. Biswas, J. Tan and Y. Zhang, "Developing a Reduced 240-Bus WECC Dynamic Model for Frequency Response Study of High Renewable Integration," 2020 IEEE/PES Transmission and Distribution Conference and Exposition (T&D), Chicago, IL, USA, 2020.

[24] S. Maslennikov, B. Wang, "Creation of simulated test cases for the oscillation source location contest," 2022 PES General Meeting, accepted.

[25] “Test Case Repository for High Renewable Study,” Mar. 2021. [Online] Available: https://www.nrel.gov/grid/test-case-repository.html

[26] J. Tan, B. Wang, X. Fang, H. Yuan, etc. , Development of a Reduced 240-Bus Western Electricity Coordinating Council (WECC) Test System and High IBR Penetration Scenarios, under construction.

[27] Y. Zhao, S. You, M. Mandich, L. Zhu, C. Zhang, H. Li, Y. Su, C. Zeng, Y. Zhao, Y. Liu, H. Jiang, H. Yuan, Y. Zhang, J. Tan, “Deep learning-based adaptive remedial action scheme with security margin for renewable-dominated power grids,” Energies, vol. 14, no. 20, 2021.

[28] J. Tan and Y. Zhang, "Coordinated Control Strategy of a Battery Energy Storage System to Support a Wind Power Plant Providing Multi-Timescale Frequency Ancillary Services," in IEEE Transactions on Sustainable Energy, vol. 8, no. 3, pp. 1140-1153, July 2017, doi: 10.1109/TSTE.2017.2663334.

[29] J. Tan, H. Yuan, Y. Zhang, etc., “A Multi-Timescale Framework to Study the Performance of High-Penetration of Renewables Providing Frequency Ancillary Services,” submitted to IEEE Trans on Sustainable Energy.

[30] B. Wang and J. Tan, in DC-AC Tool: Fully Automating the Acquisition of AC Power Flow Solution, NREL/TP-5D00-80100, 2022.

[31] “IEEE-NASPI Oscillation Source Location Contest,” https://www.naspi.org/node/890

[32] “MIDAS DC-AC Tool,” https://github.com/NREL/DC2AC.

[33] “PSSE Network Reduction,” https://github.com/NREL/PSSE_Network_Reduction

[34] R. W. Kenyon, A. Sajadi, A. Hoke, and B.-M. Hodge, “Open-Source PSCAD Grid-Following and Grid-Forming Inverters and A Benchmark for Zero-Inertia Power System Simulations,” in 2021 IEEE Kansas Power and Energy Conference (KPEC), Apr. 2021, pp. 1–6.

[35] R. W. Kenyon, B. Wang, A. Hoke, J. Tan, C. Antonio, and B.-M. Hodge, “Validation of Maui PSCAD Model: Motivation, Methodology, and Lessons Learned,” in 2020 52nd North American Power Symposium (NAPS), Apr. 2021, pp. 1–6.

[36] R. W. Kenyon, A. Hoke, J. Tan, and B. Hodge, “Grid-Following Inverters and Synchronous Condensers: A Grid-Forming Pair?,” in 2020 Clemson University Power Systems Conference (PSC), 2020, pp. 1–7.

[37] R. W. Kenyon, A. Sajadi, A. Hoke, and B.-M. Hodge, “Criticality of Inverter Controller Order in Power System Dynamic Studies – Case Study: Maui Island,” Accepted, 2022.

[38] J. Tan, X. Fang, H. Yuan, J. Wang, S. Yin, Y. Lin “MIDAS TOOL MANUAL_V2.0”. NREL Internal Report.

[39] X. Liu, X. Fang, J. Tan. “MIDAS GUI Manual” NREL Internal Report.

[40] R. W. Kenyon, B. Wang, A. Hoke, J. Tan, B. M. Hodge, "Comparison of Electromagnetic Transient and Phasor Dynamic Simulations: Implications for Inverter Dominated Systems," in preparation.

[41] A Hoke, P. Koralewicz, B. Wang, and R. W. Kenyon, Li Yu, Kelcie Kawamura, Jin Tan, “Stability of Inverter-based Transmission Systems: Power Hardware-in-the-Loop Experiments with a Megawatt-scale Grid-forming Inverter,” IEEE Electrification Magazine, to appear, 2022.

[42] J. T. Bin Wang, "DC-AC Tool: Fully Automating the Acquisition of the AC Power Flow Solution," National Renewable Energy Lab 2022.

[43] B. Wang, A. Hoke, J. Tan, “Power System Network Reduction for Power Hardware-in-the-Loop Simulation,” IEEE Kansas Power and Energy Conference, 2021

Appendix

6.1 Appendix A – 18-bus 4-areaTest System

6.2 Appendix B – Machine-learning based dynamic stability assessment.

Appendix A – 18-Bus Test System

A.1 System Layout

The four-area system given in GE PSLF is shown in Figure 1.

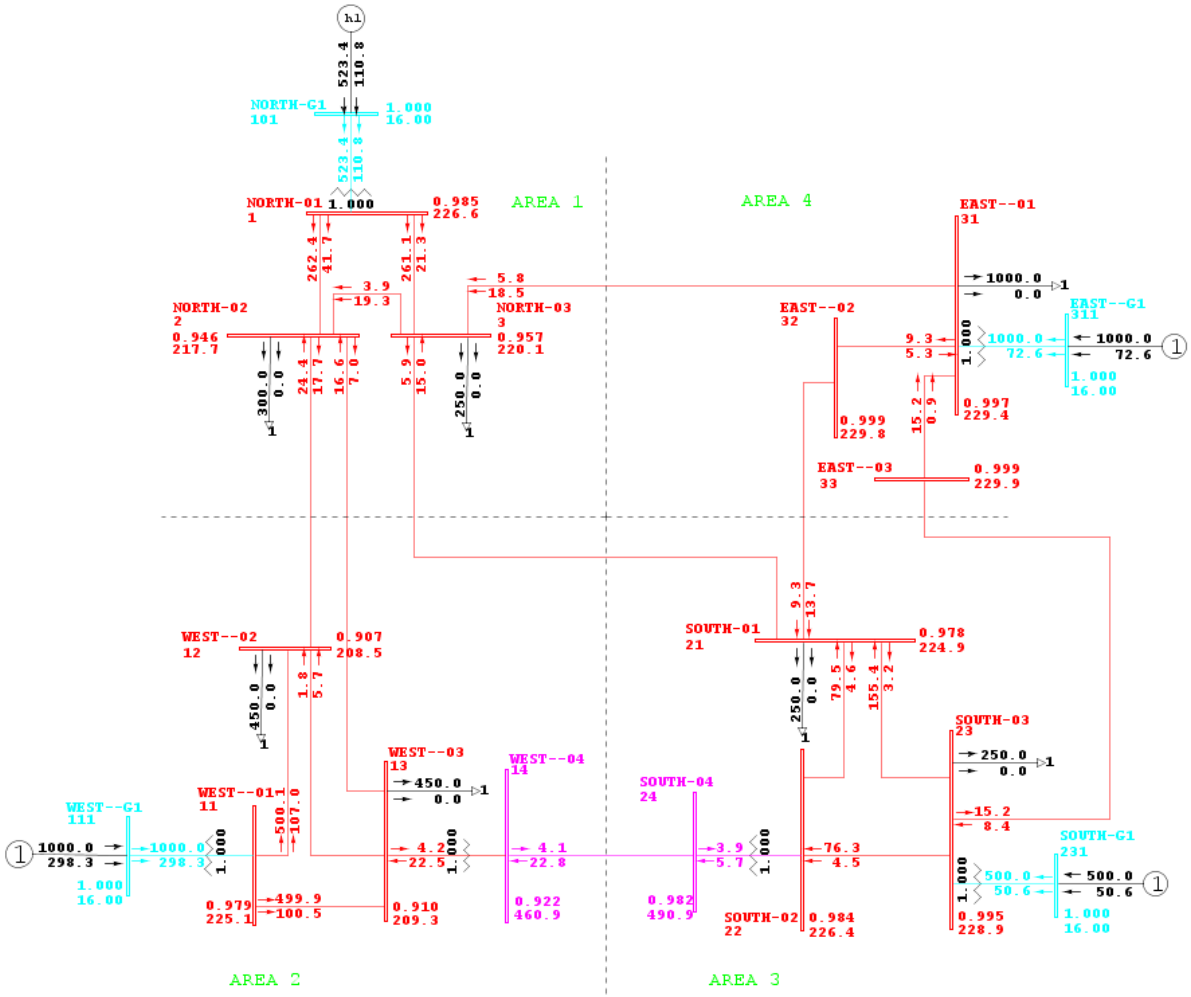

Figure 1. Four-area system

The voltage levels for the buses with the blue color, the red color and the purple color are 16 kV, 230 kV and 500 kV, respectively. Here, buses 101, 1 and 2 are used as examples to illustrate the meaning of the legends around the buses.

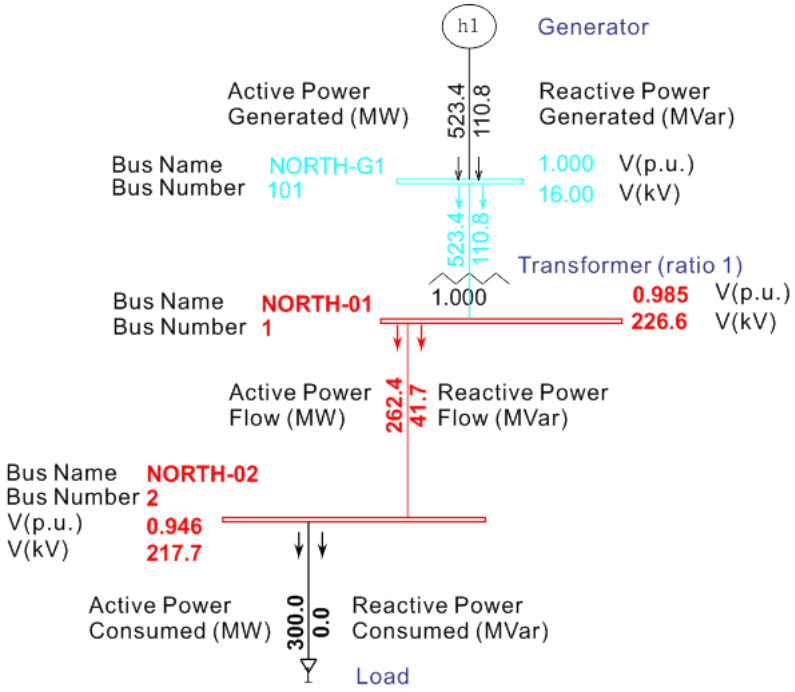

Figure 2. Illustration of the legends

A.2. Summary of the System

	Number
Areas	4
Buses	18
Lines	18
Transformers	6
Generators	4
Loads	7

A.3. System Data

The power base for the system is 100 MVA.

1) Bus Data

Bus No	Bus Name	Voltage Base (kV)	Bus Type	VSched (p.u.)	V (p.u.)	Angle (deg)	Vmax (p.u.)	Vmin (p.u.)	Area
1	NORTH-01	230	1	0.9897	0.9854	-5.08	1.0397	0.9397	1
2	NORTH-02	230	1	0.9586	0.9464	-12.91	1.0086	0.9086	1
3	NORTH-03	230	1	0.9675	0.957	-12.9	1.0175	0.9175	1
11	WEST--01	230	1	0.9795	0.9787	6.30	1.0295	0.9295	2
12	WEST--02	230	1	0.9097	0.9065	-9.35	0.9597	0.8597	2
13	WEST--03	230	1	0.9129	0.9099	-9.32	0.9629	0.8629	2
14	WEST--04	500	1	0.9241	0.9218	-9.62	0.9742	0.8741	2
21	SOUTH-01	230	1	0.9794	0.9776	-13.75	1.0294	0.9294	3
22	SOUTH-02	230	1	0.9854	0.9843	-11.35	1.0354	0.9354	3
23	SOUTH-03	230	1	0.9956	0.9951	-9.15	1.0456	0.9456	3
24	SOUTH-04	500	1	0.983	0.9818	-11.2	1.0330	0.9330	3
31	EAST--01	230	1	0.9977	0.9974	-11.38	1.0476	0.9477	4
32	EAST--02	230	1	0.9996	0.9992	-11.67	1.0496	0.9496	4
33	EAST--03	230	1	0.9998	0.9994	-10.95	1.0498	0.9498	4
101	NORTH-G1	16	0	1.0000	1.0000	0	1.0500	0.9500	1
111	WEST--G1	16	2	1.0000	1.0000	11.19	1.0500	0.9500	2
231	SOUTH-G1	16	2	1.0000	1.0000	-4.35	1.0500	0.9500	3
311	EAST--G1	16	2	1.0000	1.0000	-6.58	1.0500	0.9500	4

Bus No	Bus Name	Voltage Base (kV)	Bus Type	VSched (p.u.)	V (p.u.)	Angle (deg)	Vmax (p.u.)	Vmin (p.u.)	Area
35	EAST-05	230	1						3
351	EAST-BESS	25	1	1	1				3
352	EAST-DFIG1	25	2	1	1				3
353	EAST-DFIG2	25	2	1	1				3
354	EAST-DFIG3	25	2	1	1				3
355	EAST-DFIG4	25	2	1	1				3

Bus No: bus number
Bus Name: bus name
Voltage Base: the voltage base for the bus (kV)
Bus Type: 0 - slack bus (voltage magnitude and phase angle fixed
1 - load bus (PQ bus, unconstrained voltage phase angle and magnitude)
2 - generator bus (PV bus, voltage control within generator limits)
VSched: scheduled voltage magnitude (p.u.)
V: actual voltage magnitude (p.u.)
Angle: actual voltage phase angle (degree)
Vmax: voltage checking upper limit (p.u.)
Vmin: voltage checking lower limit (p.u.)
Area: area to which the bus belongs

2) Line Data

From Bus			To Bus			Resistance (p.u.)	Reactance (p.u.)	Susceptance (p.u.)	First Branch Rating (MVA)	Area
No	Name	V Base (kV)	No	Name	V Base (kV)					
1	NORTH-01	230	2	NORTH-02	230	0.01	0.05	0	600	1
1	NORTH-01	230	3	NORTH-03	230	0.01	0.05	0	600	1
2	NORTH-02	230	3	NORTH-03	230	0.01	0.05	0	600	1
2	NORTH-02	230	12	WEST--02	230	0.02	0.2	0.1	600	1
2	NORTH-02	230	13	WEST--03	230	0.03	0.3	0.15	600	1
3	NORTH-03	230	21	SOUTH-01	230	0.02	0.2	0.1	600	1
3	NORTH-03	230	31	EAST--01	230	0.05	0.5	0.25	600	1
11	WEST--01	230	12	WEST--02	230	0.01	0.05	0	600	2
11	WEST--01	230	13	WEST--03	230	0.01	0.05	0	600	2
12	WEST--02	230	13	WEST--03	230	0.01	0.05	0	600	2
14	WEST--04	500	24	SOUTH-04	500	0.06	0.4	0.2	2000	2
21	SOUTH-01	230	22	SOUTH-02	230	0.01	0.05	0	600	3
21	SOUTH-01	230	23	SOUTH-03	230	0.01	0.05	0	600	3
21	SOUTH-01	230	32	EAST--02	230	0.04	0.4	0.2	600	3
22	SOUTH-02	230	23	SOUTH-03	230	0.01	0.05	0	600	3
23	SOUTH-03	230	33	EAST--03	230	0.02	0.2	0.1	600	3
31	EAST--01	230	32	EAST--02	230	0.01	0.05	0	600	4
31	EAST--01	230	33	EAST--03	230	0.01	0.05	0	600	4

From Bus			To Bus			R1 (p.u.)	R0 (p.u.)	L1 (p.u.)	L0 (p.u.)	C1 (p.u.)	C0 (p.u.)	First Branch Rating (MVA)	Area
No	Name	V Base (kV)	No	Name	V Base (kV)								
31	EAST-01	230	35	EAST-05	230	0	0	0	0	0	0		3
351	EAST-BESS	25	352	EAST-DFIG1	25	0.1153	0.413	1.05e-3	3.32e-3	11.33e-9	5.01e-9		3
351	EAST-BESS	25	353	EAST-DFIG2	25	0.1153	0.413	1.05e-3	3.32e-3	11.33e-9	5.01e-9		3
351	EAST-BESS	25	354	EAST-DFIG2	25	0.1153	0.413	1.05e-3	3.32e-3	11.33e-9	5.01e-9		3
351	EAST-BESS	25	355	EAST-DFIG2	25	0.1153	0.413	1.05e-3	3.32e-3	11.33e-9	5.01e-9		3

R1: branch section positive sequence resistance (p.u.)
R0: branch section zero-sequence resistance (p.u.)
L1: branch section positive sequence inductance (p.u.)
L0: branch section zero-sequence inductance (p.u.)
C1: branch section positive sequence capacitance (p.u.)
C0: branch section zero-sequence capacitance (p.u.)

3) Transformer Data

From Bus			To Bus			Power Base (MVA)	Primary Winding Nominal V (kV)	Secondary Winding Nominal V (kV)	Tap Ratio	R (p.u.)	X (p.u.)	B (p.u.)	First Branch Rating (MVA)	Area
No	Name	V Base (kV)	No	Name	V Base (kV)									
1	NORTH-01	230	101	NORTH-G1	16	600	230	16	1	0	0.1	0	600	1
11	WEST--01	230	111	WEST--G1	16	1200	230	16	1	0	0.1	0	1200	2
13	WEST--03	230	14	WEST--04	500	100	230	500	1	0.01	0.05	0	100	2
22	SOUTH-02	230	24	SOUTH-04	500	100	230	500	1	0.01	0.05	0	100	3
23	SOUTH-03	230	231	SOUTH-G1	16	600	230	16	1	0	0.1	0	600	3
31	EAST--01	230	311	EAST--G1	16	1200	230	16	1	0	0.1	0	1200	4
35	EAST-05	230	351	EAST-BESS	25	500	230	25	1	0.0026	0.08	0		3

Power Base: transformer power base (MVA)

R: resistance primary to secondary (p.u. value on transformer bases)

X: reactance primary to secondary (p.u. value on transformer bases)

B: Magnetizing susceptance (p.u. value on transformer bases)

4) Generator Data

Bus			Control Mode	PGen (MW)	QGen (MVar)	Qmax (MVar)	Qmin (MVar)	Regulating Bus			VSched (p.u.)	V (p.u.)	Area
No	Name	V Base (kV)						No	Name	V Base (kV)			
101	NORTH-G1	16	0	523.4	110.8	999	-999	101	NORTH-G1	16	1	1	1
111	WEST--G1	16	0	1000	298.3	500	-500	111	WEST--G1	16	1	1	2
231	SOUTH-G1	16	0	500	50.6	250	-250	231	SOUTH-G1	16	1	1	3
311	EAST--G1	16	0	1000	72.6	500	-500	311	EAST--G1	16	1	1	4

Control Mode: 0 - voltage at the regulated bus is held constant within Q limits of generators specified by Qmax and Qmin

PGen: actual active power output of the generator (MW)

QGen: actual reactive power output of the generator (MVar)

Qmax: maximum reactive power output of the generator (MVar)

Qmin: minimum reactive power output of the generator (MVar)

Regulating Bus: the bus at which the voltage is regulated by the generator

VSched: generator scheduled voltage magnitude (p.u.)

V: generator actual voltage magnitude (p.u.)

Bus			Control Mode	Capacity (MW)	PGen$_0$ (MW)	QGen$_0$ (MVar)	Regulating Bus			VSched (p.u.)	V (p.u.)	Area
No	Name	V Base (kV)					No	Name	V Base (kV)			
352	DFIG	25	1	135	40	1.95	351	DFIG	25	1	1	3
353	DFIG	25	1	135	40	1.95	352	DFIG	25	1	1	3
354	DFIG	25	1	135	40	1.95	353	DFIG	25	1	1	3
355	DFIG	25	1	135	40	1.95	354	DFIG	25	1	1	3
351	BESS	25	2	4	0	0						3

Control Mode: 1- Voltage regulation; 2-Reactive power regulation and Q=Qset.
PGen0: Initial actual active power output of the generator (In this case, wind speed=9m/s).
QGen0: Initial reactive power output of the generator.

5) Load Data

Bus			Constant Power Load		Constant Current Load		Constant Admittance Load		Load Type	Area
No	Name	V Base (kV)	PLoad (MW)	QLoad (MVar)	IPLod (MW)	IQLod (MVar)	GLoad (MW)	BLoad (MVar)		
2	NORTH-02	230	0	0	0	0	334.93	0	0	1
3	NORTH-03	230	0	0	0	0	272.96	0	0	1
12	WEST--02	230	0	0	0	0	547.56	0	0	2
13	WEST--03	230	0	0	0	0	543.53	0	0	2
21	SOUTH-01	230	0	0	0	0	261.58	0	0	3
23	SOUTH-03	230	0	0	0	0	252.49	0	0	3
31	EAST--01	230	0	0	0	0	1005.15	0	0	4

Each load has three components: a constant power component, a constant current component and a constant admittance component.

PLoad: active power consumed by the constant power component (MW)

QLoad: reactive power consumed by the constant power component (MVar)

IPLod: active power consumed by the constant current component at 1 p.u. voltage (MW)

IQLod: reactive power consumed by the constant current component at 1 p.u. voltage (MVar)

GLoad: active power consumed by the constant admittance component at 1 p.u. voltage (MW)

BLoad: reactive power consumed by the constant admittance component at 1 p.u. voltage (MVar)

Load Type: 1 - non-conforming (fixed)
0 - conforming (scalable)

Appendix B: Machine-learning based dynamic stability assessment model

FINAL REPROT: MIDAS-SOLAR

JUNE 2022

Table of Contents

I. Literature Review on Using Artificial Intelligence for Stability Assessment..... 3

A. AI-based Transient Stability Assessment 4

B. AI-based Frequency Stability Assessment 8

C. AI-based Small-signal Stability Assessment 8

D. Summary 9

II. An Artificial Intelligence Tool for Frequency, Transient, and Small-signal Stability Assessment 10

A. Framework and Methods of AI-Based System Stability Assessments 10

B. Test systems for AI based stability assessment 13

1) 18-bus test system 13

2) 240-bus reduced WECC system 13

III. Artificial Intelligence Based Transient Stability Assessment 15

A. AI based transient stability assessment on the 240-bus reduced WECC system 15

B. AI based transient stability assessment on the 18-bus System 20

C. Data-driven Stability Assessment Tool Improvement Considering Topology Change 22

D. Summary 26

IV. Artificial Intelligence Based Frequency Stability Assessment 27

A. AI-based frequency stability prediction on the 240-bus reduced WECC system 27

B. Clustering-based AI training dataset reduction on the 240-bus reduced WECC system 29

C. Data-driven frequency stability on the 18-bus system 33

D. Summary 35

V. Artificial Intelligence Based Small Signal Stability Assessment 36

A. AI-based stability assessment on the 240-bus system. 36

1) Oscillation Mode Study and Target Oscillation Mode 36

2) AI-based Small Signal Stability prediction for the 240-bus reduced WECC system 39

B. Stability assessment on the 18-bus system. 40

C. Summary 43

VI. AI-based WECC-1 Remedial Action Scheme (RAS) Improvement 44

A. WECC-1 RAS-1 Introduction 44

B. AI Based RAS 44

1) Deep Learning Neural Network Structure for Adaptive RAS 47

2) Customized Loss Function 48

3) Evaluation Metrics 50

4) Prediction Performance Comparison Between Proposed Adaptive Remedial Action Scheme (RAS) and Conventional RAS 50

5) Layer Number and Node Number Selection 53

6) Regularization Hyper Parameter Tuning 54

C. Summary 55

I. Literature Review on Using Artificial Intelligence for Stability Assessment

Power grid stability consists of transient stability, frequency stability, small signal stability, and voltage stability (Figure 1) [1-2]. Fast assessment of system stability is useful in many places, including day-ahead scheduling, real-time operation, and long-term planning. Traditional methods for power system stability assessment are based on time-domain simulation, which heavily relies on the availability of real-time power system dynamic models and requires significant simulation computational resources [3-7].

Beside model simulation, another category of methods for stability assessment is data-driven methods, as shown in Figure 2. Data-driven methods for stability assessment consists of measurement-based methods and artificial-intelligence-based methods. Measurement-based methods use measurement data to develop simplified models (such as transfer functions or reduced models) for stability assessment, which require less computation time compared with time-domain simulation based on detailed models [10-13]. However, the development of measurement-based simplified models is a non-trivial task [16]. In contrast, artificial-intelligence-based stability assessment is data-driven and not directly based on physical principles [17-19]. After trained using simulation or measurement data, artificial intelligence models can perform stability assessment based on system feature inputs.

A number of studies have already tried applying artificial intelligence into power system stability assessment [16-20]. This chapter provides a literature review on existing studies. Most existing machine learning based approaches can only assess one type of stability. Input features are usually selected based on trial and error on a specific machine learning model. This work proposed an artificial intelligence tool using the same set of input data to assess power system transient stability, small signal stability, and frequency stability, simultaneously. The accuracy and efficiency of the proposed approach in stability assessment is verified on an 18-bus system.

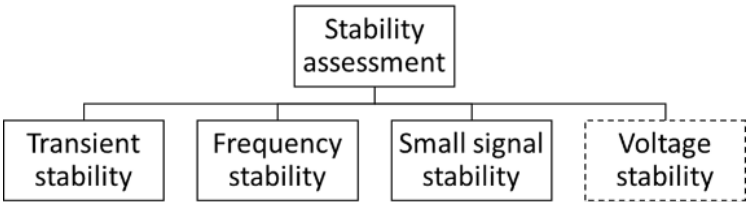

Figure 1. Stability topics in power grids

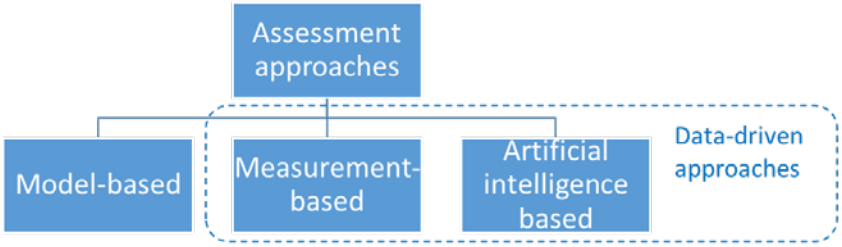

Figure 2. Power grid stability assessment approach categorization

A. AI-based Transient Stability Assessment

Transient stability is the power system ability to maintain synchronism when subjected to a severe disturbance, such as a short circuit on a transmission line [23]. Existing literature that applies artificial intelligence to assess transient stability mainly uses three categories of methods: neural network, support vector machine [24-26], and decision tree [1], as summarized In Table 1, Table 2, and Table 3, respectively. Most of these studies used the New England 10-machine system as the test system. These methods showed high accuracy in classifying stable and unstable cases: all methods achieved higher than 96% accuracy and some even reached 100% in accuracy. Additionally, a few studies tried considering the change of topology in artificial intelligence models [2,29].

A summary of these methods considering topologies is shown in Table 4. The most commonly used methods include: using the current topology to build the dynamic model and then generate the training dataset [2]; and generating a training dataset that covers all possible system topologies before training the artificial intelligence model [29]. Several other artificial intelligence methods other than the three categories in transient stability assessment are listed in Table 5. These methods achieved similar accuracy levels in transient stability assessment.

Table 1. Neural Network (NN) Based Methods for Transient Stability Assessment

Ref	Model	Test System	Samples	Training	Testing	# Features	Accuracy (%)
[2]	Extreme learning machines (ELM)	IEEE 50-bus system	6,345	5,076	1,269	50	100
[9]	Extreme learning machine (ELM) + trajectory fitting (TF)	New England 10-machine	10,000	N/A	N/A	100 (269)	99.1
[15]	Extreme learning machine (ELM) + a decision-making process	New England 10-machine	4,000	2,000	2,000	N/A	97.92 – 98.38
[21]	An array of neural networks (NN) + an interpreter	PSB4 system + New England 10-machine	248/300	208/250	40/50	N/A	99.85/100
[22]	Probabilistic neural network (PNN)	IEEE 68-bus, 16-generator system + three wind generation units	190 operation conditions and three-phase faults	N/A	N/A	244, 150,100,50	> 99
[27]	Recurrent neural network (RNN) + long short-term memory network (LSTM)	New England 10-machine	5,000	3,750	1,250	N/A	100
[29]	Long-short Term Memory (LSTM) ensemble neural network + decision machine	New England 10-machine	4,058	3,044	1,014	N/A	100
[31]	Extreme learning machine (ELM) + Boosting learning	New England 10-machine	68,640	N/A	N/A	50 (183)	100
[32]	Extreme learning machine(ELM)	New England 10-machine	1,240	864	376	62	98
[34]	Convolutional neural network (CNN) + stacked auto-encoders (SAEs)	New England 10-machine	4,014	2,689	1,325	22	96.78 – 98.68
[35]	Neural network (NN) + incremental learning	Shandong power system- 362 buses	945	540	405	N/A	96.6

Table 2. Support Vector Machine (SVM) Based Methods for Transient Stability Assessment

Ref	Model	Test System	Samples	Training	Testing	# Features	Accuracy (%)
[36]	SVM + transient energy function (TEF)	New England 10-machine	700	500	200	36, 18	97.5 – 100
[39]	Ball vector machine (BVM)	New England 10-machine	5,500	4,000	1,500	200	97.1
[41]	SVM	Priba system: 2484 buses	1,242	994	248	224, 150, 100, 50	94.4
[26]	SVM + DT + rotor angles trajectory clustering	New England 10-machine and IEEE 145-bus	3,672	1,099	2,573	19	90.74 – 98.15 94.75 – 95.41
[42]	SVM, Naïve Bayes, decision tree	IEEE 14-bus	8000	N/A	N/A	23	88.2 – 98.8
[43]	SVM + Cost-sensitive ensemble learning classifier	New England 10-machine	4,290	4,000	290	23	96.4 – 99.4
[44]	Least Square Support Vector Machine (LS-SVM)	New England 10-machine	6,600	4,620	1,980	39	100
[45]	Reformed support vector machines + sequential minimal optimization (SMO)	New England 10-machine	20,000	16,000	4,000	15	96.9
[46]	Fuzzy C-means clustering algorithm + SVM	IEEE 39-bus system	726	556	170	10	100

Table 3. Decision Tree (DT) Based Methods for Transient Stability Assessment

Ref	**Model**	**Test System**	**Samples**	**Training**	**Testing**	**# Features**	**Accuracy (%)**
[1]	Decision tree (DT) + regression tree (RT)	Salt River Project (SRP) power system	41,412	33,130	82,82	N/A	99.13
[8]	Weighted random forest (WRF)	New England 10-machine	2,000	1,300	700	263	98.79
[14]	Random forest (RF)	New England 10-machine	2,000	1,300	700	45	99.1
[20]	Decision tree (DT)	9-bus dynamic network and 1,696-bus Iran national grid	513/1,080	N/A	N/A	5	79.92 – 100 94.91 – 99.91

Table 4. Literature Considering Topology Change in Artificial Intelligence Based Transient Stability Assessment

Ref	**Method to consider topology change**
[2]	The network is trained based on the current system topology and the loading conditions
[29]	Small-height DTs are periodically updated by incorporating the possible changes of the system topology

Table 5. Other Artificial Intelligence Based Methods for Transient Stability Assessment

Ref	Model	Test System	Samples	Training	Testing	# Features	Accuracy (%)
[28]	Deep belief network (DBN)	A real regional power system in China, consisting of 1300 buses, 3215 transmission lines	10,000	8,330	1,670	1,762	98.02
[30]	Least Absolute Selection and Shrinkage Operator (LASSO)	A practical 470-bus system	1,199	800	399	939	99.75
[33]	Type-2 fuzzy neural network	New England 10-machine	2,000	1,500	500	56	97.51 – 98.31

B. AI-based Frequency Stability Assessment

According to the definition from IEEE and CIGRE, frequency stability refers to the ability of a power system to maintain a steady frequency following a severe system upset resulting in an imbalance between generation and load [23]. Frequency instability occurs in the form of sustained frequency swings or large frequency deviations that eventually lead to tripping of generating units and/or loads, and system losing stability [38]. However, very few studies focused on frequency stability assessment using AI. In [31] (Table 6), an artificial neural network and power flow information were used to predict the frequency stability. The accuracy reaches 97.5%.

Table 6. Artificial Intelligence Based Frequency Stability Assessment

Ref	Model	Test System	Samples	Training	Testing	# Features	Accuracy (%)
[31]	Single-hidden layer feedforward network (SLFN)	IEEE 14-Bus System; New England 39-bus system	600	480	120	N/A	97.5%

C. AI-based Small-signal Stability Assessment

Small-disturbance (or small-signal) rotor angle stability is concerned with the ability of the power system to maintain synchronism under small disturbances [23]. The disturbances in the small signal stability domain are considered to be sufficiently small, so that stability analysis can be performed based on a linearized representation of the system. Reference [37] in Table 7 used neural network to study the small-signal stability of a single-machine infinite-bus system under different power output and power factor conditions, as well as power system stabilizer settings. Reference [40] used a decision tree to predict the eigenvalue region of critical modes. These studies also reached satisfactory (higher than 90%) accuracy in small signal stability assessment.

Table 7. Artificial Intelligence Based Small Signal Stability Assessment

Ref	Model	Test System	Samples	Training	Testing	# Features	Accuracy (%)
[37]	Artificial neural network	Single machine infinite bus system	N/A	N/A	N/A	4	~90%
[40]	Decision tree	PST 16-machine test system	2,500	N/A	N/A	252	99.77%

D. Summary

In general, it can be seen that most AI-based stability assessment approaches achieved high accuracy already. Overall, neural network has the highest accuracy. decision tree and SVM have slightly lower accuracy (Figure 3). However, in existing literature, most machine learning approaches focus on one type of stability and select input features based on trial and error on a specific machine learning model. Few studies can use the same set of input data to assess the system frequency, transient, and small signal stability simultaneously.

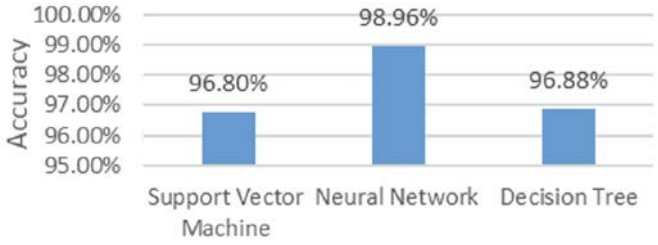

Figure 3. Average accuracy comparison of different AI methods

Challenges in using AI for stability assessment identified in this literature review include:

1. Most existing machine learning based approaches can only assess one type of stability. The inputs of machine learning are selected based on trial and error using a specific machine learning model on a specific system.
2. Existing machine learning models don't have datasets from realistic systems for validation. Their accuracy in practical application is not guaranteed, limiting their applications in the real world.
3. Existing machine learning models need a large amount of training data to reach high enough accuracy. However, these data are not always available due to computational resource constraints.

II. An Artificial Intelligence Tool for Frequency, Transient, and Small-signal Stability Assessment

A. Framework and Methods of AI-Based System Stability Assessments

Machine learning-based DSA can help determine when it is necessary to trigger a dynamic simulation; it can bridge the gap between a short-term full dynamic simulation and long-term scheduling simulation. The framework of this method is illustrated in Figure 4.

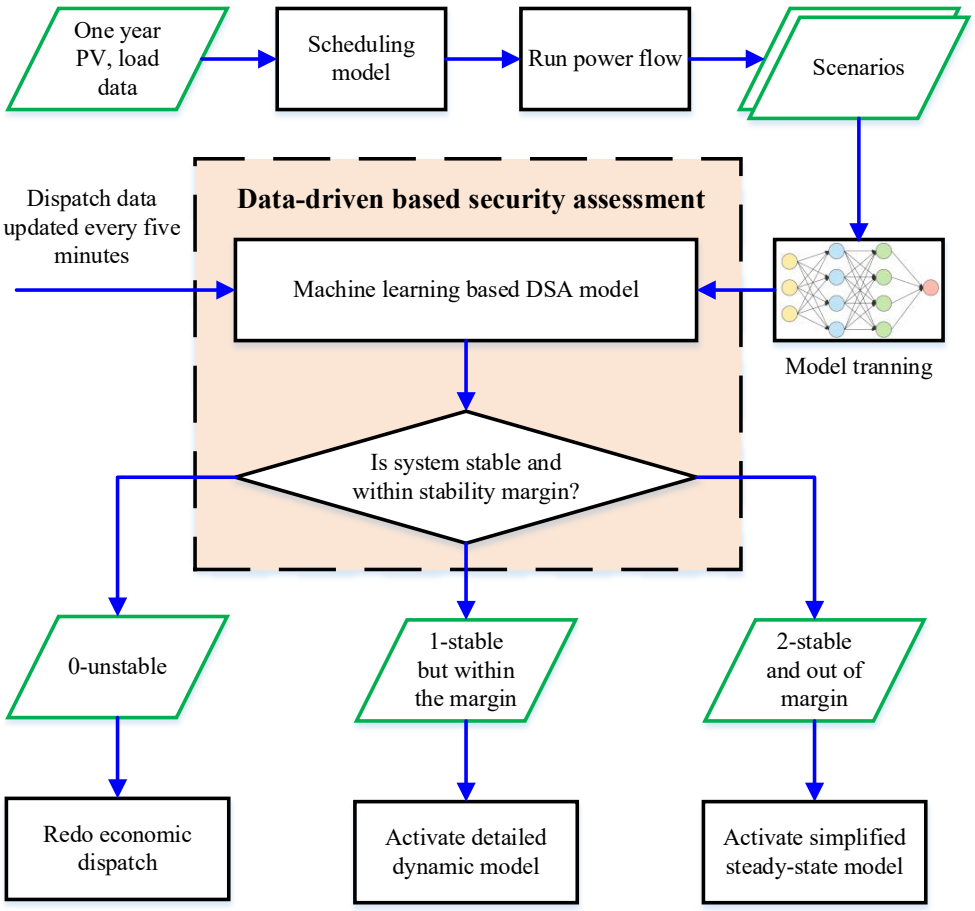

Figure 4. Framework of machine learning-based DSA

First, dispatch data from the scheduling model are used to run AC power flow. The scenarios for the whole year are obtained; these will be used for the machine learning model training. After that, the machine learning model can be used to predict the stability margin for a specific updated scenario. If the estimated stability margin indicates an unstable system, a command signal will be sent to the scheduling model to generate new dispatch data. If the system is stable and the stability margin is large enough, the simplified steady-state model will be activated for simulation. If the system is stable but within the stability margin, a detailed dynamic model is required for full dynamic simulation.

Figure 5 shows the detailed DSA flowchart based on the machine learning approach proposed in this study. In general, the DSA process includes three steps:

- Step 1: Extract informative features relevant to the system stability metrics from the load dispatch.
- Step 2: The extracted features are used to train the machine learning model to learn the underlying relationship between the informative features and the system stability metrics. The multivariate random forest regression (MRFR) and neural network models are used for the machine learning tool in this study.
- Step 3: The trained MRFR or neural network model is further implemented to estimate the system stability metrics using the load dispatch.

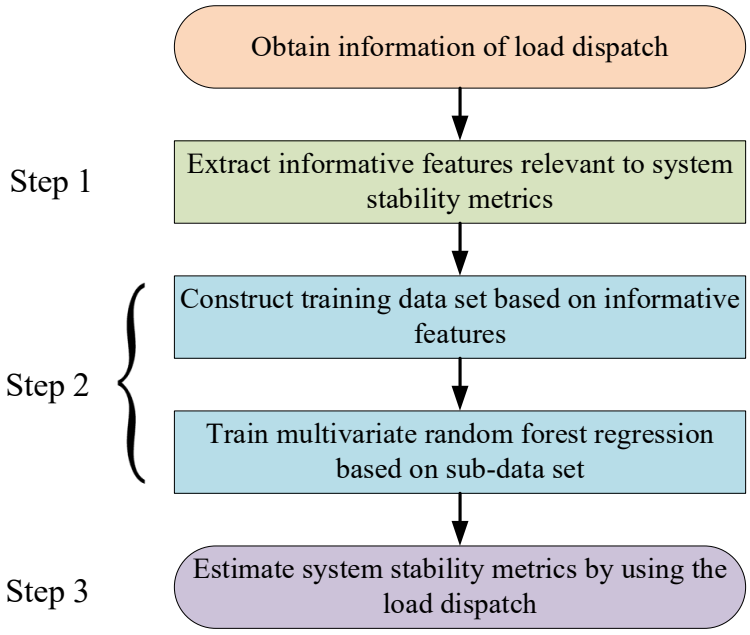

Figure 5. Flowchart of machine learning-based DSA (using MRFR as an example)

Since neural network is a commonly used machine learning model, here, we give a brief introduction about the other model used in this study: the MRFR model.

The MRFR is an ensemble of decision trees trained by bootstrap sampling and random feature selection. It aims to build a large collection of regression trees and average the output of each tree to reduce the variance of the prediction results and boost the performance of the final model. Figure 6 shows a diagram of the MRFR algorithm. Considering a training data set $\mathbf{X} = [X_1, X_2 \dots X_n]$ and the corresponding response $\mathbf{Y} = [Y_1, Y_2 \dots Y_n]$, MRFR first uses bootstrap to draw a set of samples with size m from the training data set. Then it establishes a regression Tree-i based on these bootstrapped data. The following steps are recursively repeated for each terminal node of the tree, until the minimum node size is attained.

1) Randomly select D dimension features of each bootstrapped sample in the training data set.

2) Split the parent node into two children nodes based on the information gain ratio criterion.

This iterative procedure is repeated for k times, and the output of the forest is the average of the predictions from each regression tree, as shown in (1).

$$\hat{Y} = \frac{1}{k}\sum_{i=1}^{k}\hat{Y}_i(\mathrm{X}) \tag{1}$$

Besides neural network, MRFR is used as the other machine learning model in this study because of its ease of implementation, high robustness to the input data, and capability to avoid overfitting the problem during the training process.

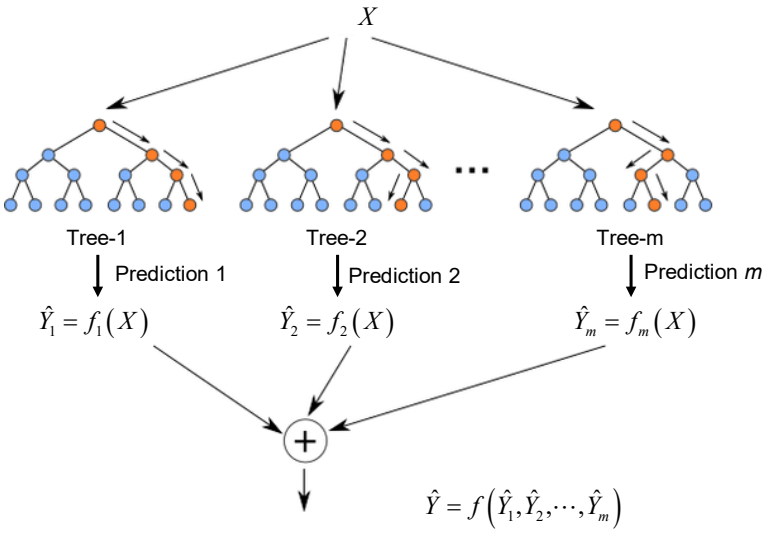

Figure 6. Diagram of multivariate random forest algorithm

In this study, the input of the DSA machine learning tool is the dispatch data updated every 5 minutes. Its outputs are system stability metrics, including critical clearing time, frequency nadir, and damping ratio of oscillation modes. A summary of inputs, outputs, data generation, and assessment approaches for three stability issues are show in Table 8.

Table 8. Summary of Inputs, Outputs, Data Generation, and Assessment Approaches for Three Stability Issues

Stability Problem	Input	Output	Contingency	Assessment Approach
Frequency	Generation dispatch results	Frequency nadir for the RCC contingency	Generation trip	• Generate a series of cases with different dispatch and inertia levels. • Evaluate frequency response using dynamic simulation.
Transient	Generation dispatch results, transmission network	Transient stability margin	3-phase fault on transmission line	• Generate a series of cases with different unit commitment and dispatch results.

Stability Problem	Input	Output	Contingency	Assessment Approach
				• Evaluate transient stability using Standard TPL-001-4 and dynamic simulation.
Small-Signal	Generation dispatch results, transmission network	Small-signal stability margin	N/A	• Generate a series of cases with different unit commitment and dispatch results. • Evaluate small-signal stability using small-signal analysis and dynamic simulation.

The stability assessment approach is implemented in two systems: the 18-bus test system and the 240-bus reduced WECC system.

B. Test systems for AI based stability assessment

1) 18-bus test system

The 1)18-bus test system has four areas, each with one conventional generator. One additional PV power plant is in the east area, as shown in Figure 7.

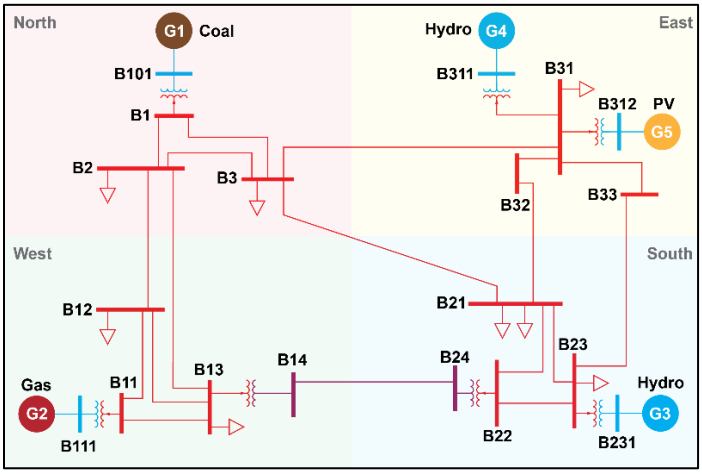

Figure 7. 18-bus test system

The NREL team provided load and generation data for the 18-bus system over a 24-hour period. Although individual load and machine data was given for every 4 seconds of the 24-hour period, saved cases were only generated for every 5 minutes. Therefore, 288 PSS/E saved cases were created. The developed saved cases were used in frequency, transient, and small-signal analysis. A Python script was used to extract generation and load data from input files, scale each machine's and load's real power, and save the results in individual PSS/E saved case files for each 5-minute period.

2) 240-bus reduced WECC system

The 240-bus system model developed by NREL is a reduced model of the WECC system. The system model has one year dispatch data obtained from unit commitment and optimal power flow. The reduced 240-bus WECC model reflects the generation resource

mix of the WECC system as of 2018. This reduced WECC system has 8,784 scenarios. Each of them represents a power flow snapshot of every hour in one year. Moreover, the developed dynamic model is validated against field frequency events measured by FNET/GridEye and preserves the dominant inter-area oscillation mode in WECC. Figure 8 shows the system overall topology. Figure 9 shows the total generation and renewable generation profiles of the system in one year. Its maximum instantaneous renewable penetration is around 30%. The system peak load is in summer, when air conditioner load reaches its maximum value.

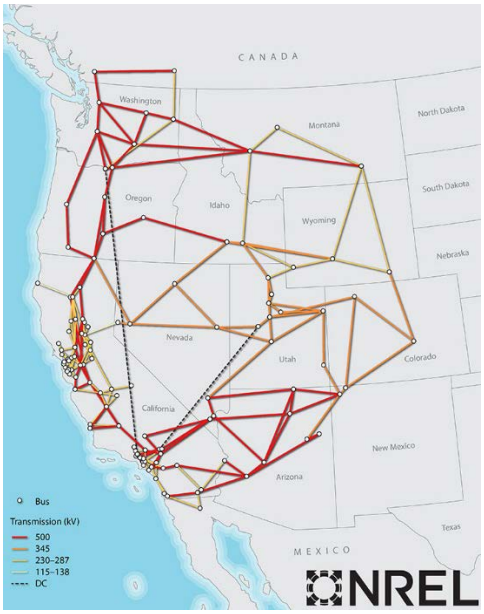

Figure 8. 240-bus reduced WECC system topology

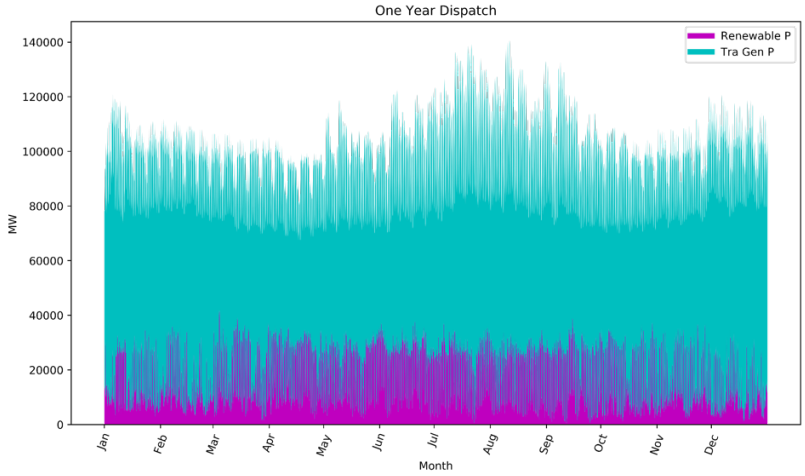

Figure 9. Total generation and renewable generation profiles

III. Artificial Intelligence Based Transient Stability Assessment

A. AI based transient stability assessment on the 240-bus reduced WECC system

This work studied the transient (angle) stability prediction. Transient stability is the power system ability to maintain synchronism when subjected to a severe disturbance, such as a short circuit on a transmission line. The maximum allowable value of the fault-clearing time for the system to remain stable are known as critical clearing time (CCT). A larger CCT value generally indicates higher angle stability.

In stability assessment of practical large systems, some small generators may lose synchronism and be tripped by out-of-step relays, without causing system-level stability issues. Therefore, in this study, the system's transient angle stability is defined as the relative rotor angles of all large generators (e.g. units with a capacity larger than 1,000 MVA for the reduced 240-bus system) do not change more than 180 degrees referring to pre-fault relative rotor angles at any time.

Generator i's relative rotor angle is defined as:

$$\delta_i(t) = \Delta_i(t) - Med\{\Delta(t)\} \quad (1)$$

where:

$\delta_i(t)$ is generator *i*'s relative rotor angle (using the system median rotor angle of all large generators as the reference) at time *t*;

$\Delta_i(t)$ is generator *i*'s rotor angle;

$Med\{\Delta(t)\}$ is the median rotor angle of all large generators at time *t*.

The generator is deemed as lost synchronization if:

$$abs\{\delta_x(t_{pre-fault}) - \delta_x(t_{after-fault})\} > 180$$

where $t_{pre-fault}$ is the time right before the fault; $t_{after-fault}$ is with several seconds (here, 2 seconds is used) after the fault.

To find the critical clearing time, we apply a binary search algorithm with 1ms resolution. The binary search algorithm's time complexity is $O(\log n)$, which can efficiently find the CCT value. For example, in our study, for a maximum 2,000ms fault lasting time, the time complexity is $\log_2 2000$ (or around 10.97). Therefore, 11 PSS/E simulations are enough to find the critical clearing time with an 1ms resolution if it is located within the 0-2 second range. Table 9 is an example of calculating a CCT value. Figure 10 shows two cases with different fault time duration: one stable case and the other unstable case.

Table 9. An Example of CCT Simulation Steps in PSS/E

Simulation steps	Fault lasting time (ms)	Transient Stability Status
1st	1,000	Unstable
2nd	500	Unstable
3rd	250	Unstable
4th	125	Stable
5th	188	Stable
6th	219	Stable
7th	234	Unstable
8th	227	Stable
9th	231	Stable
10th	233	Unstable
11th	232	Stable

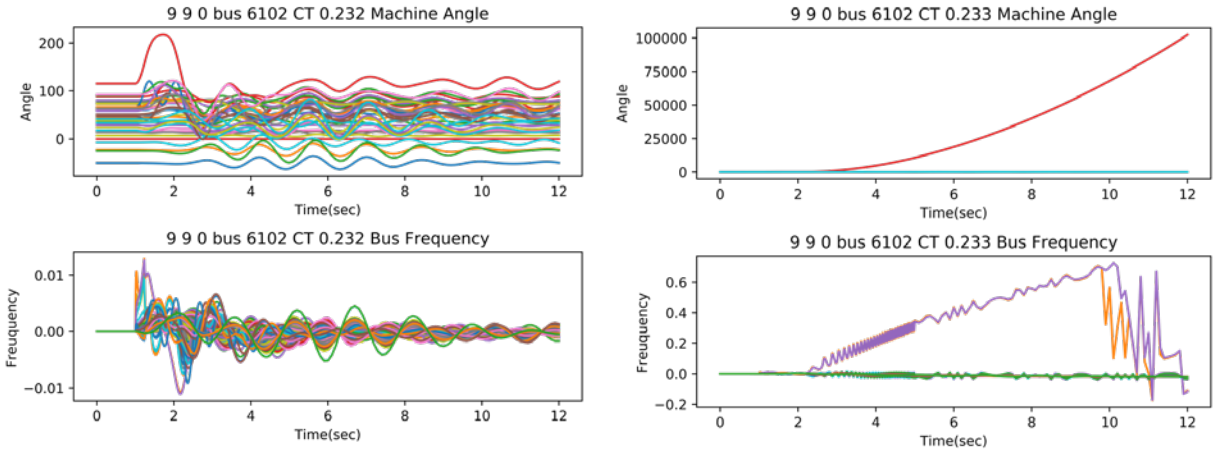

(a) Clear time is 232ms (stable) (b) Clearing time is 233ms (unstable)

Figure 10. Clearing time and system angle stability of the 240-bus reduced WECC system

In the 8,784 power flow scenarios, some cases have small signal stability issues. These cases bring some difficulties in transient angle stability assessment. For example, as shown in Figure 11, a small fault at 1.0 second does not cause the system to lose synchronism at the beginning. However, the system suffers from small-signal instability and becomes unstable after several seconds.

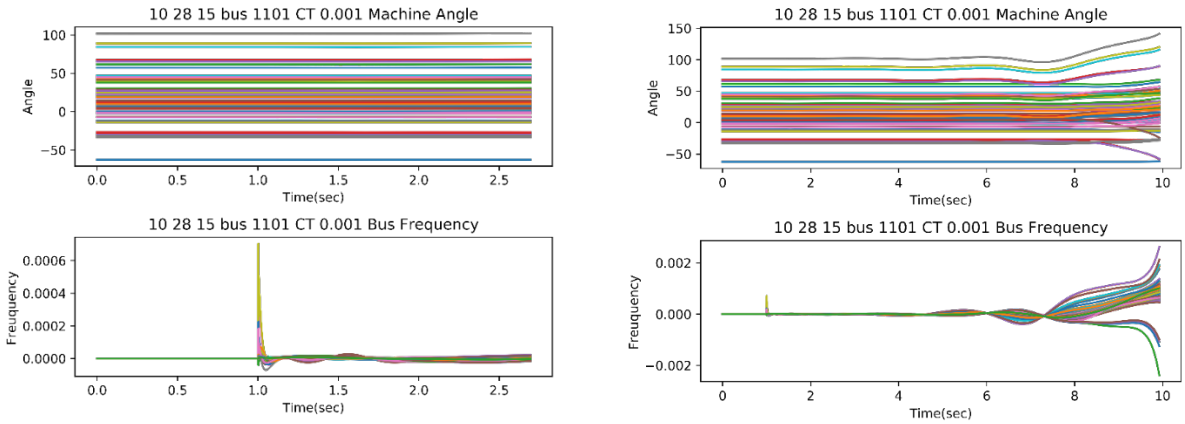

(6) 0-2.5 second 0-20 second

Figure 11. Angle and frequency profiles after a small disturbance (0.001s fault duration)

Since the small-signal instability will cause the system instability, it will influence the CCT value calculation. To provide a clean transient angle stability prediction problem in this study, we filtered out around 2,000 cases with small-signal instability issues, which will be used in the future small-signal stability prediction study. In these small-signal-unstable cases, generator rotor angle oscillations will grow or are poorly damped after a small disturbance. The criteria below are used to filter out these cases.

1. A small disturbance (a short-duration fault) is applied to the system at 1.0 second. The maximum oscillation magnitude at the first two seconds (1.0-3.0 second) after the disturbance is denoted as M_{t1}.
2. The simulation was continued to 20 seconds. The magnitude of the largest oscillation between 18.0-20.0 seconds is denoted as M_{t2}.
3. If $M_{t2} > 30\% M_{t1}$, the oscillation is considered a poorly damped oscillation and this case is considered as a small-signal unstable case and removed from the CCT prediction dataset.

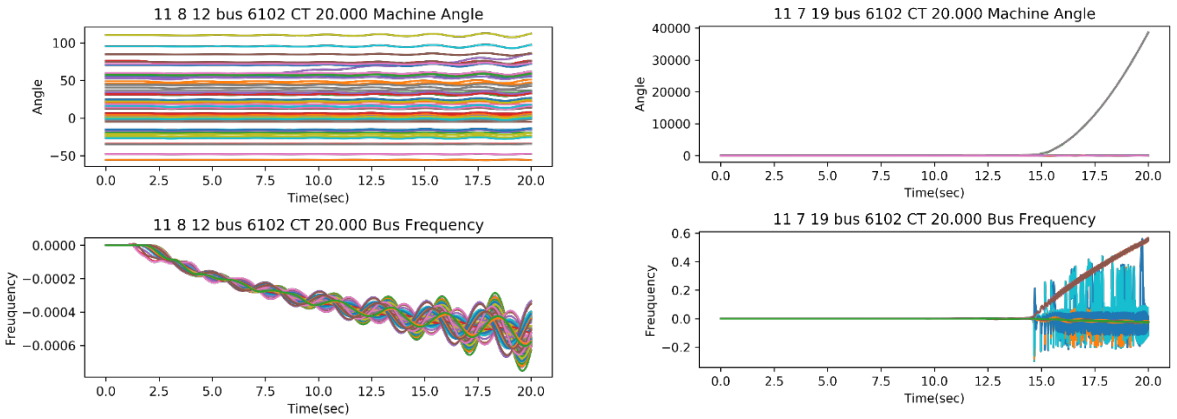

(a) Case 1 (b) Case 2

Figure 12. Two exemplar cases that are small-signal unstable

After removing these cases, the distribution of CCT values of Bus 1002 in the 240-bus system is shown in Figure 13. (Bus 1002 was selected because of lower CCT values compared with other buses.) It can be seen that the CCT values in summer peak hours are obviously lower. This is probably because of the higher loading levels of generators during summer peak hours.

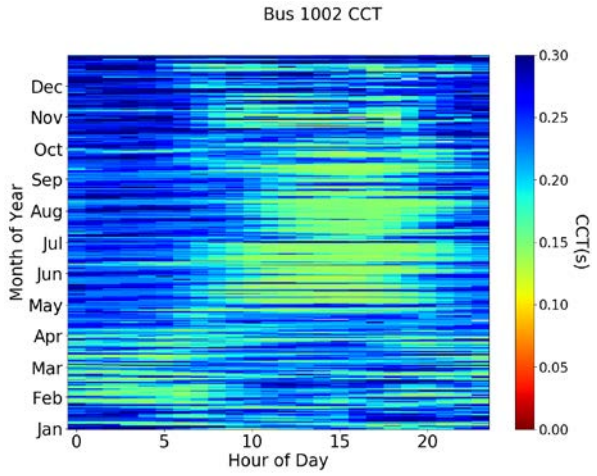

Figure 13. Distribution of the CCT values in one year

We applied neural network to predict CCT values of the 240-bus reduced WECC system. The input and output data information are given in Table 10. The dataset is divided into two subsets: 80% data are used for training (68%) and validation (12%); the rest 20% data are used for testing.

Table 10. Data Entries for CCT Prediction

Input/Output	Data	Number of Data Entries
Input	Total generation	1
	Total load real power	1
	Total system inertia	1
	Generator power output	146 (number of generators)
	Load power	139 (number of loads)
	Generator's inertia contribution	146 (number of generators)
Output	CCT	1

The CCT prediction performance and error distribution are shown in Figure 14. The Mean Absolute Error (MAE) of all prediction points is 0.00607s, which is around 4% of the average CCT value. The distribution of the error is almost symmetric to the Y axis. This indicates a desired feature that errors have a close-to-zero expectation. In addition, it can be noticed that the CCT prediction error is smaller when the CCT value is smaller, which is also a preferable feature since scenarios with low CCT values are more important for operators.

Figure 15 shows the CCT prediction performance of the four selected days. It is noted that although the CCT values change dramatically with the power flow within one day, the machine learning tool can assist real-time fast stability assessment by predicting the angle stability margin accurately. It can also verify the observation that the prediction errors are smaller for smaller CCT values.

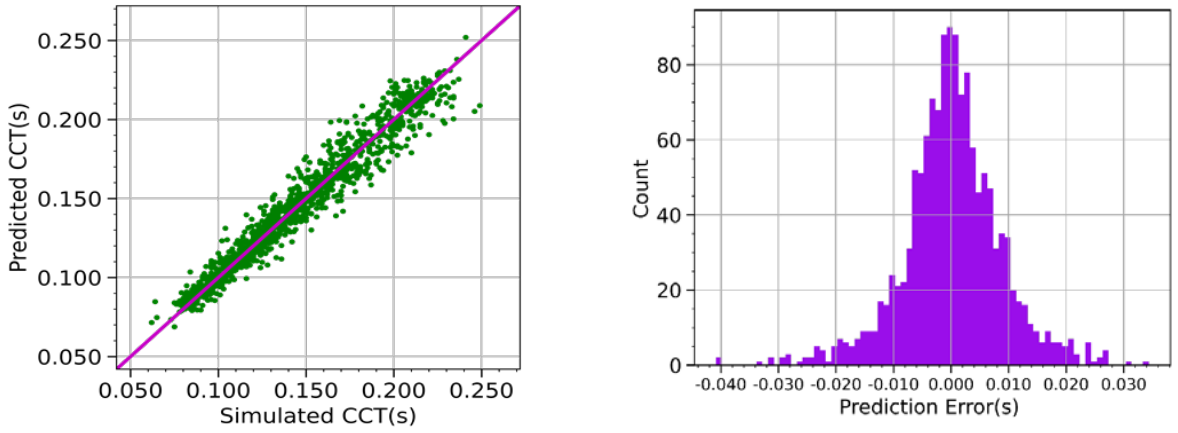

(a) CCT prediction results for multiple days

(b) CCT prediction error

Figure 14. CCT prediction performance and error distribution

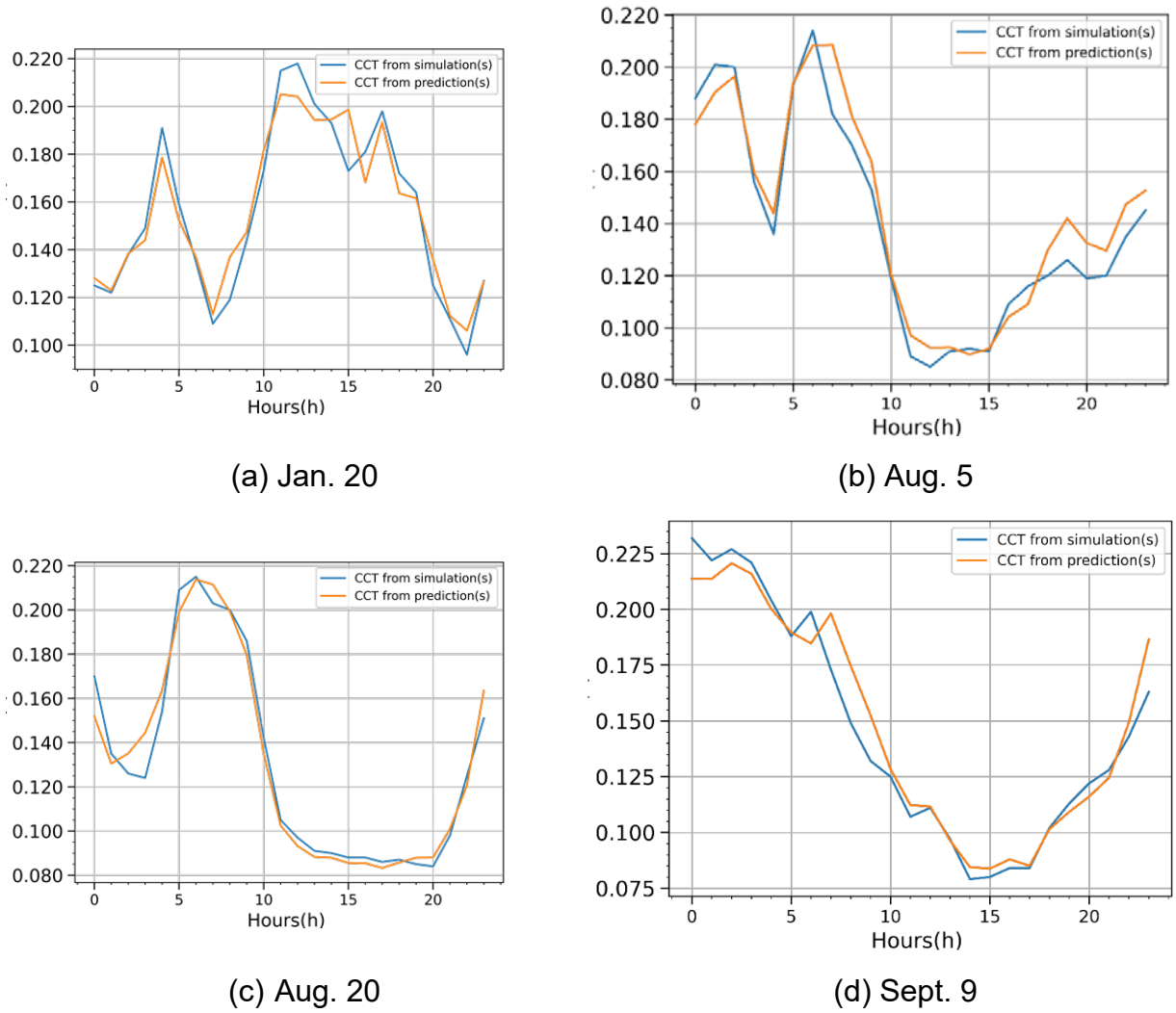

(a) Jan. 20

(b) Aug. 5

(c) Aug. 20

(d) Sept. 9

Figure 15. CCT prediction results of four selected days

B. AI based transient stability assessment on the 18-bus System

To obtain a complete picture of the transient stability of the 18-bus system, the transient stability margin is measured by the minimum critical clearing time (CCT) of the whole system. The critical bus in each area is defined as the bus that results in the minimum CCT. The CCT values of the critical buses in each area are shown as the colored solid line in Figure 16. The blue line shows the minimum CCT of the whole system, obtained by selecting the minimum CCT of the critical bus in each area.

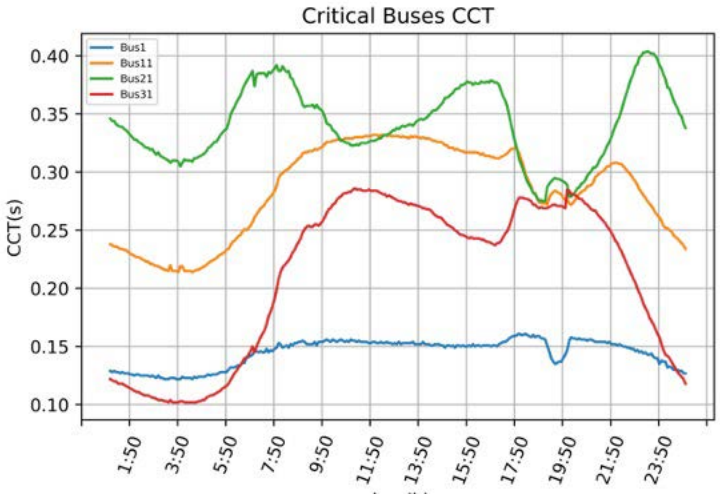

Figure 16. Change CCT values with dispatch for critical buses in the 18-bus system

The minimum CCT of the system is predicted using the artificial intelligence model. The comparison of the simulated CCT values with neural network and random forests results are shown in Figure 17 and Figure 18, respectively. Both artificial intelligence methods can achieve highly accurate CCT prediction.

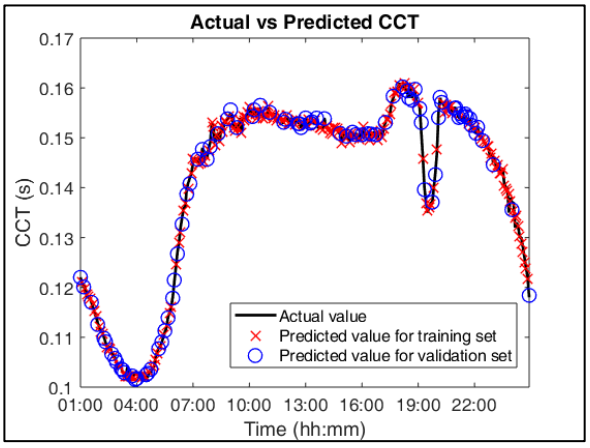

Figure 17. Actual and predicted CCT (neural network)

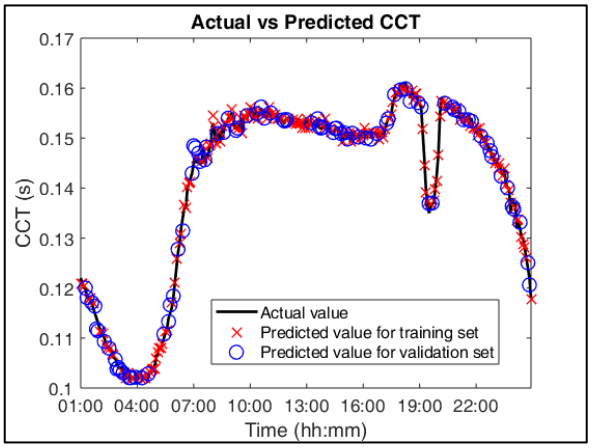

Figure 18. Actual and predicted CCT (random forests)

C. Data-driven Stability Assessment Tool Improvement Considering Topology Change

The DAS tool is improved to incorporate system topology change. The 18-bus system is used to generate topology change scenarios and test its performance in stability assessment.

In the 18-bus system, 288 power flow cases are generated based on the scheduling result, which consists of real power dispatch information for every 5 minute time snapshot in a 24-hour time range. In terms of its topology, this 18-bus system has 17 230kV AC lines and one 500kV AC line. Outages of these 18 high voltage transmission lines are used to simulate N-1 topology change. Combining 288 dispatch scenarios and 18 N-1 transmission outages, 5,184 case files are generated as the topology change dataset. Especially, the system power flow does not converge for the line outage between Bus 2 and 12 during 2:55-4:55 am, reducing the total number of cases to 5,159. According to previous research results, 4 critical buses, i.e. Bus 1, 11, 21 and 31, are buses with the smallest critical clearing time (CCT) in each area, as shown in Figure 16. Due to their small CCT values, faults on these four buses are of operators' primary concern and are used in developing and testing the transient stability assessment based on dispatch and topology information.

CCT values of these four critical buses are simulated for each of the 5,159 cases representing different combinations of dispatch and the system topology, totaling 20,636 CCT values. Each CCT value calculation involves multiple simulation runs with varying fault clearing time to pinpoint the turning point from stable to unstable simulation runs. In each simulation run, rotor angles of all machines are monitored. If the change of the rotor angle difference between any two generators exceeds 180 degrees, this simulation run is considered unstable. Otherwise, it is deemed stable.

To speed up the dataset generation, this work utilizes the python multiprocessing module to run all simulation cases in parallel on 6 computation cores, speeding up 3 times compared with running a single core. In addition, a 5ms accuracy is applied considering a balance between computation speed, practical needs and safety margins. Figure 19 shows the CCT values of a 3-phase fault on Bus 11 when dispatch and topology change. The black line in each graph represents the CCT values in the N-0 topology case (without a line outage), while different colored lines represent CCT values in different N-1 topology change scenarios. The profile of each line represents the impact of dispatch on CCT.

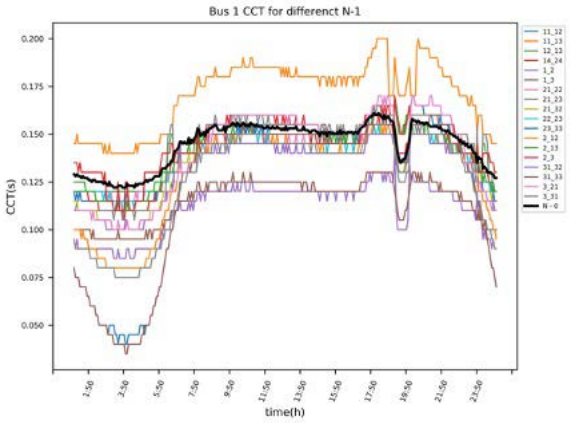

(1) Bus 1 CCT values with an N-1 line outage

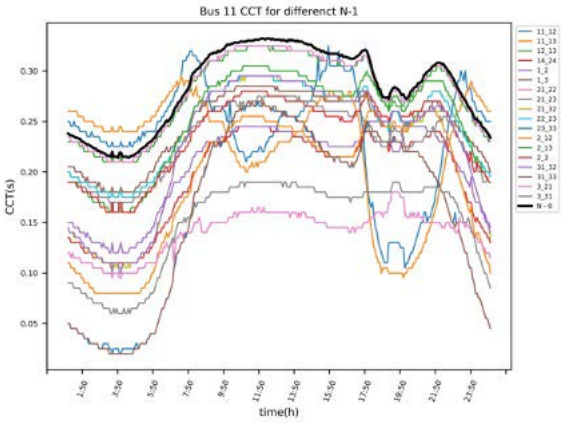

(2) Bus 11 CCT values with an N-1 line outage

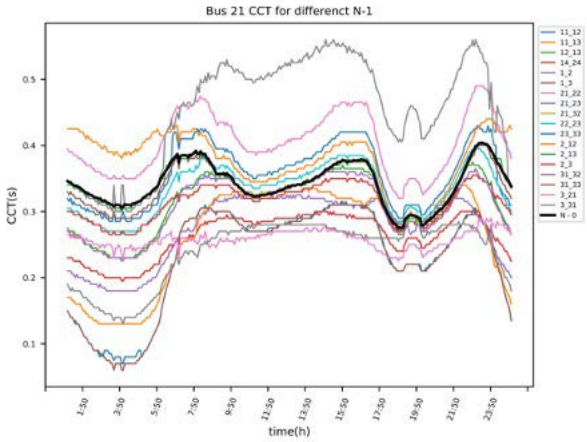

(3) Bus 21 CCT values with an N-1 line outage

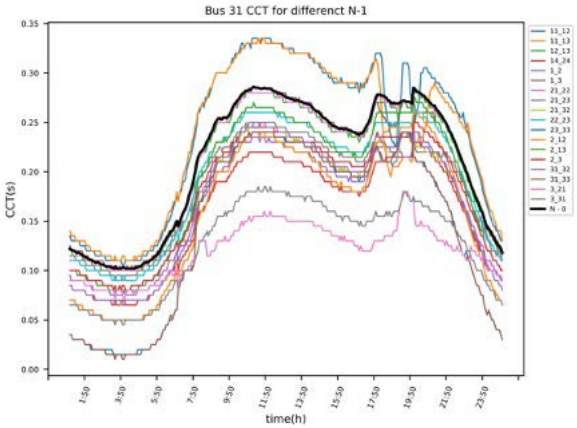

(4) Bus 31 CCT values with an N-1 line outage

Figure 19. CCT values with an N-1 line outage

The machine learning based stability assessment model is enhanced by adding another demension of input to incoprate topology change information. The informaiton of machine learning based stability assessment is shown in Table 11. The dataset generated on the 18-bus system is used to test its performance in stability assessment. As an example, the CCT values of Bus 11 predicted by neural network and random forests are shown in Figure 20. It can be seen the machine learning stability assessment approach has high accruacy in predicting CCT given a dispatch and system topolgy senario. In terms of computation time, trained mahine learning models can provide CCT estimation results instantly, making them valuable for various applications that needs real-time system stability informaiton.

Table 11. Information on Machine Learning Based Stability Assessment With System Topology Change

Input	**Output**	**Dataset generation**	**Machine learning models**	**Training and testing**
Generation dispatch information; Topology information.	Transient stability margin represented by CCT values	Generate a series of cases including different dispatch and topology scenarios; 3-phase fault on selected critical bus (with and without a line outage); Evaluate transient stability margin (CCT)	Neural network; Random forests.	70% data are selected randomly for training; the rest 30% data are used in testing.

Figure 21 shows the root mean square errors (RMSE) of transient stability prediction using neural network and random forests. It is noticed that while neural network and random forests have similar accuracy on matching the actual CCT in training, neural network has a 40% smaller error in validation compared with random forests. This result indicates neural network generally has a better performance in transient stability assessment. A closer examinaition on Figure 20 finds that neural network has significantly better performance at the turning points of the CCT curve compared with random forests. It indicates that neural network can better capture and model the non-linear relation between CCT and its impact factors. This is also consistant with previous observations on these two machine learning approaches when the system topology change was not considered.

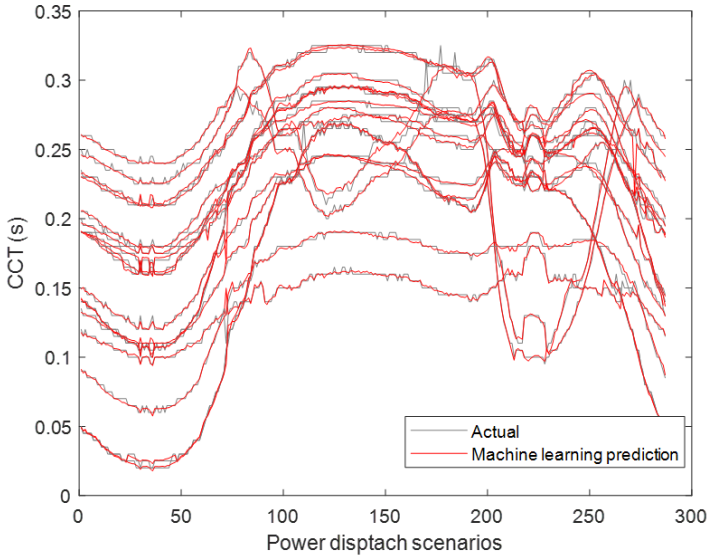

(a) Neural network result

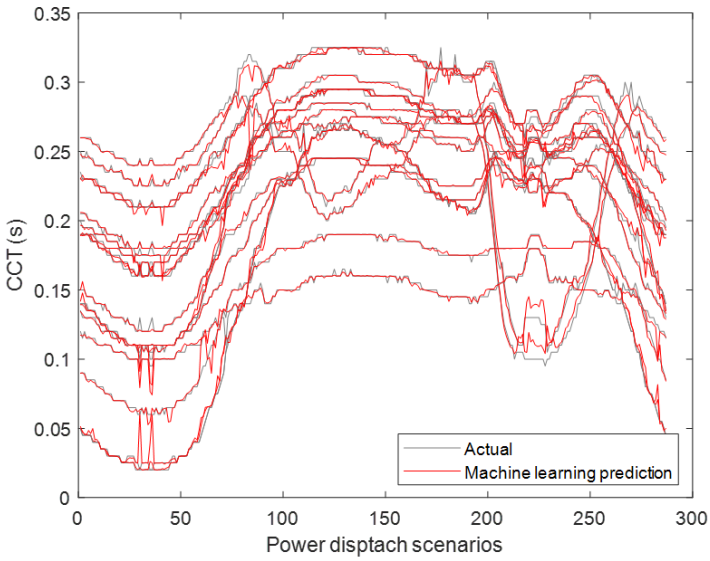

(b) Random forests result

Figure 20. Machine learning based CCT prediction with topology change (3-phase fault on Bus 11)

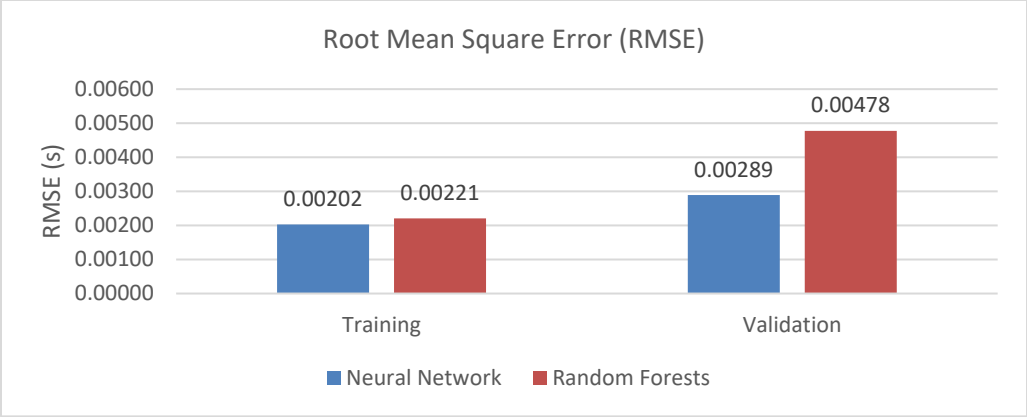

Figure 21. Root Mean Square Errors (RMSE) of transient stability prediction using neural network and random forests (3-phase fault on Bus 11)

D. Summary

We used the 240-bus reduced WECC system to study machine-learning-based transient angle stability prediction. The transient angle stability of the 240-bus system at 8,784 power flow scenarios were assessed using PSS/e simulation and binary search. Some power flow scenarios with small-signal instability issues were identified and removed from the 8,784 cases for the transient angle stability prediction study. The DSA tool based on neural network and random forests was applied to predict the CCT values and the prediction results show a high accuracy. This result indicates the capability of the tool in predicting system transient angle stability fast and accurately.

IV. Artificial Intelligence Based Frequency Stability Assessment

A. AI-based frequency stability prediction on the 240-bus reduced WECC system

In this study, the 240-bus reduced WECC system model with one year (8,784 hours) dispatch scenarios are used to test the performance of the AI-based frequency stability prediction. In addition, because of the large number of scenarios considered in this study, a dispatch based clustering approach is introduced to reduce the training dataset.

To study its frequency stability, Figure 22 gives its inertia distribution in one year, and Figure 23 presents a box plot of its distribution in each month. The inertia distribution shows a clear seasonal pattern, in which the summer has the highest inertia level while spring and autumn have some low inertia periods. This is primarily due to the differences in load and renewable generation in different seasons. For example, several low inertia periods in spring and autumn are caused by low load and high renewable generation. These months also have larger variations of inertia.

Figure 22. Inertia points in one year

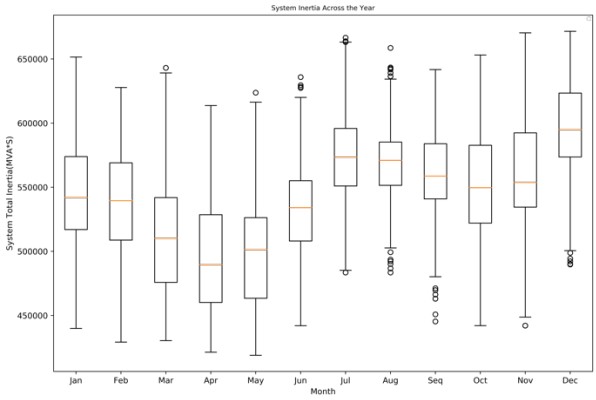

Figure 23. Inertia change in a box graph

The yearly distribution of the inertia data of the reduced WECC system is compared with the WECC inertia data in 2017, as plotted in Figure 24 and Figure 25. It can be seen that the reduced WECC system has lower inertia during daytime over the whole year. This is primarily due to higher solar generation in the reduced model. Some periods during night also see inertia decrease because of higher wind power penetration in the reduced model.

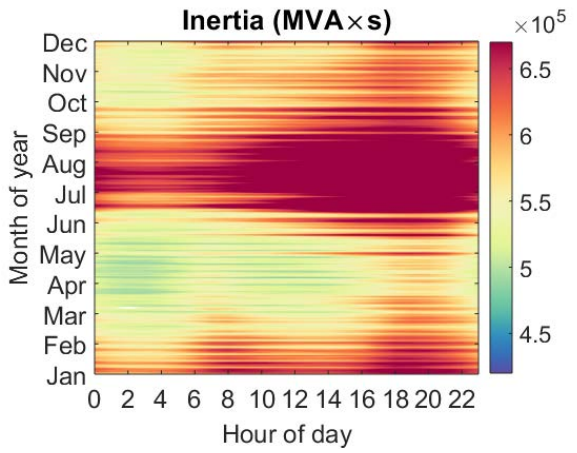

Figure 24. WECC system inertia

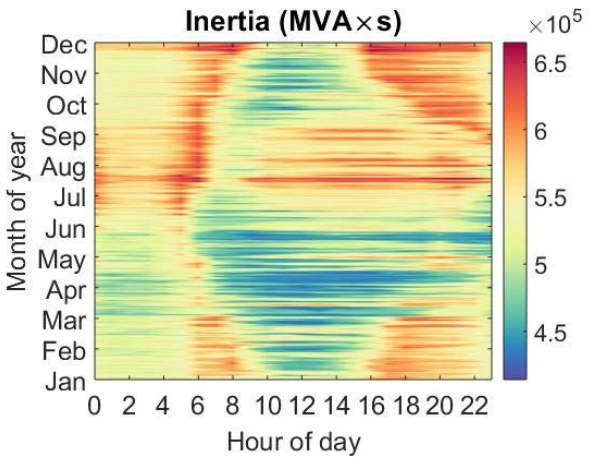

Figure 25. Reduce 240-bus WECC system inertia

In an N-1 contingency, a nuclear unit with 1,000 MW loading in California is used to simulate the frequency stability of the reduced system over the one year horizon. The simulated frequency nadir at each hour is shown in Figure 26. The distribution of frequency nadir has some correlation with the system inertia distribution (Figure 22). For example, periods with lower inertia and lower loads (March and April) generally have lower frequency nadirs. This phenomenon is reasonable since lower system inertia leaves less time for various frequency response mechanisms to deploy and arrest frequency decay, leading to a lower frequency nadir. In addition, lower inertia generally cooresponds to less generation and governor response, which also make the nadir lower.

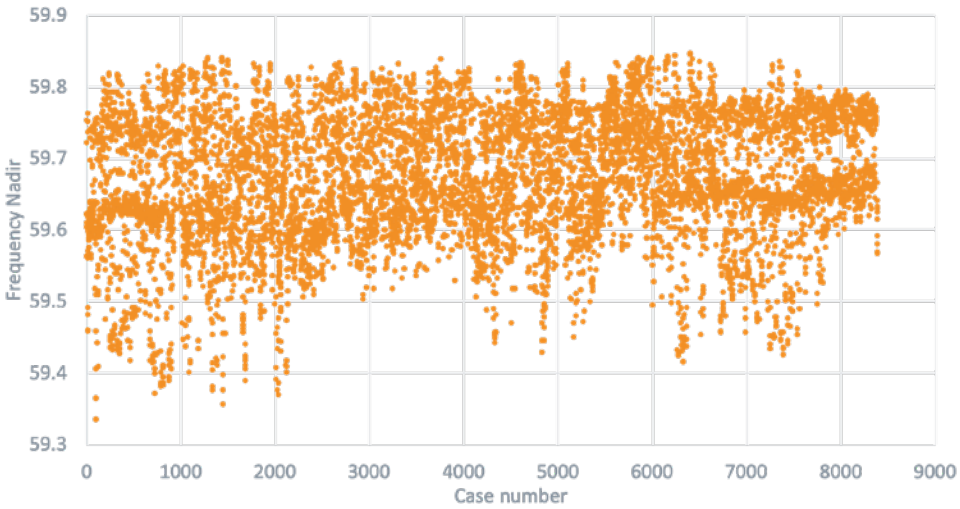

Figure 26. Frequency nadir distribution

For frequency stability study, the system inertia and dispatch pattern would be the most influential factors. In this project, we select each generator's real power output and inertia as clustering features. The 240-bus system has 146 generators in total, among which 109 are conventional generators and 37 are renewable generators including solar and wind power.

Since generator power output and inertia have different measurement units and value scales, the features need to be normalized before clustering, otherwise features with large magnitudes will play a dominant role in the clustering result.

Zero-mean normalization and min-max normalization are two typical normalization methods. In this work, since min-max normalization results do not generate negative values, it has more physical meaning than zero-mean normalization in normalizing the real power output. For example, normalizing feature p, the output of one generator, using the min-max normalization, can be represented as follows:

$$p = \frac{p - \min(p)}{\max(p) - \min(p)}$$

After normalization, each feature will have a 0 to 1 magnitude scale. For generator inertia, it will be either 0 or 1 after normalization depending on whether a generator is committed or not in a dispatch scenario.

Random forest is used to predict the system frequency nadir of the 240-bus reduced WECC system. 70% of the 8,784 dispatch scenarios are used for training; the rest 30% are spitted randomly and equally for validation and testing. Figure 27 shows the predicted and actual frequency nadir results. Figure 28 shows the error distribution of the prediction results. It can be seen that the prediction error is quite small: smaller than 0.1% (or 0.06 Hz).

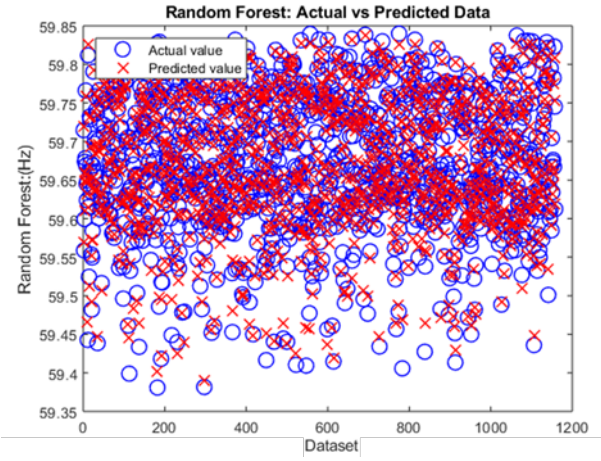

Figure 27. Predicted and actual frequency nadir distribution

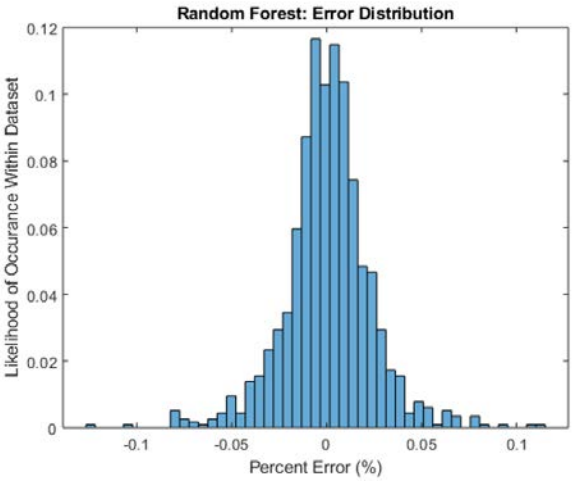

Figure 28. Distribution of the prediction error of frequency nadir

B. Clustering-based AI training dataset reduction on the 240-bus reduced WECC system

In practice, generating the training dataset is a time-consuming work even if parallel computation is used for acceleration. For the 8,784 scenarios in the 240-bus reduced WECC system, 8 CPUs in one machine were used in parallel to generate the simulation cases. It still took 10 hours to generate the training dataset. For transient stability prediction, the time consumption to generate the training dataset will be even larger (it is estimated at 160 hours for the 240-bus system) because multiple simulations are needed

to nail down the critical clearing time. Due to the substantial computation time needed for generating the training dataset, it has significant practical value to reduce the training dataset and save the simulation time in generating the training dataset. Therefore, this work will study clustering approaches in constructing the training dataset for AI based stability prediction to save time.

As an unsupervised machine learning, clustering is used to discover the data pattern based on features of interests and then group data based on similar features. Clustered data groups have similar features within each group and different features across different groups.

Many clustering approaches exist. Each approach has its application scope for the best performance. Some clustering approaches require a target number of clusters. Others require determining the maximum distance in one cluster. Here, two common clustering approaches: K-means++ clustering and affinity propagation are studied to reduce the training dataset.

(1) K-means++ clustering

K-means clustering presents the most commonly used category of clustering methods. It aims at minimizing the sample variance within a cluster by grouping data points based on their Euclidean distances. The samples in one cluster are always close to the center of this cluster compared with other cluster centers. In K-means clustering methods, the clustering number needs to be pre-determined. Its initial cluster center will also impact the clustering result. As an improved version of basic K-means clustering, K-means++ assigns the clustering center more optimally and reasonably than the basic K-means clustering approach.

(2) Affinity propagation

Different from K-means methods that require a pre-determined number of clusters, affinity propagation (AP) method can find an optimal number of representative cases that best summarize the data. In AP, real-valued messages are exchanged between data points until a high-quality set of exemplars and corresponding clusters gradually emerges. Due to the need to build an 8,784 by 8,784 matrix, the AP method requires more memory and computation time compared with other clustering method. In this study, since the desktop computer with 16GB could not meet the memory requirement, we run the affinity propagation program on the Google cloud with 60GB memory.

K-means ++ clustering is applied to cluster dispatch scenarios. The result shows the clustering can identify different dispatch patterns (summer peak, shoulder, off-peak, etc.), some of which are aligned continuously and concentrated in time. Figure 29 show the distribution of clusters in one year. Different sub-graphs represent the aggregation of clusters when different number of clusters are used. For example, in Figure 29 (a), all dispatch scenarios are clustered into two clusters: one cluster is concentrated in daytime periods while the other cluster in nighttime periods. The seasonal effect can also be noticed: most scenarios in summer belong to the “daytime cluster”, which covers only a

short period of peak load time during winter. This clustering result is primarily determined by the PV output and load level. As the number of clusters increases, it can further divide the clusters into more sub-clusters. As shown in Figure 29 (b), the “daytime cluster” is further divided into two clusters, one of which represents dispatch scenarios with relatively higher load and the other with lower load. With the increase of the cluster number, these clusters can be further divided into more sub-clusters. Each cluster will represent a smaller group of dispatch scenarios with similar features (with a finer resolution). Compared with Figure 25, it can be seen the clustering result has a similar pattern as the inertia. As the cluster number increases to 50, the one year dispatch scenarios are partitioned into even finer groups, as shown in Figure 30.

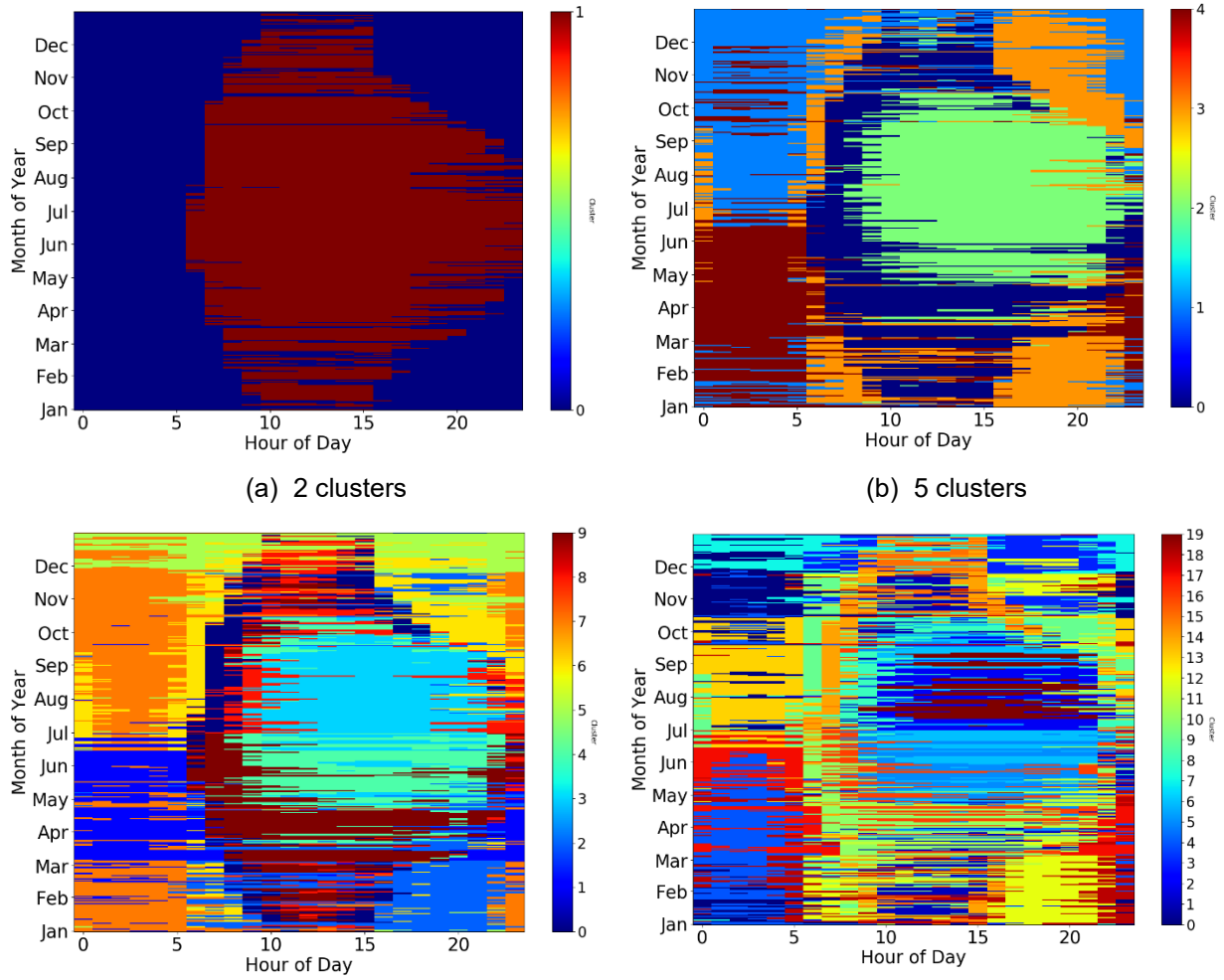

Figure 29. Clustering results visualized in hours/months

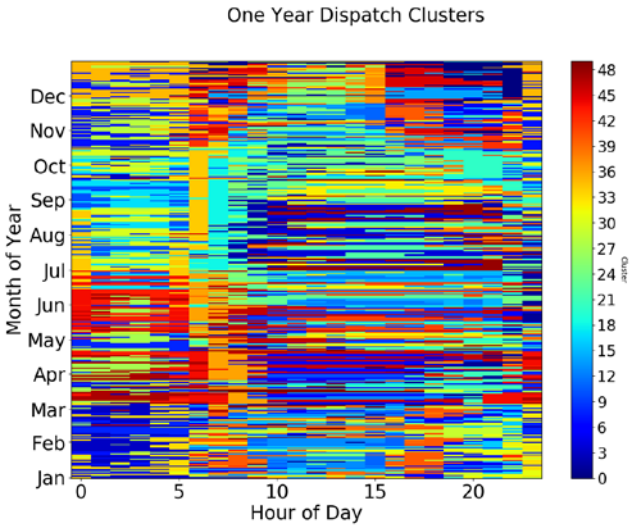

Figure 30. The clustering result of 1-year hourly dispatch

Figure 31 is the clustering result from affinity propagation clustering method, which clustered all the data into 443 clusters. It can be seen that most adjacent days and adjacent hours were grouped together, while a distinct seasonal pattern of change can be noticed primarily due to load and renewable variations. And because of the uncertainties and randomness of exact these variations, some swapping between dispatch scenarios in different seasons can be noticed in the clustering result.

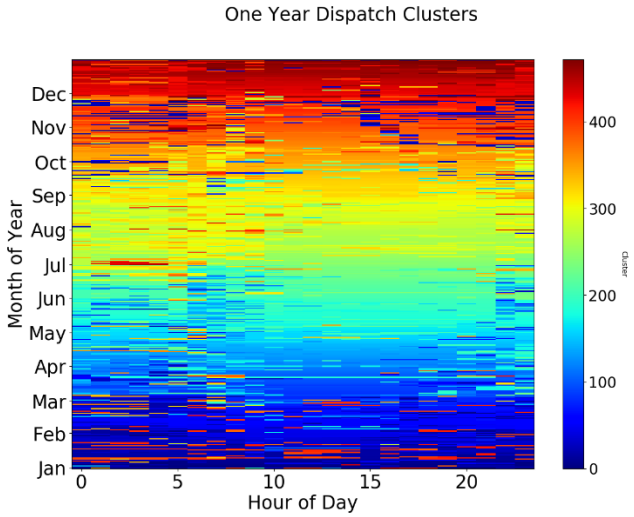

Figure 31. Affinity propagation clustering results visualized in hours/months

(different colors represent different clusters)

The 443 cluster-center data from the AP clustering result are used in the AI based frequency stability prediction. These data are used to train the machine learning model and 67 additional data points randomly selected from the 8,784 dataset are used to test the accuracy. Figure 32 and Figure 33 show the predcition result and accuracy. It can be seen that the maximum error is less than 0.08% (or 0.05 Hz). Comparing this result with

the Figure 28, the error range using the 443 clustered data is within the error range of using 6,146 (70% of the total data) randomly selected data.

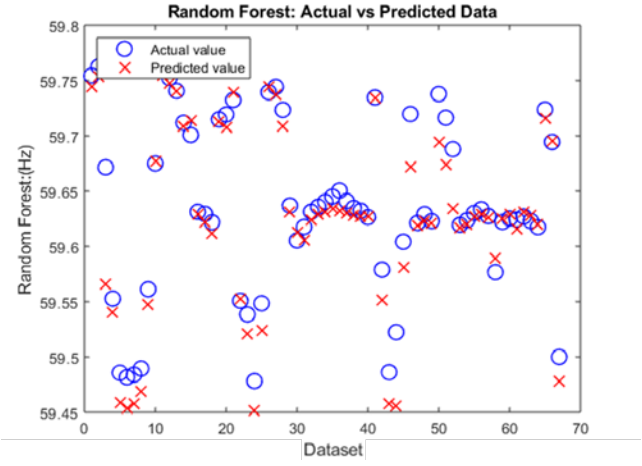

Figure 32. AI-based frequency stability prediction results based on 443 data obtained from AP clustering

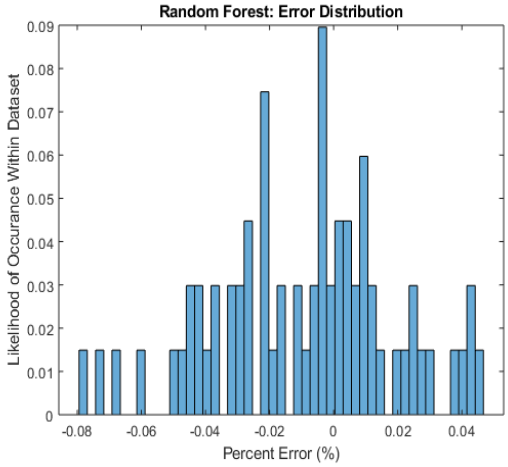

Figure 33. Percentage error distribution of AI-based frequency stability prediction based on AP clustering data

For comparison, Figure 34 and Figure 35 show the result using 443 randomly selected data from the original 8,784 dataset. The maximum error is around 0.18% (or around 0.11 Hz), which is much larger than the maximum error in the case using 6,164 randonly selected data in training. This comparision result proves that data clustering will effectively reduce the training data size while maintaining sufficiently high accuracy in the machine learning based stability assessment.

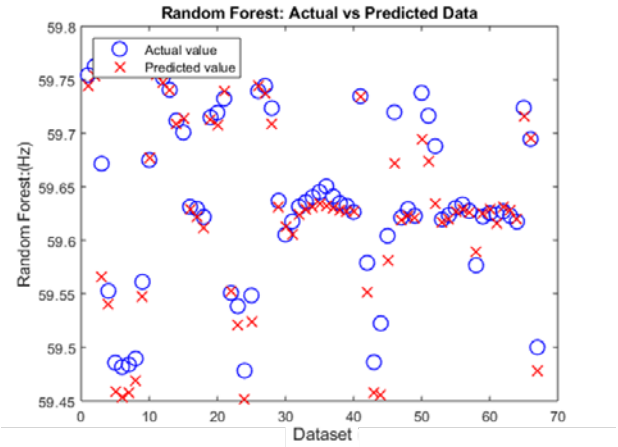

Figure 34. AI-based frequency stability prediction results based on 443 randomly selected data

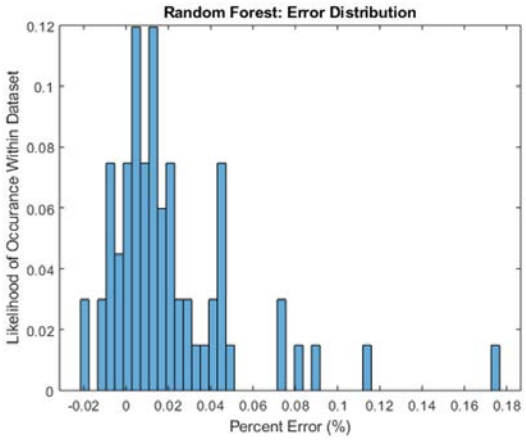

Figure 35. Percentage error distribution of AI-based frequency stability prediction based on 443 randomly selected data

C. Data-driven frequency stability on the 18-bus system

The data-driven frequency stability assessment was also applied to the 18-bus system. Details of frequency stability assessment considering inertia change are described as follows:

- Dataset description: frequency nadirs at different inertia conditions
- Dataset size:
    - (Inertia change only) 288 power flow scenarios (a 5-minutes step over 24 hours)
    - (Inertia + governor change) 288 power flow scenarios * 15 combinations of governors
- Input features: active power of all generators, total power generation of the system
- Estimation metric: frequency nadir (frequency stability margin)
- Training/testing sample number:
    - (Inertia change only) 200/88
    - (Inertia + governor change) 3,000/1,320

The estimation results of frequency nadirs when inertia changes are shown in Figure 36 and Figure 37. From these figures we can see that the developed machine learning tool can accurately predict frequency nadirs, and the estimation errors of frequency nadirs are less than 6 mHz.

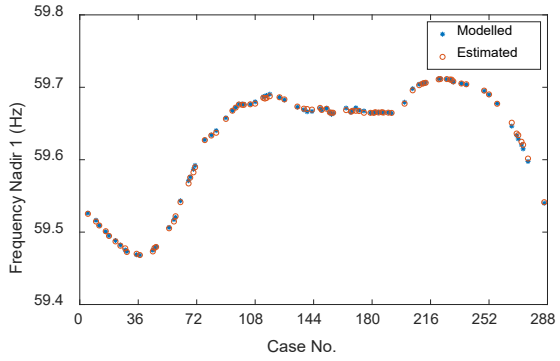

Figure 36. Frequency nadir of testing cases

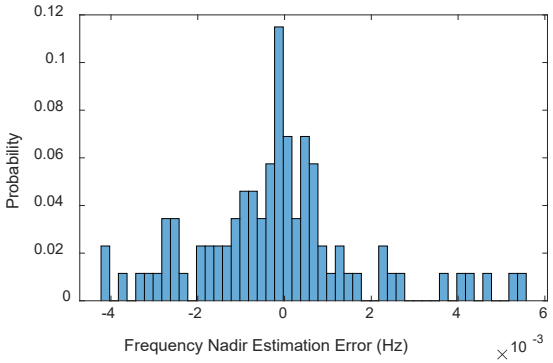

Figure 37. Frequency nadir estimation error distribution

The results of frequency stability assessment with different governor combinations and inertia changes are shown in Figure 38 and Figure 39. Results show that the developed machine learning tool can accurately predict frequency nadirs considering governor status. The largest error is around 0.06Hz.

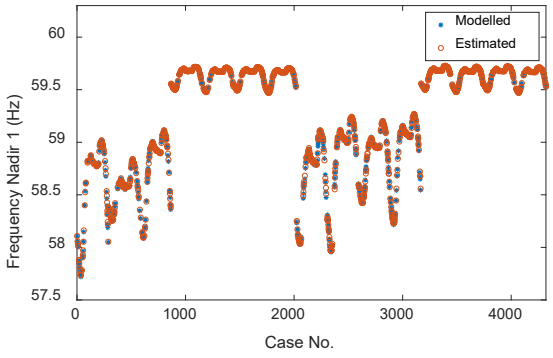

Figure 38. Modelled and estimated frequency nadir with different governor combinations

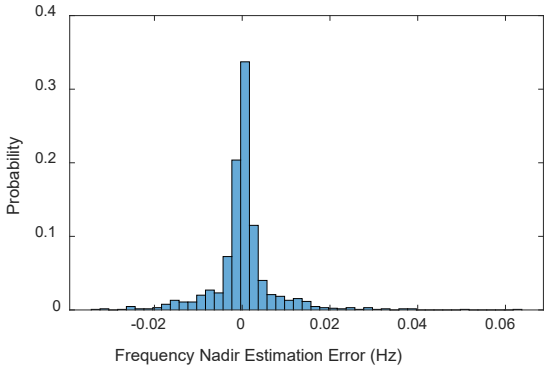

Figure 39. Frequency nadir estimation error distribution with different governor combinations

D. Summary

This section developed the technology to use AI to predict the frequency stability of power systems. The new approach was applied to 240 plus reduced WECC system and the 18-bus system. Results show that the proposed mastered has high accuracy in predicting frequency stability, and clustering datasets may help reduce the size of training data set and increase the model training efficiency.

V. Artificial Intelligence Based Small Signal Stability Assessment

A. AI-based stability assessment on the 240-bus system.

1) Oscillation Mode Study and Target Oscillation Mode

Small signal stability is the ability of the power grid to keep in synchronism after small disturbances. This quarter studied the machine learning based small signal stability prediction on the 240-bus reduced WECC system. In this study, we focused on the well-known N-S mode in WECC (N-S mode A and B merge to one mode because of the absence of the Alberta-U.S. connection in the reduced model). This oscillation mode has an oscillation frequency at around 0.3 Hz. The North area oscillates against the South area, Mexico area, and California area. The oscillation frequency and damping ratio of that mode were used to quantify the system small signal stability during different operation conditions.

For small signal stability, the 240-bus system SSAT analysis result has the same south-north oscillation mode (with 0.365Hz oscillation frequency, and 9.646% damping ratio) observed in the time domain simulation results. Figure 40 and Figure 41 show the mode shape and participation factors of the south-north oscillation mode of SSAT analysis results for the 240-bus system. This result validated that SSAT analysis results on the 240-bus system are trustworthy and laid a foundation for testing the DSA tool on small signal stability assessment using larger systems.

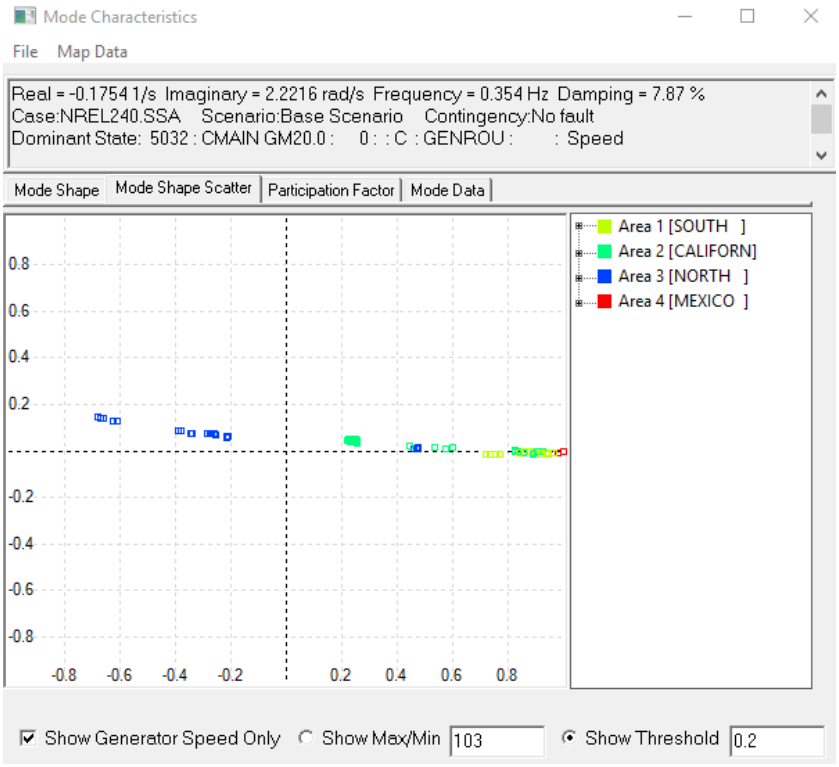

Figure 40. Oscillation mode shape of the south-north mode in the 240-bus WECC system

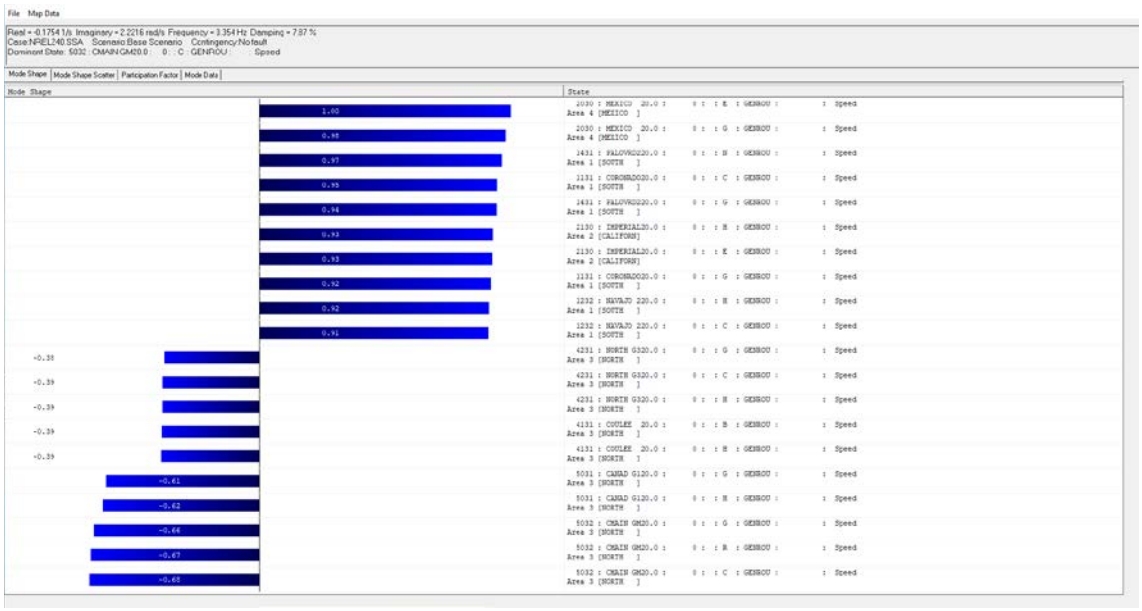

Figure 41. Oscillation mode participation factor of the south-north mode in the 240-bus WECC system

2.1.1 Oscillation Observation Channel Selection

We performed time-domain simulation in PSS/E to calculate the oscillation frequency and damping ratio. In this simulation, we applied a small probing disturbance to one generator's exciter. By analyzing the generators' rotor speed, we can get the oscillation frequency and the damping ratio of the target oscillation mode.

The system has multiple oscillation modes, some of which have oscillation frequencies that are close to that of the target oscillation. In addition, the target mode's oscillation frequency varies substantially with power flow. In order to select the exact target oscillation mode in each power flow scenario, we performed SSAT analysis and selected 10 generators' rotor speed as the observation channels. Among the 10 generators, five generators have the largest participation factors from one side of the oscillation mode shape and the other five generators' on the opposite side of the mode shape. The first five signals' oscillation phase angles lie in the range between -90 degrees to 90 degrees, while the rest five signals' oscillation phase lie in the range between 90 degrees to 270 degrees. Since the target mode's oscillation frequency is around 0.3 Hz and it varies with power flow, oscillation modes that have a frequency between 0.1 Hz to 0.5 Hz are included in the result to cover the target mode. The oscillation mode that meets the two standards is regarded as the target oscillation mode.

1. The first five signals' oscillation phase angles lie in the range between -90 degrees to 90 degrees, while the rest five signals' oscillation phase lie in the range between 90 degrees to 270 degrees.

2. The oscillation mode has an oscillation frequency between 0.1 Hz to 0.5 Hz.

Figure 42 shows the oscillation analysis result of one dispatch result. The yellow-colored rows are selected to belong to the target oscillation mode. After pinpointing the target oscillation mode, its oscillation frequency and damping ratio are retrieved and further used to construct the machine learning database.

Month	Day	Hour	Channel	Oscillation Frequency	Damping Ratio	Angle	Error
1	1	0	1	0.1961	35.965	246.29	0.000873
1	1	0	1	0.36033	4.6023	182.37	0.000873
1	1	0	2	0.18652	42.205	120.86	0.000638
1	1	0	2	0.36035	4.608	181.92	0.000638
1	1	0	3	0.2373	43.429	-37.524	0.001324
1	1	0	3	0.36034	4.5908	181.34	0.001324
1	1	0	4	0.25917	35.081	10.427	0.001353
1	1	0	4	0.36019	4.5682	182.66	0.001353
1	1	0	5	0.2105	25.237	-87.335	0.000658
1	1	0	5	0.36032	4.6067	181.98	0.000658
1	1	0	6	0.12158	49.183	44.996	0.000799
1	1	0	6	0.36126	4.8843	6.2916	0.000799
1	1	0	6	0.33803	2.646	-82.625	0.000799
1	1	0	7	0.30612	9.6176	232.99	0.000465
1	1	0	7	0.36041	4.8243	4.5008	0.000465
1	1	0	8	0.30695	5.6079	150.47	0.000457
1	1	0	8	0.36058	4.8051	4.963	0.000457
1	1	0	9	0.31044	7.9142	211.51	0.000674
1	1	0	9	0.36052	4.8314	5.0175	0.000674
1	1	0	10	0.30855	10.298	227.48	0.000479
1	1	0	10	0.36042	4.8524	5.7122	0.000479

Figure 42. Select the oscillation components in the target oscillation mode

In the 8,784 power flow scenarios, some cases have the small signal stability issue. The system under these operation conditions will not be able to maintain stability even after a small disturbance. These cases show instability after applying a small disturbance. Figure 43 gives two examples of the simulation result of unstable cases. We identified around 2,000 such cases. Since the oscillation analysis method can not accurately analyze oscillation modes of unstable cases, these cases are removed from the quantitative prediction study. After removing, the rest 6,000 power flow scenarios have valid oscillation frequency and damping ratio information to train and test the machine learning model.

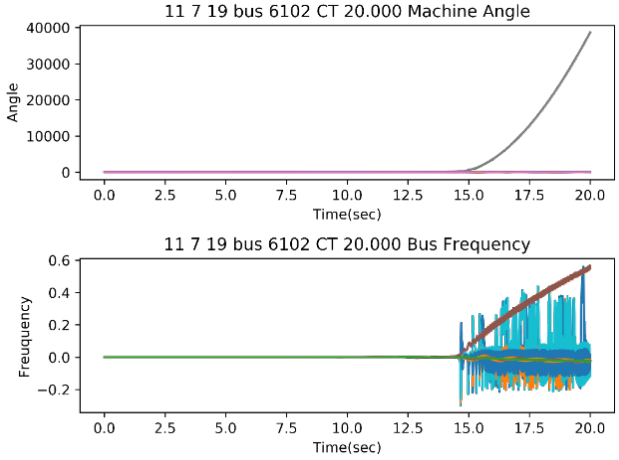

Figure 43. The simulated frequency and angle of small-signal-unstable scenarios

2) AI-based Small Signal Stability prediction for the 240-bus reduced WECC system

We applied neural network to predict the small signal stability of the 240-bus reduced WECC system. The input and output data information are given in Table 12. The dataset is divided into two subsets: 80% data are used for training (68%) and validation (12%); the rest 20% data are used for testing.

Table 12. Data Entries for CCT Prediction

Input/output	**Data**	**Number of Data Entries**
Input	Total generation	1
	Total load real power	1
	Total system inertia	1
	Generator power output	146 (number of generators)
	Load power	139 (number of loads)
	Generator's inertia contribution	146 (number of generators)
Output	Oscillation frequency	1
	Oscillation damping ratio	1

The oscillation frequency prediction performance and error distribution are shown in Figure 44 and Figure 45. The prediction performance for the oscillation damping ratio is shown in Figure 46 and Figure 47. It can be seen that the oscillation frequency prediction has a relatively higher accuracy compared with oscillation damping ratio. The distribution of the prediction error is almost symmetric to the Y axis for both the oscillation frequency and the damping ratio, implying a desired feature that errors have a close-to-zero expectation. In addition, the result shows that when the damping ratio is small, the machine learning prediction result tends to have a larger error.

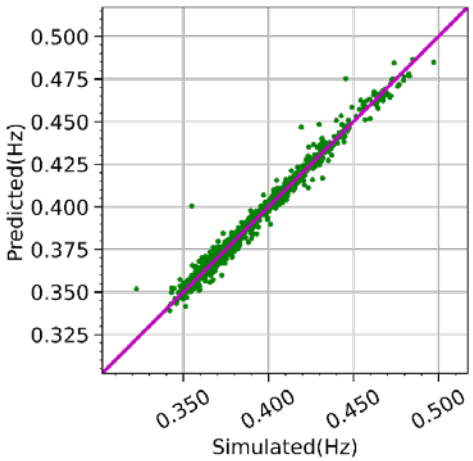

Figure 44. Oscillation frequency prediction result

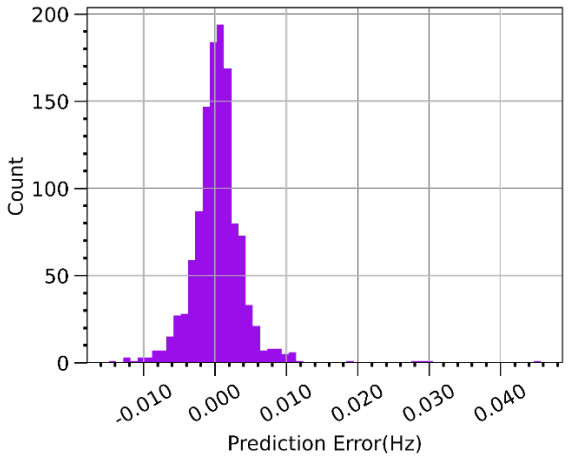

Figure 45. Oscillation frequency prediction error distribution

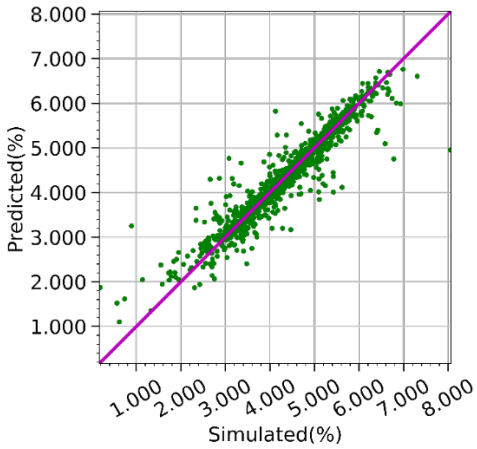

Figure 46. Oscillation damping ratio prediction result

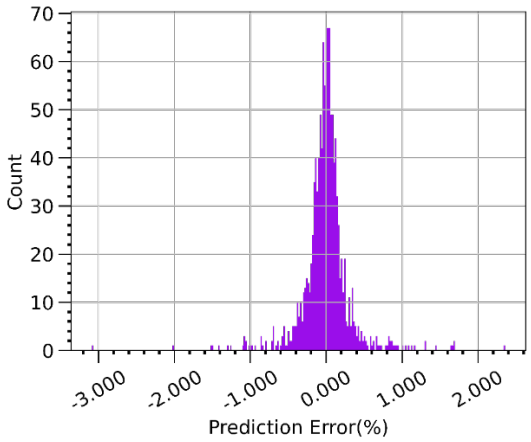

Figure 47. Oscillation damping ratio prediction error distribution

B. Stability assessment on the 18-bus system.

The 288 saved cases of the 18-bus system were also used in the small-signal stability assessment. Because power flow files had already been generated in PSS/E, these files were inputted into SSAT to create a case for each dispatch level. Each SSAT case accepts a single PSS/E power flow file in RAW format, along with a single dynamic (DYR) file. Because 288 power flow files were generated, every five minutes over a 24-hour period, 288 SSAT cases were also created. The dynamic file inputted was the same for all 288 SSAT cases. Since SSAT does not have an application programming interface (API) to easily create a batch of dynamic cases, a MATLAB script was used to change the filename of the PSS/E RAW file to be inputted, since SSAT cases can also be read with a text editor.

After SSAT cases were created for each dispatch level, a small-signal stability computation was run on each case. The selected computation was full eigenvalue analysis. All modes, with corresponding frequencies and damping ratios, were outputted for each SSAT case. SSAT has a tool called Case Scheduler to run batch simulations. A

list of SSAT cases were loaded into the Case Scheduler and run at once. Damping ratio was selected as the metric of small signal stability. The damping ratio is a dimensionless measure describing how oscillations in power system decay after a disturbance. Ideally, the system is stable if the damping ratio is positive and unstable if the damping ratio is negative.

The data-driven small signal stability assessment was performed on the 18-bus system. Firstly, full eigenvalue analysis was performed on the 18-bus system in SSAT. All the eigenvalues of the 18-bus system are shown in Figure 48. There are 47 oscillation modes in total. Three of them have low damping ratio which is marked as mode 1, mode 2 and mode 3, respectively, in Figure 48. These three oscillation modes affect the system performance most. Therefore, the small signal stability assessment mainly focuses on these three modes. The participation factors for three oscillation modes are listed in Table 13.

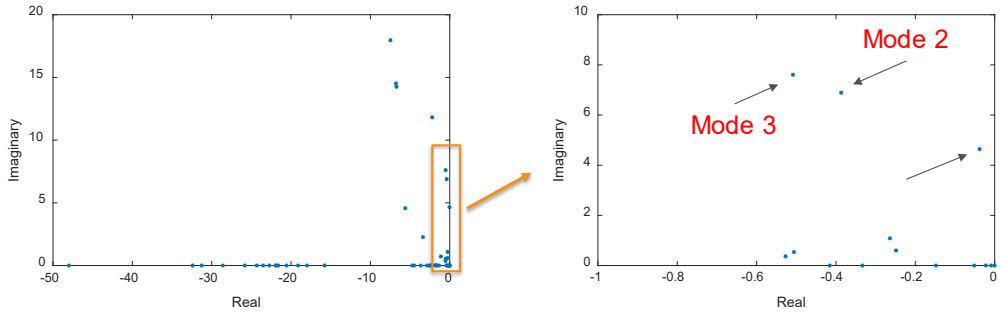

Figure 48. Eigenvalues of the 18-bus system

Table 13. Participation Factors for the Three Oscillation Modes

Generator	Participation factor		
	Mode 1	Mode 2	Mode3
North G1	0.01	1.00	0.15
West G1	1.00	0.41	0.01
SOUTH G1	0.09	0.26	1.00
East G1	0.60	0.63	0.13

From Table 13, it is seen that WEST G1 and EAST G1 are involved most in Mode 1 (which is two generators' oscillation); all generators are involved in Mode 2 (which is inter-area oscillation); only SOUTH G1 is involved in Mode 3 (which is single generator oscillation). The detailed information of small signal stability assessment can be described as follows:

- Dataset description: damping ratio subjected to system dispatch
- Dataset size: 288 power flow scenarios with 5 minutes step over 24 hours
- Input features: active power of all generators, total power generation of the system

- Estimation metric: damping ratio
- Training/testing sample number: 200/88

The results of small signal stability assessment for these three oscillation modes are illustrated in Figure 49 to Figure 54. From these figures, we can see that the estimated results agree well with the modelled results. The maximum damping ratio estimation errors of these modes range from 0.18% to 0.35%.

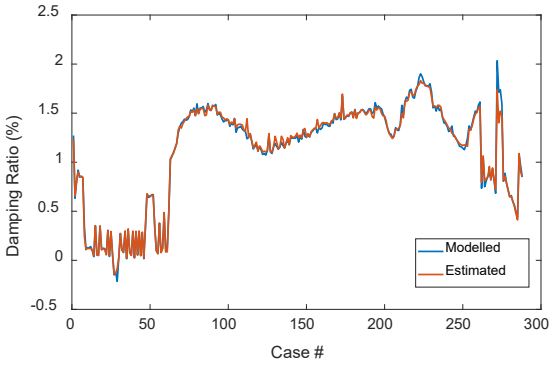

Figure 49. Modelled and estimated damping ratio in testing dataset for mode 1

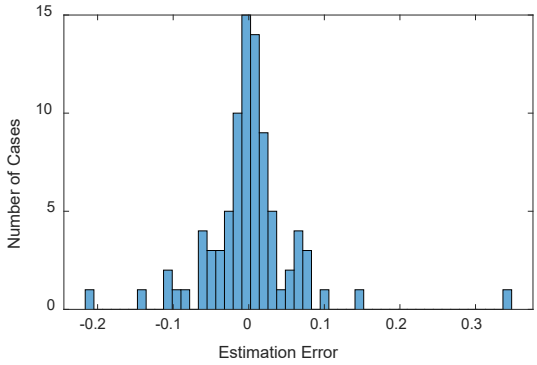

Figure 50. Damping ratio estimation error distribution for mode 1

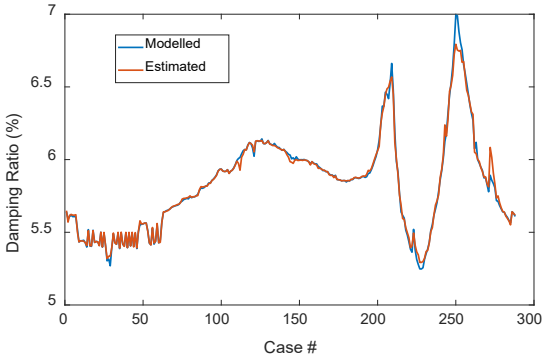

Figure 51. Modelled and estimated damping ratio in testing dataset for mode 2

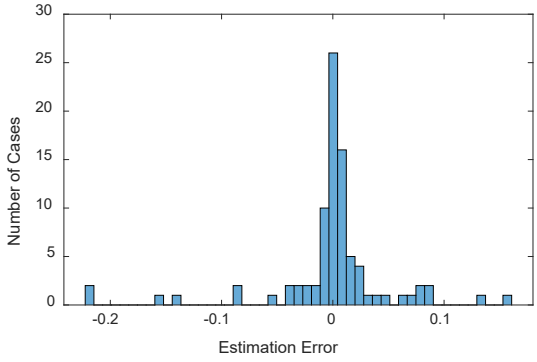

Figure 52. Damping ratio estimation error distribution for mode 2

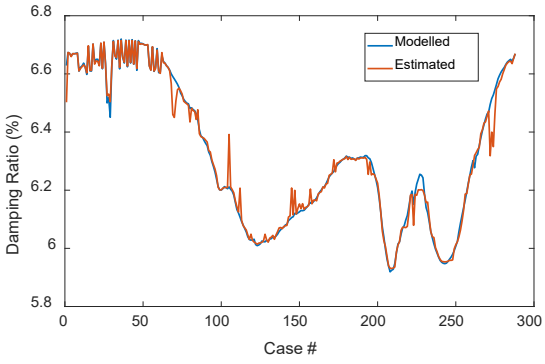

Figure 53. Modelled and estimated damping ratio in testing dataset for mode 3

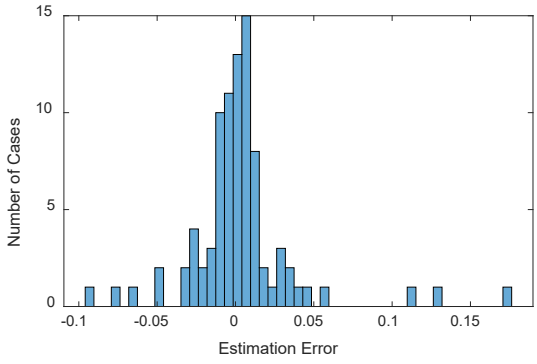

Figure 54. Damping ratio estimation error distribution for mode 3

Table 14 summarized the accuracy and computation time of stability assessment using artificial intelligence in the 18-bus system. It can be seen that both random forests and neural network reach high accuracy for the three stability assessment tasks using the same set of power flow input data. Neural network has higher accuracy than random forest except for small signal stability assessment. In addition, the artificial intelligence-based method significantly reduces the computation time compared with conventional stability assessment methods. This result indicates that artificial intelligence has good capability in stability assessment. This approach can save the data preparation efforts and benefit multiple applications in which accurate and fast stability assessment is desired, such as real-time security margin assessment, short-term stability prediction for system adjustment, stability-related resource procurement and stability validation in day-ahead markets, and stability margin assessment of multiple power flow scenarios in long-term planning.

Table 14. Accuracy of Different Testing of Artificial Intelligence Based Stability Assessment

Stability	**Estimation accuracy**		**Time for stability assessment (86 dispatch scenarios)**	
	Random forests	Neural network	Time domain simulation	Artificial intelligence based
Frequency	98.30%	99.72%	~1 h	~0.18 ms (with trained model)
Transient	98.44%	99.29%	~16 h	
Small-Signal	98.61%	98.59%	~1 h	

C. Summary

In this quarter, we used the 240-bus reduced WECC system and the 18-bus system to study machine-learning-based small signal stability prediction. In the 240-bus system, we focused on the well-known WECC N-S inter-area oscillation mode, whose frequency and damping ratio are quantified by PSS/E time-domain simulation and signal processing in Matlab and python. The DSA tool based on the neural network algorithm was applied to predict the oscillation frequency and damping ratio. The result shows that both oscillation frequency and damping ratio can be predicted fairly accurately based on power flow data. The oscillation frequency has a higher prediction accuracy compared with the damping ratio. Work in the next quarter will be enhance the tool to identify unstable cases and predict transient stability considering N-1 topology change.

VI. AI-BASED WECC-1 REMEDIAL ACTION SCHEME (RAS) IMPROVEMENT

A. WECC-1 RAS-1 Introduction

This study is based on the reduced WECC 240-bus system model developed by NREL, which has generation of different fuel types, e.g., coal, gas, bio, nuclear, hydro, wind, and solar. The renewable (wind and solar) generation penetration level varies from 0.2% to 49.2% across 8,786 hourly dispatches of an entire year of 366 days.

WECC-1 RAS is selected for this study. As shown in Figure 55, the tie lines connecting the south area (California, Arizona, and New Mexico) and the north area (Origen, Nevada, Utah, and Colorado) are tripped to mimic the actions of WECC-1 RAS and followed by corrective actions to maintain the system stability. In reality, load shedding and generation trip at predetermined locations in two islands respectively are used to maintain the two islands' frequency between 59.5 Hz and 60.5Hz. For simplicity, proportional load decrease in one island and proportional load increase in the other island are used to generate the training database in this study.

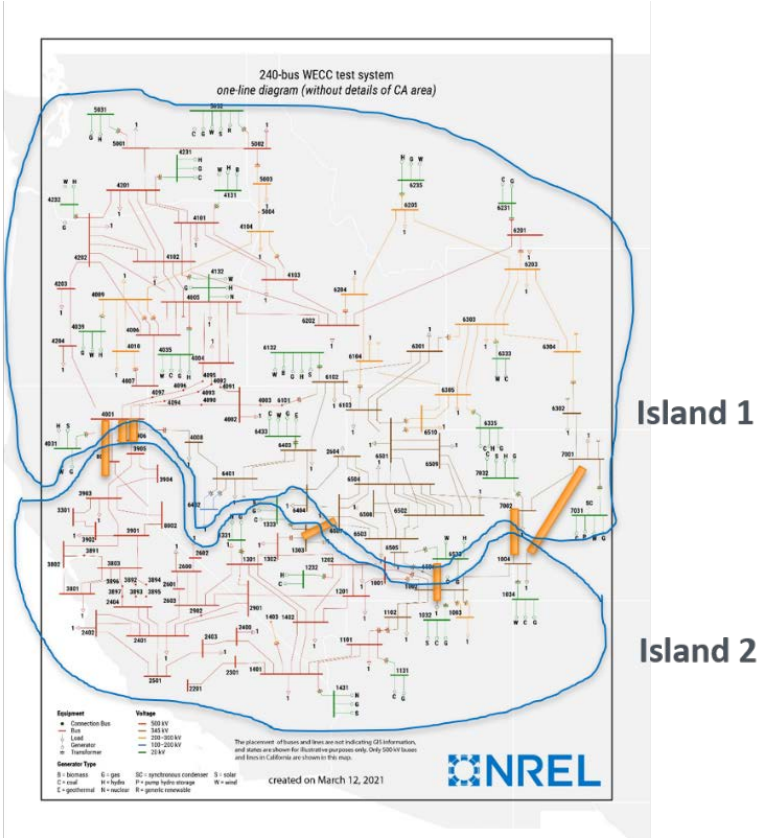

Figure 55. One-line diagram of 240-bus WECC test system model

B. AI Based RAS

The dataset is comprised of 8,784 total power flow scenarios. Approximately 2,000 of these cases were identified to have stability issues, and were excluded from the training dataset. Two examples of unstable power flow cases are shown in Figure 56.

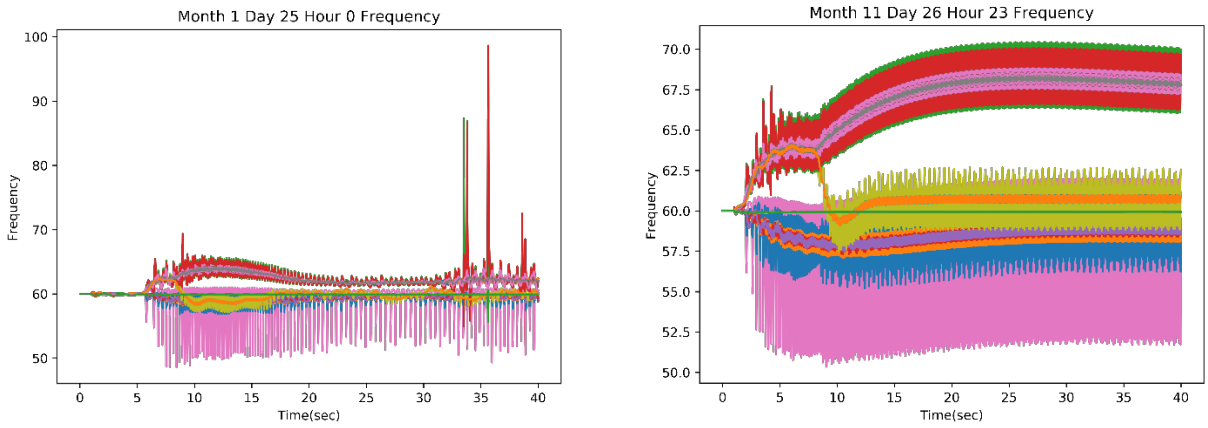

Figure 56. Cases with stability issue

In order to get the optimal MW amount, we perform the iterative simulations and fine tune the MW amount until the two systems' maximum/minimum frequencies marginally reach 59.5 Hz and 60.5 Hz respectively according to the following procedures.

1) Adjust (increase or decrease) load in two systems according to their tie-line power flow MW after RAS activation.

2) If two systems' maximum/minimum frequencies do not marginally reach 59.5 Hz and 60.5 Hz respectively, change the MW adjustment amount based on the frequency nadir of the last simulation. Run multiple simulations until we get the optimal MW amount for load adjustment for two separate systems.

Figure 57(a) shows the frequencies of the two islanded systems when RAS performs load adjustment according to tie-line flows. In this case, the tie-line flows for the PNW and CA system are 6,177.922 MW and -6,073.320 MW respectively. Figure 57(b) shows the frequency of the two islanded systems when RAS performs the optimal load adjustment. The optimal load adjustment are 2996.882 MW and -4928.92 MW respectively. Optimal power is cost effective compared to tie line flow, and in this example case, it avoids an extra 3181.04 MW load increase and 1144.4 MW load decrease in the two islanded systems.

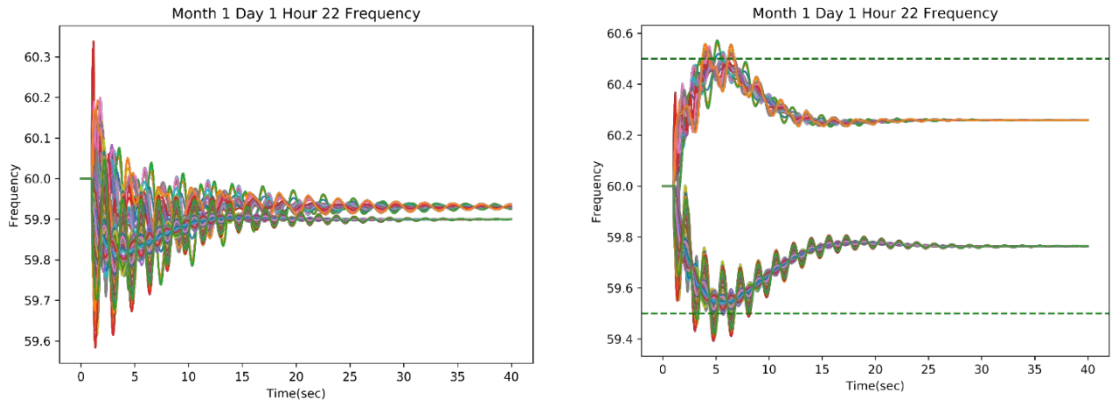

(**a**) (**b**)

Figure 57. (a) Load adjustment power equals tie line flows; (b) Optimal Load adjustment power maintains two islanded system at 59.5Hz and 60.5Hz respectively.

Deep learning was used to predict the active power needed in two separated systems after WECC-1 RAS. The input and output data information are given in Table 15. The dataset is divided into two subsets: 80% of data is used for training (68%) and validation (12%), while the remaining 20% is used for testing.

Table 15. Data Entries for Load Adjustment Prediction

Input/output	**Data**	**Number of Data Entries**
Input	Total generation	1
	Total load real power	1
	Total system inertia	1
	Generator power output	146 (number of generators)
	Load power	139 (number of loads)
	Generator's inertia contribution	146 (number of generators)
Output	Load Increase	1
	Load Decrease	1

The active power prediction performance and error distribution are shown in Figure 58 and Figure 59. It can be seen that the standard deviation for the MW increase prediction error is around 96MW, meaning that there is a 66% probability that the load increase prediction error is 96 MW or less. This error standard deviation is larger for load decrease prediction, at 146 MW.

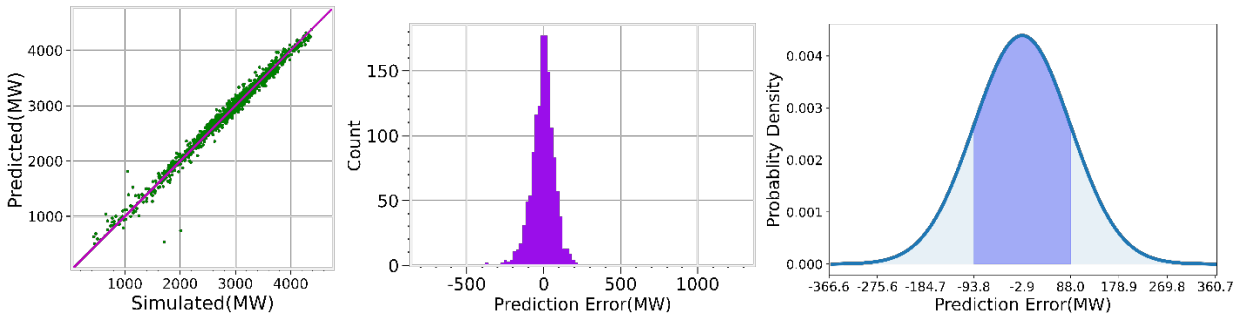

Figure 58. Load Increase Power prediction result

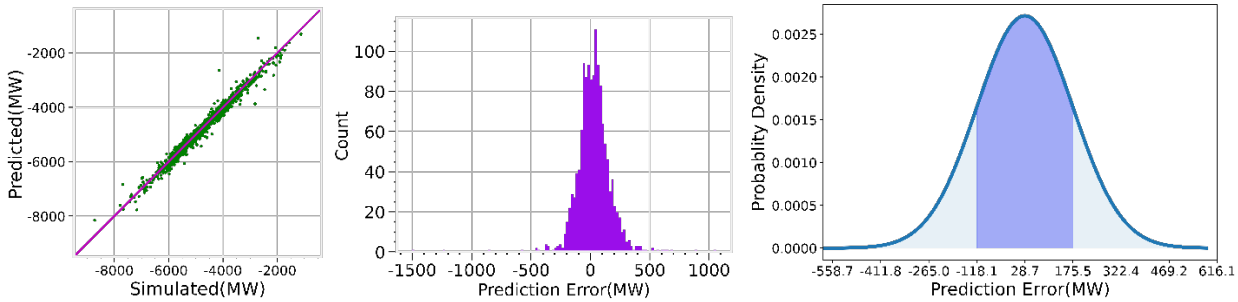

Figure 59. Load increase power prediction result

1) Deep Learning Neural Network Structure for Adaptive RAS

Deep learning neural network can use multiple layers to abstract the information based on the previous layer, and progressively abstract the input features, resulting in better generalization. As shown in Figure 60, this study uses a fully connected feedforward neural network with more than one hidden layer to map the operating conditions to the optimal WECC-1 RAS corrective actions. The operating conditions include total generation, total load, total inertia, power output of each generator, inertia of each generator, and each load. The outputs are the corrective actions, such as load increase MW amount and load decrease MW amount in two islands, respectively.

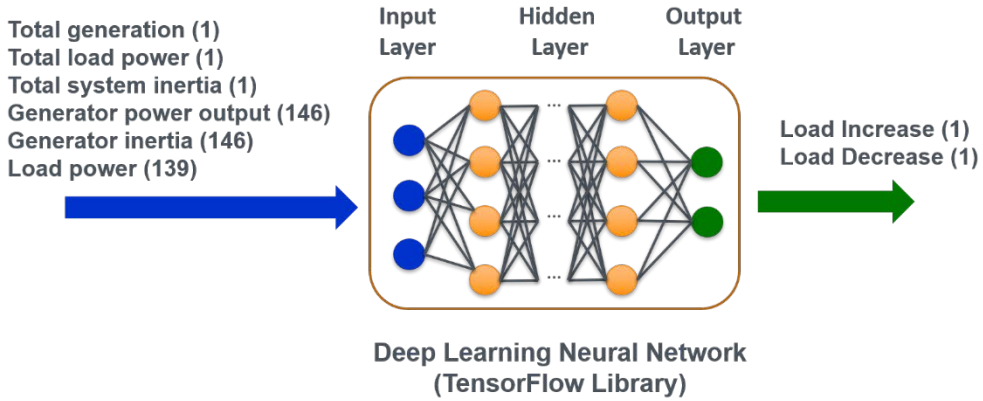

Figure 60. Neural network structure for RAS study

2) Customized Loss Function

In this study, a customized loss function is proposed to make the model favor the positive error more than the negative error. The customized loss function is shown in (2).

$$E = \begin{cases} \left(\hat{Z} - Z\right)^2 \; if \; \left|\hat{Z}\right| > |Z| \\ \left(N * \left(\hat{Z} - Z\right)\right)^2 \; if \; \left|\hat{Z}\right| < |Z|, N > 1 \end{cases} \quad (2)$$

where Z is the ground truth of load increase or load decrease, $\hat{Z}$ is predicted load increase and load decrease, and N is the penalizing factor.

When $\hat{Z}$ is greater than Z, the two islands' frequency will not trigger under-frequency load shedding or over-frequency generation trip. When $\left|\hat{Z}\right|$ is less than $|Z|$, the loss function will be penalized by enlarging N times. N decides the degree of conservativeness. The greater the penalizing factor N, the more conservative of the prediction results.

Although the model result is highly accurate, error is measured as the distribution around the mean of zero. This means that load increase cases with negative error will trigger an over-frequency generation trip, and load decrease cases with positive error will trigger under-frequency load shedding. To solve this issue, the neural network model should not only minimize the loss, but also make the loss selection behavior conservative. A customized loss function is proposed to make the model favor positive error during load increase and negative error during load decrease.

In equation (2), Z is the ground truth of load adjustment in MW to maintain the two islanded systems at their respective frequencies. $\hat{Z}$ is the load adjustment in MW calculated by the neural network during the training process. When the absolute value of the output of model $\hat{Z}$ is greater than the ground truth Z, error is simply the squared error of the two Z values. When the absolute value of the model $\hat{Z}$ output is less than ground truth Z, the loss function will penalize the error N times as the squared error.

By customizing the loss function in equation (2), the model will predict the load adjustment amount conservatively. The penalizing factor N in the loss function will determine the degree of conservatism. The greater the penalizing factor N, the more conservative the model prediction. Although high penalty factors result in more cases within the safety margin, higher penalty factors also cause the error to be more scattered, indicating a less accurate neural network model.

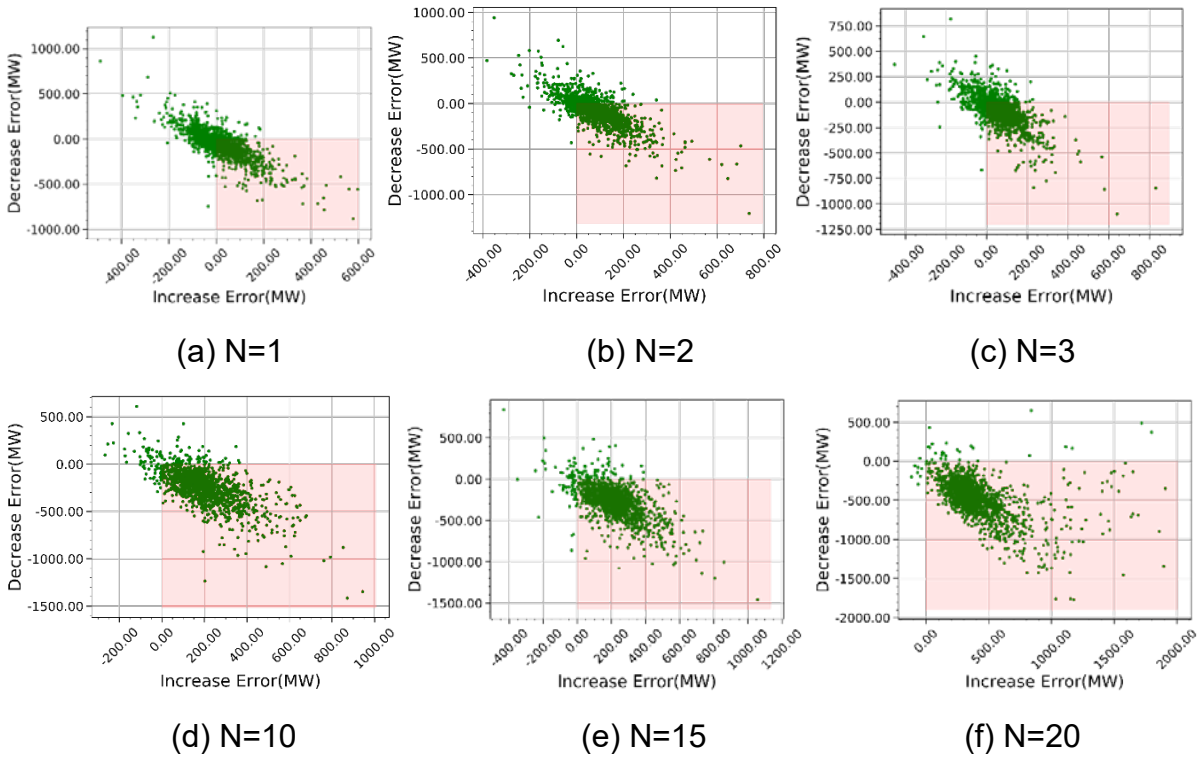

Figure 61. Load increase power prediction result

In this study, *N*=10 is selected as the penalization factor for the loss function. The data in Figure 62 and Figure 63 show the frequencies of the islanded systems with and without a customized loss function. Approximately 58% of cases fall within the safety margin with non-customized loss function. This value jumps to 92% with the customized loss-function, a considerable improvement.

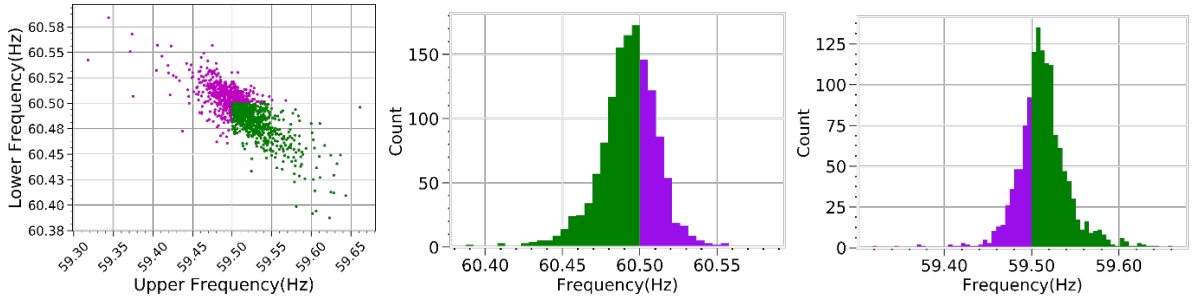

Figure 62. Two islanded system frequency without customized loss function

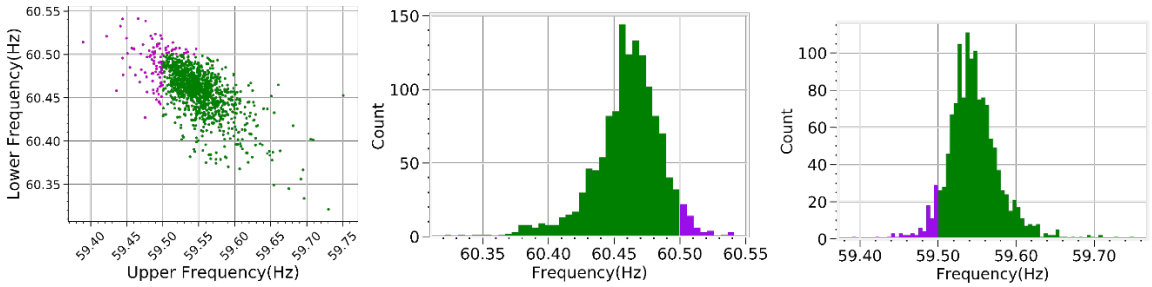

Figure 63. Two islanded system frequency with customized loss function

3) Evaluation Metrics

Root of mean squared percentage error (RMSPE) and mean absolute percentage error (MAPE) are used for evaluation metrics which can make comparisons between data with different scales. The RMSPE and MAPE calculation is given in (3) and (4).

$$RMSE = \sqrt{\frac{1}{m}\sum_{i=1}^{m}\left(\frac{y_i - \hat{y}_i}{y_i}\right)^2} \tag{3}$$

$$MAPE = \frac{1}{m}\sum_{i=1}^{m}\left|\frac{y_i - \hat{y}_i}{y_i}\right| \tag{4}$$

4) Prediction Performance Comparison Between Proposed Adaptive Remedial Action Scheme (RAS) and Conventional RAS

This section is to verify that the proposed adaptive Remedial Action Scheme (RAS) is better than the conventional RAS.

Proposed Adaptive RAS. Figure 64(a) shows the maximum and minimum frequency in two islanded systems respectively based on the prediction results without penalization (N = 1). The shadow area is the security region where UFLS and OVGT are not triggered. If no penalization, only 58.09% of cases are in the security region. Figure 64(b) and (c) show the histogram of maximum frequency in Island 1 and the histogram of minimum frequency in Island 2.

Similarly, Figure 65 and Figure 66 show the maximum and minimum frequency of the two islanded systems respectively, and also shows the histogram of maximum frequency in Island 1 and the histogram of minimum frequency in Island 2 when N =10 and N =20. In 92.36% (or 97.77%) of the total cases, the maximum and minimum frequency are inside the secure region, when N = 10 (or N = 20).

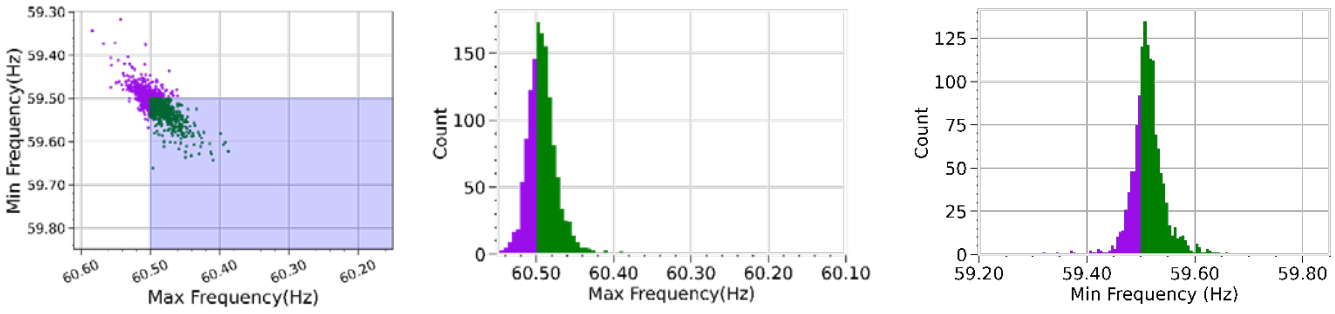

(**a**) Max. and Min. frequency (b) Max. frequency histogram in Island 1 (c) Min. frequency histogram in Island 2

Figure 64. Max. & Min. frequency and histograms of Island 1 and Island 2: N = 1. (purple: outside secure region, green: inside secure region, shaded area: secure region)

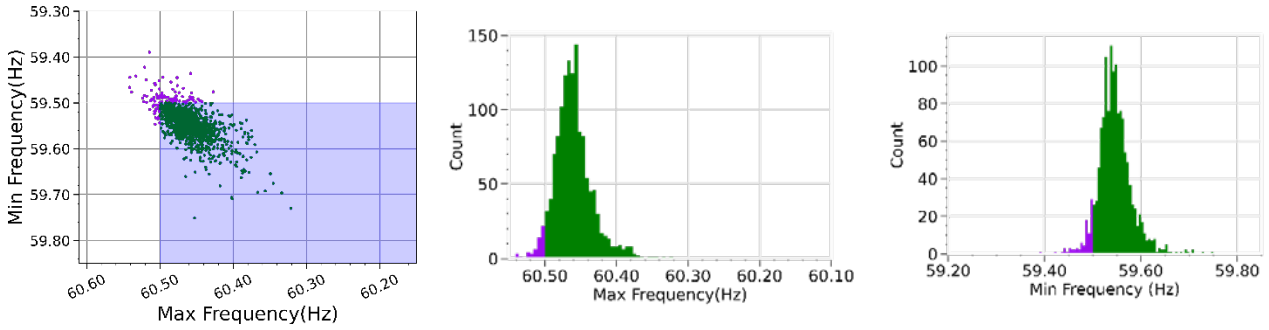

(**a**) Max. and Min. frequency

(b) Max. frequency histogram in Island 1

(c) Min. frequency histogram in Island 2

Figure 65. Max. & Min. frequency and histograms of Island 1 and Island 2: N = 10. (purple: outside secure region, green: inside secure region, shaded area: secure region)

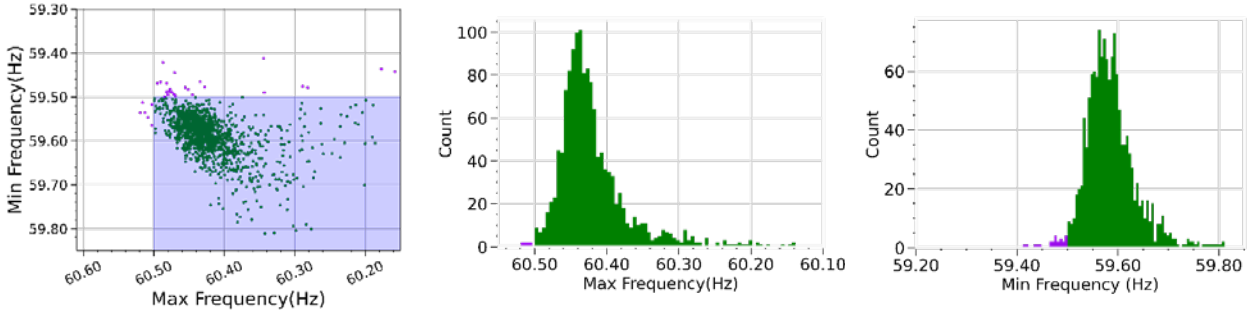

(**a**) Max. and Min. frequency

(b) Max. frequency histogram in Island 1

(c) Min. frequency histogram in Island 2

Figure 66. Max. & Min. frequency and histograms of Island 1 and Island 2: N = 20. (purple: outside secure region, green: inside secure region, shaded area: secure region)

Table 16 gives the performance of the model with different penalizing factor N. The frequency between 59.5 Hz and 60.5 Hz is considered the secure region. As shown in Table 16, with larger N, RMSPE and MAPE are getting larger, but in more cases the frequency is inside the security region. This means the customized loss function can make the predicted value more conservative by penalizing the values out of the security region. For instance, when N = 20, the frequency will be inside the security region in 97.77% of the cases.

Table 16. Prediction Errors With Different Penalizing Factors

N	RMSPE Island 1 / Island 2	MAPE Island 1 / Island 2	Inside Security Region (%)
1	7.15% / 4.94%	3.50% / 3.04%	58.09
2	8.37% / 5.43%	4.73% / 3.49%	76.70
3	6.90% / 5.09%	3.84% / 3.14%	73.14
10	14.10% / 7.89%	8.86% / 5.93%	91.78
15	14.23% / 9.50%	9.40% / 6.83%	92.36
20	28.23% / 14.54%	18.36% / 11.44%	97.77

Traditional RAS. In contrast, traditional RAS is designed based on the rate of active power change to frequency change to estimate the generation trip and load shedding for each operating condition.

Since the WECC system is separated into two islands after the activation of WECC-1 RAS, the rate of active power change to frequency change is calculated separately for two islanded systems. Two scenario simulations are performed in order to calculate the rate r_{11} and r_{21} for one dispatch.

In scenario 1, if load decrease P_1 and load increase P_2 performed in two islanded systems equal to the power flow of the tie lines connecting these two systems before RAS, the two islanded systems' frequency nadir and frequency maximum will be f_{11} and f_{21}.

In scenario 2, if optimal load decrease P_{o1} and optimal load increase P_{o2} are performed in two islanded systems, the two islanded systems' frequency nadir and frequency maximum will be 59.5Hz and 60.5Hz. The rate r_{11} and r_{21} for two islanded systems can be calculated as follows.

$$r_{11} = \frac{P_1 - P_{o1}}{f_{11} - 59.5}, \tag{5}$$

$$r_{21} = \frac{P_2 - P_{o2}}{f_{21} - 60.5}. \tag{6}$$

The average rates of four typical scenarios: heavy load case, light load case, high renewable penetration case, and low renewable penetration case are calculated and used as the final rates of active power change to frequency change for two islanded systems in WECC system in equation (7). The average frequency nadir and frequency maximum of four typical scenarios in two islanded systems after RAS when performing load decrease and load increase using tie line flows, are calculated in equation (8).

$$\begin{cases} r_1 = \sum_{i=1}^{4} r_{1i} \\ r_2 = \sum_{i=1}^{4} r_{2i} \end{cases} \tag{7}$$

$$\begin{cases} f_1 = \sum_{i=1}^{4} f_{1i} \\ f_2 = \sum_{i=1}^{4} f_{2i} \end{cases} \tag{8}$$

In actual system operation, tie line flows between two subsystems P_{1r} and P_{2r} can be monitored and obtained once RAS is detected. Then, the optimal load decrease amount P_{o1r} and load increase amount P_{o2r} in two islanded systems for that operation condition can be calculated in (9) and (10).

$$P_{o1r} = P_{1r} - r_1 * (f_1 - 59.5) \tag{9}$$

$$P_{o2r} = P_{2r} - r_2 * (f_2 - 60.5) \quad (10)$$

Where r_1, r_2, f_1 and f_2 can be calculated in equation (7) and (8) using offline simulations on four typical scenarios. P_{1r} and P_{2r} are known for each operating condition.

Based on traditional RAS calculation, Table 17 shows the performance on the traditional RAS. Only in 33.78% of the cases, the frequency is inside the security region.

Table 17. Performance on Testing Data Based on Traditional RAS Calculations

RMSPE Island 1/2	MAPE Island 1/2	Inside Security Region (%)
9.65% / 19.70%	5.65% / 14.09%	33.78

Figure 67 shows the frequency distributions of two islanded systems based on traditional RAS. The frequency of one system is scattered in a larger range compared with the other system.

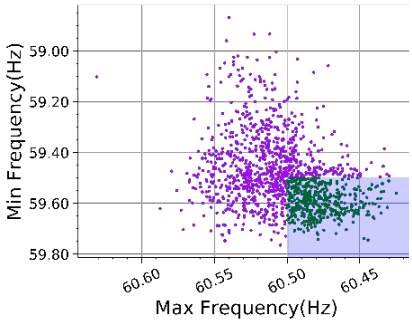

(**a**) Max. and Min. frequency

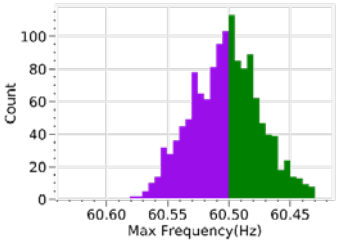

(b) Max. frequency histogram in Island 1

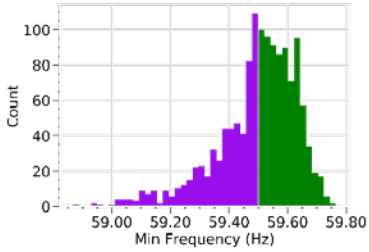

(c) Min. frequency histogram in Island 2

Figure 67. Max. & Min. frequency and histograms of Island 1 and Island 2: Traditional RAS. (purple: outside secure region, green: inside secure region, shaded area: secure region)

By comparing Table 17 with Table 16, we can see that the error level of the conventional RAS is comparable to cases when N=10 and N=15 in the proposed adaptive RAS. However, the security levels are 91.78% (N=10) and 92.36% (N=15) for the adaptive RAS, in comparison with the 33.78% security level in the conventional RAS. This implies that the adaptive RAS has better performance in estimating the optimal MW change amount while maintaining the frequency in the desired region as much as possible. This difference can also be noticed by comparing the distribution of frequency distributions in Figure 65 and Figure 67.

5) Layer Number and Node Number Selection

Another work done in this quarter is exploring the best layer and node numbers in deep learning. The deep learning neural network model is trained with 80% of the total dataset. This work uses TensorFlow, which is an open-source software for machine learning. Early stopping technique is used to prevent overfitting. The rest 20% dataset is used for performance evaluation. The model can have different layer numbers and different node

numbers in each layer. A model with too many weights tends to be over fitting, but with insufficient weights tends to be under fitting. In this study, models with 2, 5, and 7 hidden layers and with 50, 100, 300, 500, 800, 1000, 1500, 2000 and 3000 nodes are compared.

Figure 68 shows different models' performances. The model with 2 hidden layers and the model with 5 hidden layers has similar performance. Both are better than the model with 7 hidden layers. For the model with 2 hidden layers, its performance does not improve significantly if the node number is larger than 300. As more complex model is more likely to overfit, the 2 hidden layers with 300 nodes in each layer is selected as the optimal model structure.

	2 layers	5 layers	7 layers
Island 1	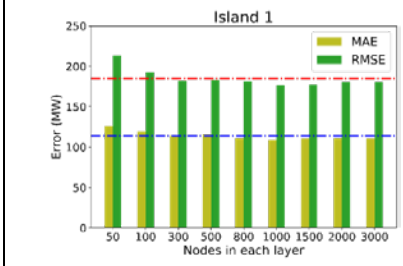	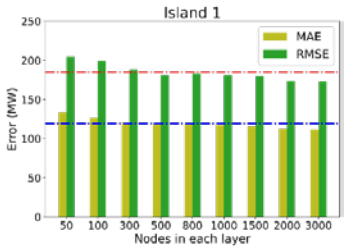	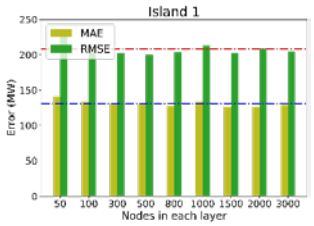
Island 2	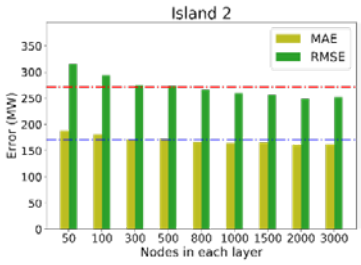	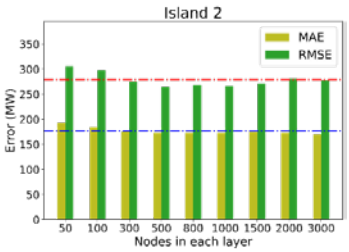	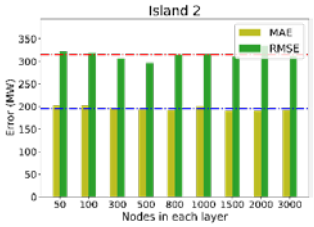

Figure 68. Model performance with different layers and nodes

6) Regularization Hyper Parameter Tuning

This quarter's work also includes exploring the impact of the regularization hyper parameter on system prediction error. Table 18 shows the performance of the trained model with different L1, L2 regularization techniques. When both L1 and L2 are equal to 1, the model can achieve the best performance. Table 19 and Table 20 show the performance of the trained model with different dropout regularization techniques and Gaussian noise levels, respectively. Neither dropout regularization nor Gaussian noise can help significantly improve the model performance, and thus they are not used in this study.

Table 18. Performance of Trained Model With L1 and L2 Regularization Techniques

Hidden Layers /Nodes	L1, L2	RMSE (MW) Island 1 / Island 2	MAE (MW) Island 1 / Island 2
2/300	0	182.31 / 275.62	112.05 / 169.51
	0.0001	185.24 / 276.63	116.20 / 173.58
	0.001	187.58 / 280.95	116.65 / 173.68
	0.01	185.62 / 279.33	116.19 / 175.02
	0.1	175.12 / 259.69	107.88 / 163.45
	1	132.23 / 206.36	87.64 / 134.07
	5	133.17 / 209.35	89.67 /136.25
	10	134.49 / 206.92	91.50 / 135.64
	20	142.41 / 224.85	101.61 / 152.53

Table 19. Performance of Trained Model With Dropout Regularization Techniques

Hidden Layers /Nodes	Dropout rate (%)	RMSE (MW) Island 1 / Island 2	MAE (MW) Island 1 / Island 2
2/300	0	182.31 / 275.62	112.05 / 169.51
	0.001	182.02 / 275.30	113.62 / 172.90
	0.01	182.51 / 276.03	114.89 / 171.89
	0.05	191.58 / 281.00	124.78 / 181.59
	0.1	193.39 / 277.66	127.18 / 179.49
	0.3	208.59 / 298.81	141.53 / 197.86

Table 20. Performance of Trained Model With Gaussian Noise Regularization Techniques

Hidden Layers /Nodes	Gaussian Noise (std)	RMSE (MW) Island 1 / Island 2	MAE (MW) Island 1 / Island 2
2/300	0	182.31 / 275.62	112.05 / 169.51
	0.0001	185.90 / 279.24	116.81 / 175.06
	0.001	185.53 / 277.87	116.65 / 173.68
	0.01	179.49 / 262.96	115.21 / 172.00
	0.1	212.98 / 315.83	149.92 / 217.31
	1	454.10 / 656.37	345.28 / 494.78

C. Summary

In this quarter, the 240-bus reduced WECC system was used to study deep learning based WECC-1 RAS load adjustment amount prediction. To maintain the system frequency range between 59.5 Hz and 60.5 Hz with the minimum load adjustment in MW, the more economic strategy was developed based on deep learning and compared with the tie-line-flow-based technique. Analysis revealed that due to negative errors in the neural network's loss function, almost half of the cases triggered under frequency load shedding or over-frequency generation trip. After implementing the customized loss function to penalize the cases when the absolute value of the prediction is greater than ground truth, the percentage of cases within the safety margin jumped from 58% to 92%. We also provided a more detailed comparison with conventional RAS. The comparison

shows that the proposed RAS has better performance in estimating the optimal MW change amount while maintaining the frequency in the desired region as much as possible. In addition, the layer and node numbers, and the regularization hyper parameters in deep neural network were tuned to optimize the performance of the proposed RAS.